Department of Physics and Astronomy

University of Heidelberg

Master thesis

in Physics

submitted by

Richard Kaiser

born in Mannheim

2019

Study of the nuclear modification factor of charged particles in Pb-Pb and Xe-Xe collisions with ALICE

This Master thesis has been carried out by Richard Kaiser

at the

Physikalisches Institut Heidelberg

under the supervision of

Priv.-Doz. Dr. Kai Schweda

Zusammenfassung

Diese Arbeit präsentiert eine Analyse des nuklearen Modifikationsfaktors R_{AA} in Schwerionenkollisionen von Xenon-Xenon und Blei-Blei Kollisionen im transversalen Impulsbereich von $0.15 < p_T < 50$ GeV/c und einem Pseudorapiditätsbereich von $|\eta| < 0.8$ von geladenen Teilchen in neun Zentralitätsklassen. Die zugrundeliegenden Daten wurden jeweils im Jahr 2017 und 2015 , mit einer Schwerpunktsenergie $\sqrt{s_{NN}}$ von 5.44 TeV und 5.02 TeV, aufgenommen. Die aufgezeichneten Daten wurden anschließend mit Monte Carlo Simulationen auf ihre Effizienz hin korrigiert. Die Teilchenzusammensetzung, sowie die Auflösung des transversalen Impulses, wurden anhand experimenteller Daten korrigiert. Das Ziel dieser Arbeit liegt darin, den nuklearen Modifikationsfaktor sowohl in gleicher Multiplizität, als auch in gleicher Zentralität der Kollisionen zu analysieren. Die bestimmten systematischen Fehler belaufen sich hierbei auf unter 10%, sie sind jedoch abhängig von dem transversalen Impuls und der Zentralität der Kollision. In dem Verhältnis der beiden nuklearen Modifikationsfaktoren ist für eine gleiche Multiplizität in beiden Kollisionssystemen ein Unterschied im Bereich von $2 < p_T < 4$ GeV/c mit einer Ausprägung in Höhe von ca. 10% zu sehen.
Ein Vergleich mit Daten des CMS Experimentes zeigt gute Übereinstimmung bei zentralen und semizentralen Kollisionen. Die größer werdenden Unterschiede in peripheren Kollisionen bleiben unverstanden.
Modellrechnungen können die Daten in zentralen Kollisionen beschreiben, jedoch nicht in semi-zentralen oder peripheren Kollisionen.

Abstract

This thesis presents studies on the nuclear modification factor R_{AA} in heavy-ion collisions of xenon-xenon and lead-lead ions in a transversal momentum range of $0.15 < p_T < 50$ GeV/c within a pseudorapidity range $|\eta| < 0.8$ of charged particles in nine centrality classes. The data were recorded in 2017 and 2015 respectively at the ALICE experiment with a center of mass energy $\sqrt{s_{NN}}$ of 5.44 TeV and 5.02 TeV. The obtained data was then corrected for efficiencies using Monte Carlo data samples. The particle composition as-well as the transverse momentum resolution was corrected in a data-driven approach. The goal of this thesis was to observe if matching the multiplicity or the centrality of two different colliding systems shows comparable results for the nuclear modification factor. Systematic uncertainties which were calculated throughout this thesis are no larger then 10%, but depend on the transverse momentum and centrality of the collision. In the ratio of the two nuclear modification factors at $2 < p_T < 4$ GeV/c a difference of around 10% is visible for central and mid central collisions at matched multiplicity between the two colliding systems.
Comparisons to experimental results from the CMS experiment show an agreement for central and mid-central collisions. The divergence for peripheral collisions is not understood.
Model calculations can describe the data in central collisions. However not anymore in mid-central and peripheral collisions.

Contents

1 Introduction

Nuclei are composed of protons and neutrons, called nucleons. The protons and neutrons are hadrons that are of bound states of quarks and gluons [1]. The fundamental **Q**uantum **F**ield **T**heory (QFT) describing the interactions and dynamics of quarks and gluons is called **Q**uantum **C**hromo **D**ynamics (QCD). Quarks and gluons are confined in hadrons, and never occur as free particle like for example an electron. Confinement of quarks and gluons is still not fully understood, since free quarks have never been observed in an experiment [2]. When heating and compressing nuclear matter sufficiently large, a phase transition to a **Q**uark **G**luon **P**lasma (QGP) occurs in which the quarks and gluons are deconfined. Such a state of matter with deconfined quarks and gluons is supposed to have existed during the early universe [3].

Using ultrarelativistic heavy-ion collisions, a QGP can be formed for a short time ($\approx$ 10 fm/c [4]). In heavy-ion colliders, like the **R**elativistic **H**eavy-**I**on **C**ollider (RHIC) or the **L**arge **H**adron **C**ollider(LHC), heavy nuclei are accelerated to relativistic energies and then collided, forming a hot and dense medium. The LHC, as the highest energy particle accelerator currently in existence, provides heavy-ion collisions with energies several times larger than the critical temperature T_c. Here, T_c is denoting the critical temperature at zero baryon chemical potential at which the phase transition between a hadron gas and the quark gluon plasma takes place [5]. The temperature is estimated from lattice QCD calculations [6]. It coincides with the chemical freeze-out temperature which describes hadron abundancies within the Statistical Model [6].

The QGP created in accelerators is not observed directly but studied through hadrons and particles produced in the collision or during hadronization. Characteristically for a QGP is that fast quarks and gluons can not traverse it freely but will lose energy according to the properties of the QGP. This energy loss is experimentally observed in hadron spectra as a depletion of yields when compared to a scaled pp reference.

At the LHC, a pilot run of Xe-Xe collisions was held in 2017 and recorded at the ATLAS, CMS and ALICE detectors. Normally, Pb-Pb collisions are performed because of their high nucleon count ($A_{Pb} = 208$) and the precise knowledge of the ground state properties of lead nuclei. The higher the nucleon count, the larger the energy density and the larger the QGP gets. Xenon ions with a nucleon count of $A_{Xe} = 129$ are in the middle between proton and lead nuclei. Analyzing the Xe-Xe collisions and comparing them to Pb-Pb collisions is the task of this thesis. For this purpose not only the centrality of both colliding systems is matched, but also the charged-particle multiplicity. The multiplicity denotes the number of particles, that

are created in the collision, in a given pseudorapidity range (typically at ALICE $|\eta| < 0.8$) and the centrality describes the geometric overlap of the colliding nuclei. The nuclear modification factor describes the ratio of the transverse momentum distribution of particles created in a heavy-ion collision divided by the distribution of a proton-proton collision at same center of mass energy. This ratio is then scaled by the nuclear overlap gathered through Monte Carlo Glauber simulations [7]. When comparing the nuclear modification factor for same centrality or multiplicity for two collision systems of different size, one can gain give insight on the path length dependence inside the QGP and gain access to the energy loss mechanism. Various models exist that calculate energy loss of fast partons. The predicted energy loss crucially depends on the length that a parton propagates inside a QGP. This path-length dependence directly relates to the microscopic energy loss mechanism such as collisional and radiative energy loss. Comparing central collisions of two systems with different initial geometric size gives excellent control over the path length and thus providing a testbed to all models.
Within this thesis, an analysis on the transverse momentum spectra of Xe-Xe and Pb-Pb collisions is performed. The thesis is organized as follows. Section 1 gives a short introduction into the subject of heavy-ion collisions. Section 2 provides some theoretical background. Section 3 gives a brief overview of the ALICE experiment and its detectors. Section 4 describes the analysis of the data recorded in Xe-Xe and Pb-Pb collisions which leads to fully corrected data with applied systematic and normalization uncertainties as well as matched multiplicity bins ins Xe-Xe and Pb-Pb collisions. Section 5 presents the results of this analysis with comparisons to CMS experimental results and model comparisons. Section 6 gives a conclusion and outlook.

2 Theoretical background

This chapter briefly explains the theoretical knowledge needed to understand the results presented in this thesis. First, a short summary of the standard model of particle physics is given. Second, the observed and used variables and their acronyms are explained. Third, heavy-ion collisions and their associated energy-loss are discussed. Last, an overview of the differences between xenon and lead nuclei is given.

2.1 Standard model of particle physics

The standard model of particle physics describes particles and their interactions between them. Particles can be divided into two groups, bosons (integer spin) and fermions (half-integer spin). There are four known fundamental interactions in physics :

Strong interaction The strong interaction is the coupling between the quarks inside of a proton and neutron inside a nuclei. It dominantly contributes to the mass of the nuclei. Theoretically it is described by **Q**uantum **C**hromo **D**ynamics (QCD) as the underlying Quantum Field Theory and interacts via the exchange of gluons through color charge. It is as the name suggests the strongest interaction, but its range is limited. A source could be the experimentally observed gluon self interaction.

Electromagnetic interaction The electromagnetic interaction is together with gravity the most prominent interaction. It is widely observe in our every-day life. It couples to all charged particles via an exchange of a photon and is the most well understood interaction of all. It is theoretically described by **Q**uantum **E**lectro **D**ynamics (QED).

Weak interaction The weak interaction is weaker than the electromagnetic and strong interaction. This is due to the masses of the force carrier bosons, namely the $W^{\pm}$ and Z bosons. At energies larger than the masses of the exchange bosons, the electromagnetic and weak interaction are equally strong. The weak interaction is described together with the electromagnetic interaction in the electroweak unification. This theory also includes the Higgs field which is responsible for the masses of fundamental particles.

Gravity Gravity is the weakest interaction but its range is infinite. On cosmic scales, gravity is dominant, because strong and weak interaction are range limited and electromagnetic interactions are non existent because atoms are neutral. Gravity is described by Einsteins theory of General Relativity Theory. Gravity is not part of the standard model of particle physics since no accepted Quantum Field Theory of gravity exists.

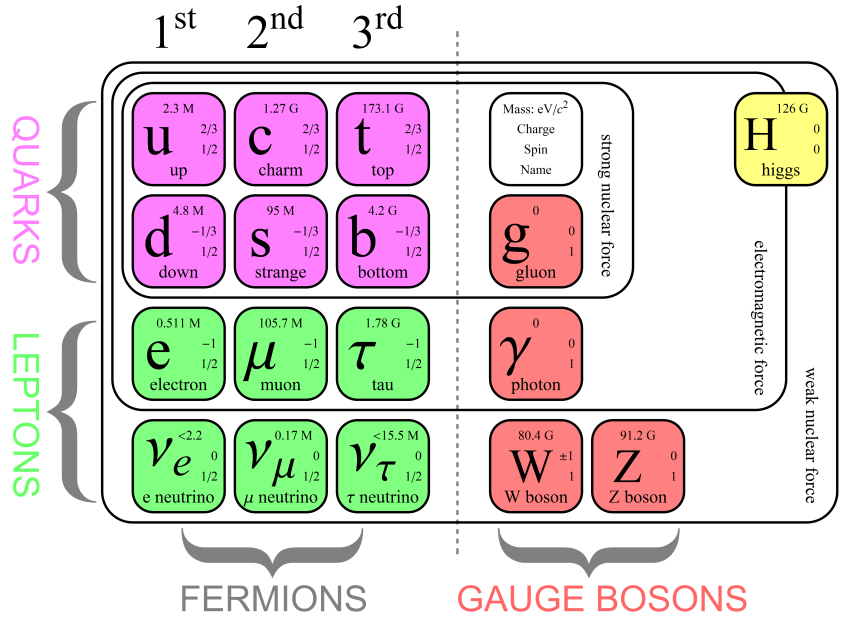

Figure 2.1: Fundamental particles of the standard model of particle physics [8].

The fermions can be divided into quarks and leptons and also into three flavours as shown in figure 2.1. Quarks have a color charge and can interact via the strong interaction, but they are only found in colorless bound states (hadrons). They can be subdivided in up-like particles (electric charge of $+\frac{2}{3}$e) and down-like particles (electric charge of $-\frac{1}{3}$e). Leptons have an integer electromagnetic charge and do not interact via the strong interaction. They can be divided into neutral neutrinos and charged leptons. The neutral neutrinos have a mass very close to zero but recent studies on neutrino oscillations show that they are not massless [9]. For further information about the principles of particle physics see [10].

2.2 Observables

In heavy-ion collisions, various variables are observed. For a better understanding of those, and their acronyms they are here explained briefly.

Transverse momentum p_{T}: The transverse momentum is the momentum of a particle transverse to the beam axis. It can be determined from the track radius $R = p_T/zB$ in ALICE. With B being the magnetic field strength and z being charge

of the particle. This equation can be translated to $R = \frac{10}{3}\frac{p_T}{B}[\frac{Tm}{GeV/c}]$, where p_{T} is given in GeV/c and the magnetic field strength is given in T.

Rapidity y: The rapidity is $y = \frac{1}{\sqrt{1-v^2/c^2}} = \frac{1}{2}ln\frac{E+|p_L|}{E-|p_L|}$ with p_L being the momentum longitudinal to the beam direction. It is a measure for relativistic velocity in beam direction. The rapidity is Lorentz invariant with a remaining offset constant.

Pseudorapidity η: The pseudorapidity describes the angle of a particle with respect to the beam axis. It is calculated as $\eta = -ln[tan(\frac{\theta}{2})]$. The larger η the closer to the beam axis the particle is. An $\eta = 0$ describes a particle perpendicular to the beam axis. For a massless particle, or when the mass is negligible (e.g. the ultra-relativistic case) the pseudorapidity coincides with the rapidity.

Monte Carlo Glauber: The Monte Carlo Glauber simulation is a special Monte Carlo simulation which takes advantage of the Glauber model. It takes the nucleons as having straight-line trajectories and being independent of previous interactions. Furthermore, the nucleons are distributed in three dimensions according to a Woods-Saxon parametrization of the nuclear shape.

Multiplicity: The multiplicity describes the number of charged particles produced in a heavy-ion collision in a given pseudorapidity range. In the case of the ALICE detector, this is usually a range of $|\eta| < 0.8$. The multiplicity is measured directly by the ITS or calculated using the p_{T} spectra and extrapolating it to zero p_{T}.

Number of collisions and participants $\mathrm{N_{COLL}}$ and $\mathrm{N_{part}}$: These describe the number of binary collisions or the number in a heavy-ion collision of nucleons participating in the collision. They are quantities obtained from Monte Carlo Glauber simulations.

Centrality: The centrality describes how central a heavy ion collision is in percentiles. The centrality is measured through the distribution of multiplicity which then gets separated into equal event count bins. The most central collisions (centrality of 0%) are also the ones with the highest multiplicity since the $\mathrm{N_{part}}$ is largest for most central events.

Primaries and secondaries: The ALICE definition of primary particles is described as [11]: "A primary particle is a particle with a mean proper lifetime τ larger than 1cm/c which is either produced directly in the interaction, or from decays of particles with τ smaller than 1cm/c, restricted to decay chains leading to the interaction." Particles that do not follow this definition are generally described as secondaries.

Nuclear overlap function T_{AA}: This value is not acquired through data, but is extracted from a Monte Carlo Glauber simulation. It describes the overlap of the two colliding heavy-ions as an inverse cross section. It is calculated through $T_{AA} = \frac{N_{COLL}}{\sigma_{inel}}$, with σ_{inel} being the cross-section of inelastic collisions in a heavy-ion collision. It is gathered for each centrality bin and it's dimension is inverse barn.

pp reference σ_{pp}: It is the invariant p_T dependent cross section of a p-p collision at the same energy as the heavy-ion collision.

Nuclear modification factor R_{AA}: The nuclear modification factor is calculated using $R_{AA}(p_T) = \frac{1}{T_{AA}} \cdot \frac{dN_{AA}(p_T)/dp_T}{d\sigma_{pp}(p_T)/dp_T}$. It describes an enhancement (> 1) or suppression (< 1) of hadron production in heavy-ion collisions compared to proton-proton collisions. It is a dimensionless variable.

2.3 Heavy-ion collisions

Heavy-ion collisions differ significantly from their proton-proton equivalent. First the ion is much larger and carries a larger energy in total than a single proton can. The nuclei in heavy-ion collisions are made up of over 100 nucleons, when two nuclei collide they do not have a head-on collision like in the proton-proton case, but rather the number of participants varies for each collision and is a measure for the centrality of the event. Collisions of two heavy-ions form a dense and hot matter, if the energy is large enough, the matter undergoes a phase-transition and becomes a QGP. The strong interaction is the main force in the QGP and therefore electrons and photons created in the interaction roam freely through the plasma and in principle date back to the beginning of the plasma. Fast quarks and gluons however will experience energy loss through the QGP which is observed in the hadron p_T spectra. The energy loss can be divided into linear energy loss through elastic collisions with particles in the QGP and radiative energy loss through gluon bremsstrahlung in the medium (for a sufficiently thin medium). This also leads to a quenching of jets which will be explained in section 2.3.2. The QGP which is observed by the ALICE experiment at the LHC is formed in ultra-relativistic heavy-ion collisions disintegrates within 10 - 20 fm/c (3 - 6 10^{-23} s)[12].

2.3.1 Evolution of heavy-ion collisions

In figure 2.2, the space-time evolution of a heavy-ion collision is depicted. Before the collision, the two nuclei are Lorentz contracted disks, which are moving with almost the speed of light towards each other [13]. At $\tau = 0$, the collision occurs when the nuclei have contact. Hereby, τ refers to the proper time $\tau = \sqrt{t^2 - x^2}$ with x being the spatial coordinates. First the hard parton-parton collisions occur which produce high-p_T hadrons. The next phase is the pre-equilibrium phase where softer parton-parton collisions occur, which thermalize the energy. This is leading to a state of

matter with deconfined quarks and gluons. The Quark Gluon Plasma is formed. The medium expands which can be described by hydrodynamical calculations assuming a local thermodynamic equilibrium. Through the expansion, the medium cools down till it drops below the critical temperature T_c. The partons under confinement form a hadron gas. The hadron gas is still a hot dense medium which expands and cools down till the rate of inelastic collisions becomes so small, that the hadron abundances become fixed at the chemical freeze out. When the elastic collisions stop, the kinetic freeze out occurs.

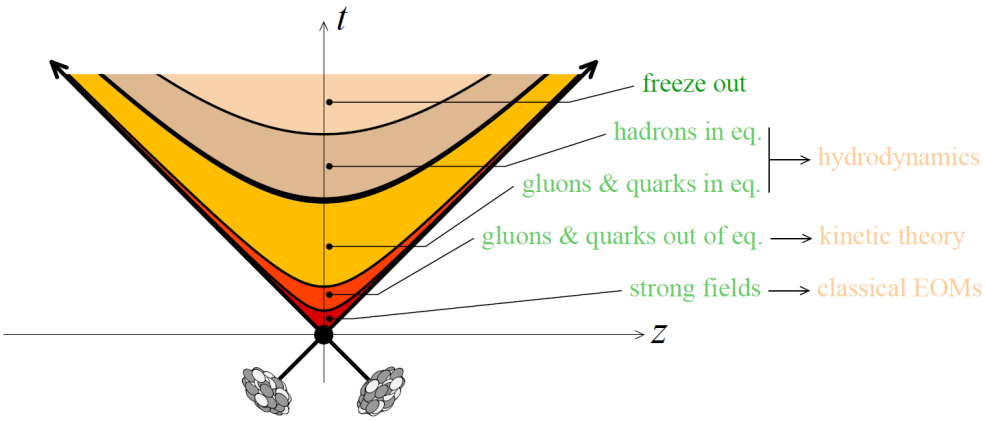

Figure 2.2: Space-time evolution of a heavy-ion collision[13].

2.3.2 Energy loss in heavy-ion collisions

In heavy-ion collisions, high p_{T} partons are created during the early phase of the collision. These particles experience the full evolution of the newly formed QGP and upon leaving the QGP will fragment into a set of final-state hadrons. The characteristic collimated spray of hadrons for an outgoing parton is called jet. In figure 2.3 this jet is presented. Also presented is a characteristic of the QGP, jet quenching. A particle traversing the QGP will suffer energy loss in the hot dense QGP which leads to a suppressed (quenched) jet [14].
There are two ways of energy loss in the QGP, they are presented in figure 2.4. First particles scatter through elastic collisions inside the medium. This dominates for low p_{T} particles. Second there is the radiative energy loss through inelastic scattering such as gluon bremsstrahlung. This dominates for high momentum particles. Both ways of energy loss are driven by the strong interaction which is the dominant interaction in the QGP [14].

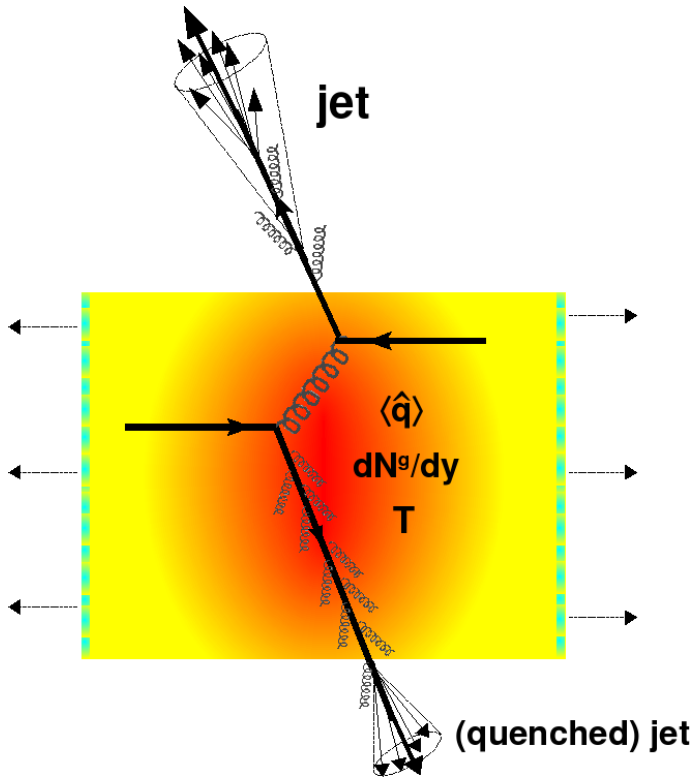

Figure 2.3: Graphical representation of the jet quenching effect. The medium is described by the transport coefficient $\langle \hat{q} \rangle$, the gluon density dN_g/dy and the temperature T [14].

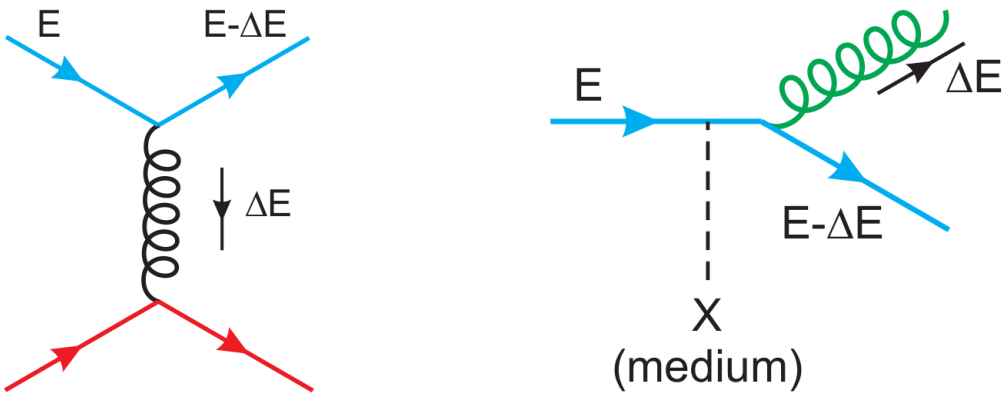

Figure 2.4: Feynman diagrams of the two models of energy loss in the QGP are shown. On the left, elastic scattering is presented and on the right, inelastic scattering is visible [14].

2.4 Difference between lead and xenon nuclei

Since this thesis accommodates both lead and xenon nuclei, their characteristics and differences in the ground-state will be shown here. The used xenon isotope has 129 nucleons and the lead isotope has 208 nucleons, thus the xenon isotope sits between Pb-Pb and p-p collisions in terms of nucleons. This made it the ideal candidate for a search of path length dependence in heavy-ion collisions.

The Woods-Saxon parametrization

$$\rho(r,\theta) = \rho_0 \cdot \frac{1}{1 + exp(\frac{r-R(\theta)}{a})}$$

with

$$R(\theta) = R_0 \cdot (1 + \beta_2 Y_{20}(\theta))$$

describes the charge density of nuclei [15]. The parameters R_0, β_2 and a are individual for each nuclei and listed for ^{129}Xe and ^{208}Pb in Table 2.1. They can be measured by elastic scattering of electron beams on the nuclei, however for the xenon nuclei these parameters were extrapolated from existing results of other Xe isotopes [16]. The uncertainties on the xenon nuclei are therefore larger than those for lead. Xenon also has a quadrupole deformation which is expressed by the β_2 parameter. These uncertainties contribute to the T_{AA}.

	^{129}Xe	^{208}Pb
R_0 (fm)	5.36 ± 0.1	6.62 ± 0.06
a(fm)	0.59 ± 0.07	0.546 ± 0.01
β_2	0.18 ± 0.02	-

Table 2.1: Parameters of ^{129}Xe and ^{208}Pb in the Woods-Saxon parametrization.

3 The ALICE experiment

3.1 The LHC

The Large Hadron Collider (LHC) is the largest particle accelerator ever built. It is located at CERN (European Organization for Nuclear Research) in Geneva and is a ring accelerator with a circumference of 26.7 km as shown in figure 3.1. It is currently the largest and highest energy particle accelerator, although a successor the Future Circular Collider (FCC) is already being discussed and planned [17, 18, 19]. The LHC is designed for proton-proton collisions in contrast to proton-antiproton colliders like the Tevatron. This design needs two separate rings for the two colliding systems. At the LHC, this was accomplished by using one magnet with two beam pipes. This allows for a more compact design, but restricts the field strength of each beam to be the same. This induces different kinetic energies for each beam in an asymmetric collision system. The design beam energy of 7 TeV for protons (equivalent to $\sqrt{s} = 14$TeV) was reached whereas the design beam energy of $\sqrt{s_{\mathrm{NN}}}$ = 5.52 TeV for Pb-Pb collision was adjusted to an energy of $\sqrt{s_{\mathrm{NN}}} = 5.02$ TeV to match with the $\sqrt{s_{\mathrm{NN}}}$ of p-Pb collisions.

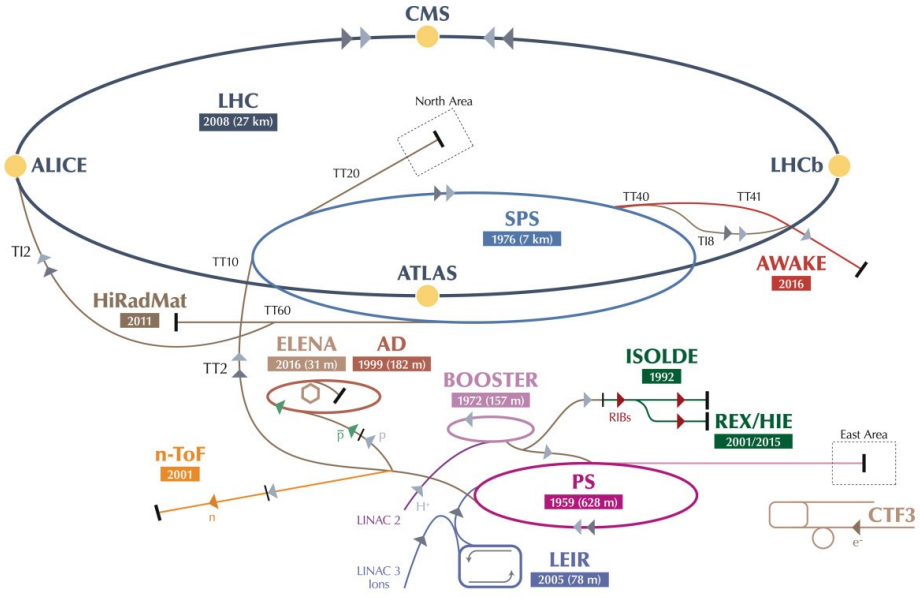

Figure 3.1: Top down view of the accelerator complex at CERN. Main point of interest is the LHC ring and its four major experiments. Source[20].

There are four large-scale experiments at the LHC: ALICE, ATLAS,CMS and LHCb.

ALICE will be described in more detail in the next section 3.2.
ATLAS (A Toroidal LHC ApparatuS) and CMS (Compact Muon Solenoid) are general purpose detectors and discovered the Higgs Boson in 2012 ([21] and [22]). The LHCb experiment is a forward arm detector and focuses in B-meson physics and CP-violation. It successfully discovered the pentaquark [23] and tetraquark [24] states.

3.2 The ALICE detector

ALICE (A Large Ion Collider Experiment) can be seen in figure 3.2. It is located at point 2. The purpose of the ALICE experiment is to investigate heavy-ion collisions at high multiplicity with excellent PID capabilities. It is especially built for the high track densities occurring in heavy-ion collisions. Consisting of two main parts, the muon forward arm spectrometer and a solenoid magnet with the central detectors. The large magnet, which was inherited from the previous L3 experiment at the LEP, houses the other detectors inside, providing a homogenous solenoid magnetic field up to 0.5 T. The experiment differentiates between an A and C side, where A denotes a positive z coordinate and C a negative z coordinate. The origin of the coordinate system in ALICE is in the interaction point with the z axis pointing along the beam axis. The individual detectors of ALICE are being shortly discussed. The main detectors used in this thesis are the ITS and TPC.

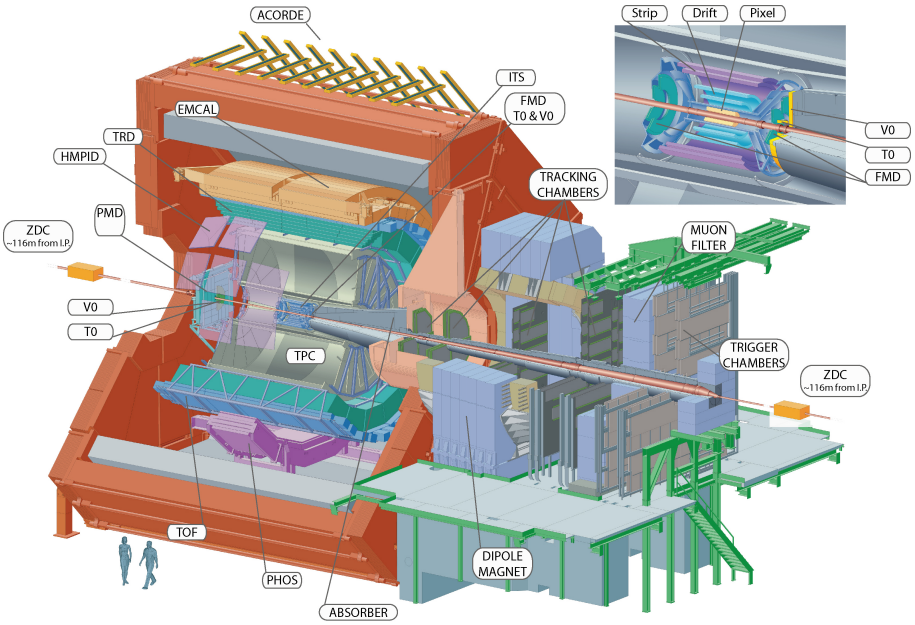

Figure 3.2: Representation of the ALICE detector with all its detectors marked. The persons depicted in the lower part are there to scale [25].

3.2.1 Inner Tracking System (ITS)

The Inner Tracking System (ITS) [26] consist of 6 layers of different silicon trackers. The first 2 layers are Silicon Pixel detectors (SPD), the next 2 are Silicon Drift detectors (SDD) and the last 2 are Silicon Strip Detectors (SSD). It covers a pseudorapidity range of $|\eta| \leq 0.9$. It provides primary vertex reconstruction as well as secondary vertex reconstruction and improves the tracking capabilities of the TPC. The two SPD layers are closest to the beam pipe at 39 and 70 mm and are equipped with hybrid silicon pixel detectors. They cover a pseudorapidity range of $|\eta| \leq 1.95$. The outer most layers, the SSD, is crucial in connecting the tracks from the TPC to the ITS. It also contributes to particle identification through measuring the energy loss.

3.2.2 Time Projection Chamber (TPC)

The Time Projection Chamber (TPC) [27, 28] is a 90 m^3 large gas detector located around the ITS. With an inner diameter of 80 cm and an outer diameter of 250 cm, it is the main detector for tracking and particle identification. It covers $|\eta| < 0.9$ for particles with a maximal track length of the whole detector. The volume of the TPC is divided by the central electrode depicted in figure 3.3. It generates an electric field of 400 V/m, directed towards the electrode with a potential of 100 kV. The electric field is homogenized by the outer field cage of the TPC.

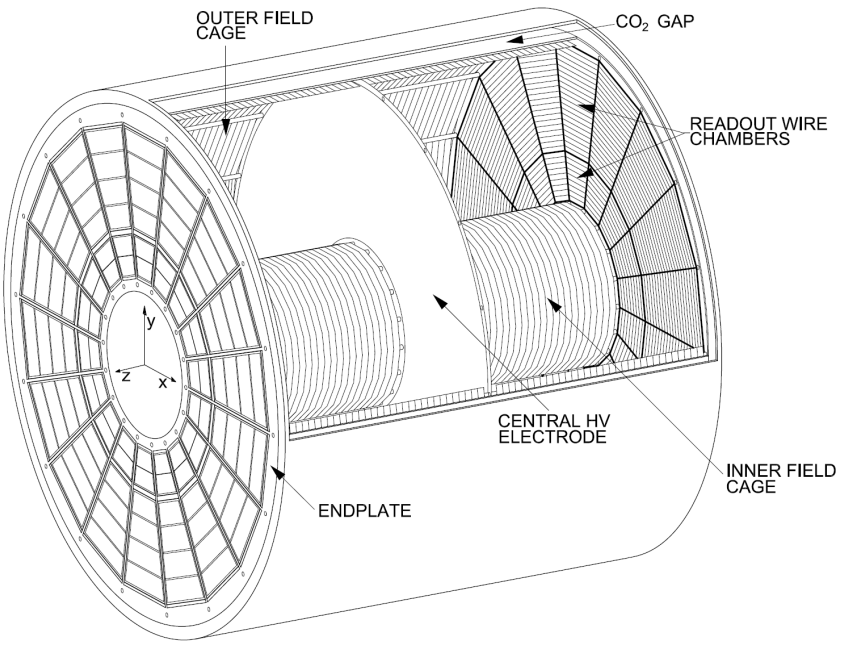

Figure 3.3: Schematic side view of the TPC field cage [27].

The TPC is filled with a gas composition which ionizes when charged particles traverse it. The gas composition has to provide a reasonable drift velocity for electrons and ions, does not damage or interfere with the detectors and be non explosive or flammable. The latter is due to safety concerns when having 90m^3 of a high reactive gas volume close to a high energy beam. The gas composition changed from Run1 to Run2 and also for the Xe-Xe collision data taking. For Run1, it was a mixture of 85.7% neon, 9.6% CO_2 and 4.7% N_2. In Run2, argon was chosen instead of neon as it generates more electrons through ionization, leaving a mixture of 88% Ar and 12% CO_2. Argon however did not provide adequate electron mobility and led to accumulation of space charge. Therefore the gas composition was then reverted back to its original state in 2017.
Electrons created through ionization in the TPC drift to either side of the detector where the endcaps and readout of the TPC are mounted. The endcaps are divided into 18 sectors with each covering an angle of 20 degree in azimuth and divided horizontally into inner and outer readout chambers. The readout is carried out through multiwire proportional chambers. In the inner region, the distance between the layers is 2 mm and in the outer region it is 3 mm. The first layer is the gating grid, its wires can be set to alternating potentials which closes the grid and hinders charged particles from traversing it. This is useful to not let ions from the amplification region reenter the TPC's active volume. It can also be set to the potential of the surrounding field and thus opening the gating grid for charged particles. The middle wire layer is the cathode layer which separates the amplification from the drift region. The charged particles are then accelerated towards the anode wire grid which strength is high enough to cause electron avalanches and therefore amplifying the electron signal.
In total 159 rows, with a total number of 557568 readout pads provide the high granularity used in the TPC tracking. In addition to the spatial signal detection in the r-ϕ plane, a sampling as a function of time is done. Together with the measured drift velocity, a t-component of the clusters can be determined. This is needed for a good track separation at high multiplicities of heavy-ion collisions at ALICE ($\frac{d\text{N}_{\text{ch}}}{d\eta} \approx 2000$). The tracks in the TPC are then reconstructed through clusterization of the signals.

3.2.3 Transition Radiation Detector (TRD)

The goal of the TRD is to identify electrons [29] in the region above 1 GeV/c. It also increases the measured track length through its tracking information which improves the resolution for high p_{T} particles. Furthermore can it be used as a trigger on electrons or high p_{T} particles and requiring several particles above a given p_{T} threshold even as a jet trigger.
The detector is located around the TPC at a radial distance of 2.9 m to 3.68 m and covers a pseudorapidity range of $|\eta| < 0.84$ and the full azimuthal region. As the TPC, it is segmented into 18 super modules containing 30 chambers each. Every chamber contains a radiation region and a drift region with an additional

amplification region and readout inside. High p_{T} electrons create transition radiation photons within the radiator. Those photons are usually absorbed within the first few mm of the drift region and cause ionization in addition to the primary energy loss of the particles. This allows to identify electrons on a track-by-track basis.

3.2.4 Time Of Flight (TOF)

The TOF [30] is a particle identification detector in momentum ranges where the TPC cannot be used. It provides pion/kaon and proton/kaon separation. Identification of electrons and nuclei also greatly improves with the TOF information. It is used as wake-up trigger for the TRD and even successfully for cosmic rays.
TOF measures the velocity β of a charged particle as the name suggest via the time it need from collision to the detector. The start signal is delivered by the T0 detector and the time resolution of the TOF is better than 40 ps. It is designed as a Multi-gap Resistive Plate Chamber (MRPC) and is segmented into 18 parts like the TPC and TRD. It is located outside the TRD at a radial distance of 3.78 m and covers the full azimuthal angle as well as a pseudorapidity range of $|\eta| < 0.9$.

3.2.5 Calorimeters

The Calorimeters are here briefly explained with their basic principle and their purpose.

Electromagnetic Calorimeter: The Electromagnetic Calorimeter (EMCal) [31] is an electromagnetic calorimeter with the purpose of measuring high p_{T} electrons and photons. It can also be used as a trigger for photons, electrons and jets. It uses a lead/plastic-scintillator calorimeter where the scintillation light is detected by avalanche photo diodes.

Photon Spectrometer: The Photon Spectrometer (PHOS) [32] is as the EMCal an electromagnetic calorimeter but purposely build for the detection of photons in the range of 0.1 GeV/c to 100 GeV/c. Therefore it is using high-density lead-tungstate ($PbWO_4$) crystals as scintillator. Again it uses avalanche photo diodes for readout.

Photon Multiplicity Detector: The designated purpose of the Photon Multiplicity Detector (PMD)[33] is to measure the multiplicity and spatial distribution of photons in the forward region on the A side. It consists of two gas counters with a lead converter in between. Photons convert in the lead and are detected in the second layer whereas other particles will leave a trace on both sides.

Forward Multiplicity Detector: As the name suggests the Forward Multiplicity Detector (FMD)[34] is designated on measuring charged particles at forward rapidity. Contrary to the PMD it is located on both sides of the interaction point, but with three of the five rings which make up the FMD located on the A side.

Muon spectrometer: The muon spectrometer in ALICE [35, 36] is, as shown in figure 3.2 installed only in forward direction of the experiment. The goal is to measure the dimuon decay channel of heavy flavor and vector mesons. It consists of a front absorber to filter the large amount of generated hadrons, a dipole magnet and five tracking stations. With the tracking stations not only being able to track the position but also the direction of the muon.

3.2.6 High Momentum Particle Identification Detector (HMPID)

The HMPID [37] is a Cherenkov ring detector which extends the particle identification capabilities to larger p_{T}. It measures the velocity of charged particles using the opening angle of Cherenkov radiation. Together with the information from the ITS and TPC particle identification can be made.

3.2.7 V0 detectors (V0)

The two VZERO (V0)[34] detectors are located on the forward side of the detector but opposite to each other. The V0A detector is situated in A direction, whereas the V0-C detector is on the C side. They are used as trigger detectors and are crucial for the minimum bias (MB) trigger. The other provided triggers are a multiplicity trigger, central and semi-central trigger. The multiplicity provided by the V0 detectors is also used for offline analysis. Due to their high time resolution of 1 ns beam induced background can be identified. The detectors consist of plastic scintillators which are aligned in disk shaped arrays and connected to photomultipliers.

3.2.8 T0 detectors (T0)

The TZERO (T0)[34] detectors are as the V0 detectors split in A and C side. They are used as a start signal for the TOF and as a wake-up trigger for the TRD. Twelve Cherenkov counters are used for each of the two arrays. It provides a time resolution of 50 ps.

3.2.9 Zero Degree Calorimeter (ZDC)

The ZDC [38] is as the previous detectors split in A and C side but this time they are located at a distance of 112 m from the interaction point. It measures the energy of nucleons which do not take part in the heavy-ion collision. The ZDC is then

again split into a neutron (ZN) and a proton (ZP) detector. Since neutrons are not bent by the LHC magnets, they get detected in the ZN detector whereas protons get deflected by the LHC magnets and are therfore detected in the ZP. They both use the same principle of measurement, which consists of a passive absorber with quartz fibers embedded as detector. The absorber provokes particle showers which in turn create Cherenkov radiation in the fibers. This radiation is then detected by photomultipliers. The ZDC's can moved out of beam plane when not in use to maximize the lifespan of the detectors.
For peripheral heavy-ion collisions, some spectators are bound in fragments of the nucleus which escape the detection of the ZDC's and thus leading to similar results than for central collisions. For this purpose, on the A side, an electromagnetic ZDC is located which measures the energy of the particles which scales monotonically with the centrality.

3.3 Centrality determination at ALICE

Centrality determination in ALICE is described in detail in ref.[39, 40]. The centrality is a measure of the nuclear cross section in percent and allows the relation of measured quantities to geometrical quantities of the collision which can not be observed, like the impact parameter b, the number of participants N_{part}, the number of binary collisions N_{COLL} or the overlap T_{AA}. For the determination of the centrality various detectors are used like the ZDC, V0, TPC and ITS. Their information is combined in a single framework to be easily used in the experimental data analysis.

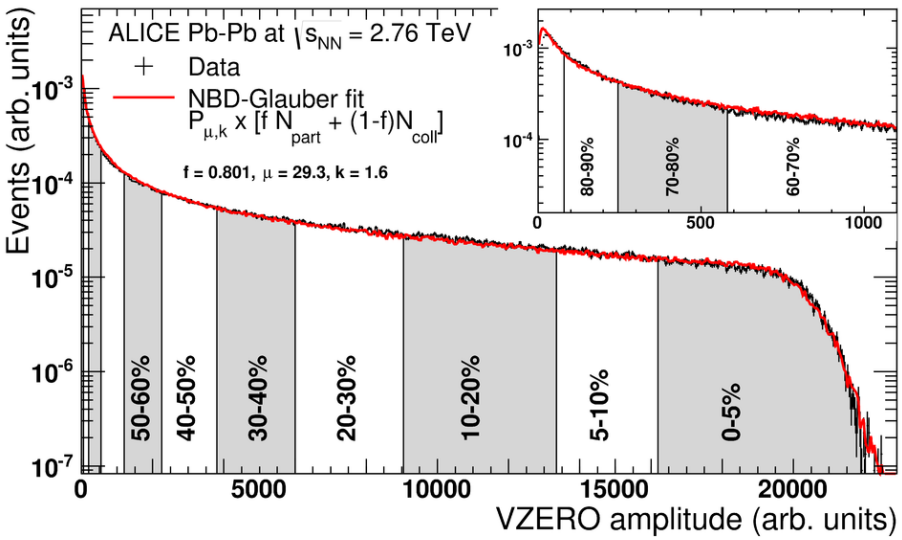

Figure 3.4: Event counts over the V0 amplitude. The V0 amplitude is representing the multiplicity of the collision. A convolution of NBD and Monte Carlo Glauber model was used as fit for the experimental data [39].

The best resolution is achieved when using the combined multiplicity (V0M) of the

V0 detectors. The V0M is hereby used as estimator for the collision centrality and is the main method used by ALICE. This multiplicity distribution is then fitted with a convolution of a negative binomial distribution (NBD) and a Monte Carlo Glauber Model. The distribution for Pb-Pb collisions is shown in figure 3.4. Only the range of 0-90% is used for the fit, as background contamination through electromagnetic processes disturb the measurement in the 90-100% centrality region. The lower end of this fit range is called Anchor Point (AP). The centrality is determined by using the same integrated number of events for each centrality bin. From these selections geometrical values can be obtained by inspecting the fitted Monte Carlo Glauber Model.

4 Analysis

This chapter presents the main focus of this thesis. It describes the analysis from raw data samples to a corrected R_{AA} measurement with systematic uncertainties in Xe-Xe and Pb-Pb collisions. The corrected data for both collision systems is then matched in multiplicity.

4.1 Data samples

For this analysis two different data samples and two Monte Carlo (MC) samples have been analyzed. The data samples were all recorded at ALICE (see section 3.2 for further information) in the year 2015 or 2017 for Pb-Pb and Xe-Xe collisions respectively. The focus of this thesis is on the collision of xenon (^{129}Xe) nuclei and on matching the multiplicity with collisions of lead (^{208}Pb) nuclei. Both have already been observed and analyzed in previous publications [41, 42]. In the publication of the Xe-Xe collision analysis of the nuclear modification factors [42] a comparison of R_{AA} for matched multiplicity was made and showed good agreement for most central collisions and differences, although still within systematic uncertainties, for more peripheral collisions. Due to the limitations of this publication to stick to the standard binning of the Pb-Pb data, the two matches in multiplicity were not sufficient enough to make a sophisticated assumption. Therefore, the goal of this thesis was to get the data in a smaller bins of centrality to get a matched multiplicity over the complete centrality range of Xe-Xe collisions. The different experimental datasets and their event counts per centrality bin are shown in figure 4.1.

4.1.1 Xe-Xe collisions

For Xe-Xe collision, there was one experimental dataset and one Monte Carlo (MC) dataset. The Xe-Xe run was a pilot run at the LHC in 2017 with just $\approx$ 8 hours of data taking. The data is from 2017 (LHC17n) and contains 1.6 million minimum bias events. The MC sample is from 2017 (LHC17j7) and was generated with the HIJING event generator [43] and contains 0.87 million minimum-bias events. An important difference in the experimental setup between Xe-Xe and Pb-Pb collisions aside from the nuclei count is the changed magnetic field from 0.5 T in Pb-Pb collisions to 0.2 T in Xe-Xe collisions. This change was made to allow tracking and reconstruction of lower momentum particles. Additionally, the energy of the systems is different with $\sqrt{s_{\mathrm{NN}}} = 5.44$ TeV for Xe-Xe collisions ans $\sqrt{s_{\mathrm{NN}}} = 5.02$ TeV for Pb-Pb collisions. The change was made due to time constraints for the pilot run

and calibrating a specific beam energy for the Xe-Xe collisions taking up too much time.
The data in Xe-Xe collisions is analyzed in standard centrality binning (0, 5, 10, 20, 30, 40, 50, 60, 70, 80%). More peripheral collisions were not considered due to electromagnetic contaminations, which set in at a lower centrality for Xe-Xe collisions than for Pb-Pb collisions because of the lower N_{part} due to the lower nuclei in the nucleus.

4.1.2 Pb-Pb collisions

For Pb-Pb collisions one experimental dataset and one Monte Carlo dataset were used. The dataset is from the October 2015 (LHC15o_pass1_pidfix) data taking period with a collision energy of $\sqrt{s_{NN}} = 5.02$ TeV containing 38.7 million minimum bias events. The minimum bias trigger will be explained in section 4.2. The Monte Carlo sample is from 2016 (LHC16g1abc), a simulation with the HIJING event generator [43] and contains 1.7 million minimum bias events.
The Pb-Pb data is then analyzed with two different kinds of binning, one is in standard binning (0, 5, 10, 20, 30, 40, 50, 60, 70, 80, 90)% and the other one in 1% steps up to 90% centrality. Larger centralities are not considered due to electromagnetic contamination. The Monte Carlo dataset is only available in standard binning since the lower statistics would not allow such a fine binning. Also, the tracking efficiency scales only to a small degree as discussed in section 4.3.1

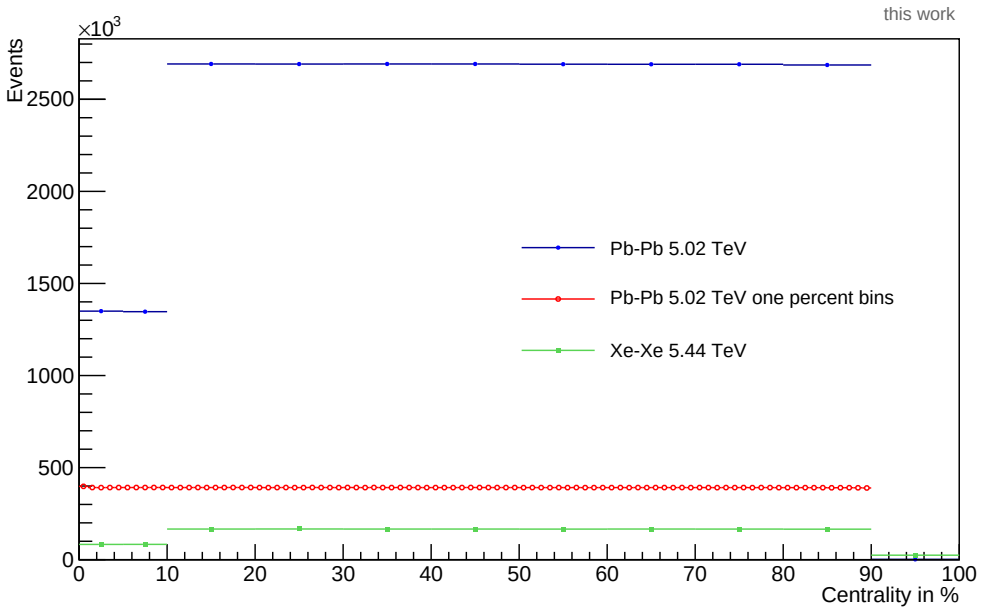

Figure 4.1: The event counts for each centrality bin are shown for two collision systems. Note that although the Pb-Pb data is scaled in one percent bins the event counts are still higher than for the 10% Xe-Xe bins.

4.1.3 Getting fine bins in Pb-Pb collisions

Normally, the datasets are analyzed on the Grid. The Grid hereby denotes an international computer and data cluster of research facilities. Not only the processing power is distributed and managed over the Grid, but also the large amounts of datasets. On the Grid there are Lego Trains running with wagons. The Train itself is a program which analyzes a dataset and the users can hang a wagon onto the train with their self-made analysis tasks. Therefore the data is in principle opened once and then analyzed with many different tasks at once. This should reduce the workload and speed up data analysis. However, as a downside, it is harder to change certain input aspects on the Grid, because then it has to be applied to all servers participating on the Grid and potentially harm the analysis of other users.
To use a finer centrality binning on the data, new OADB (**O**ffline **A**nalysis **D**ata **B**ase) files are needed. The OADB files define histograms which have to be available for each specific centrality bin. They denote the signal in the V0 detector to the centrality percentile. These could be uploaded to the grid but the procedure is harder and takes longer. As a solution now the GSI cluster was used to analyze the data. For this purpose, the whole October 2015 dataset (LHC15o_pass1_pidfix) of Pb-Pb collisions was copied to the client. The GSI cluster has a similar train operation but it is more flexible on choosing custom files for the centrality selection.

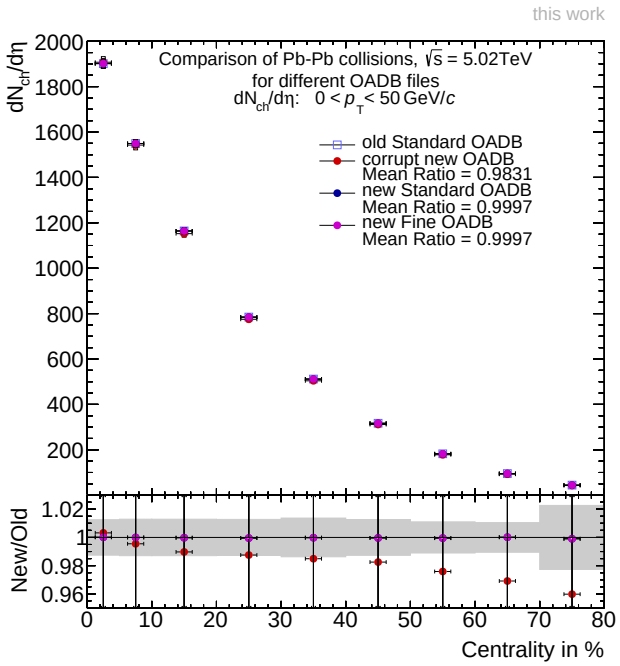

Figure 4.2: The differences on the multiplicity regarding the OADB files is shown. The ratio of the old corrupt OADB files deviates up to 4%.

The new OADB files are tested to check if there are differences between them and the old one which might effect this analysis. For this purpose, standard binning

was chosen for all used datasets. For the purpose of these crosschecks, two new OADB datasets were provided with one being for standard binning and the other one being for fine binning. At first a corrupted OADB dataset was provided which had a wrongfully assigned in the anchor point and therefore a rising discrepancy between old and new. This was fixed in the new OADB files as shown in figure 4.2. As can be seen there is some discrepancy between old and new OADB files exists, especially for higher centrality but the difference is negligible.

4.2 Event and track selection

The data which is now acquired also needs to be selected to minimize background sources and noise. There are three selections taken place in the data analyzing process. At first, there is the minimum bias trigger which is applied directly during data taking. Then there is an event selection which also inherits the centrality selection criteria and finally there is the track selection where different conditions are applied to the reconstructed tracks to ensure best track quality and high efficiency for primary particles. After applying the event selection, there are now 32.6 million minimum bias events in Pb-Pb collisions and 1.16 million minimum bias events in Xe-Xe collisions. The track selection does not affect this value since it only cuts tracks not events.

Minimum bias trigger: The **M**inimum **B**ias (MB) trigger is a high-efficiency trigger optimized for hadronic collisions. It needs a signal from the V0A and V0C detectors and additionally a coincidence between the ZNA and ZNC. The letters A and C hereby denote opposite sites of the detector as explained in section 3.2. This is done online, when the beam is running. In addition, offline the beam induced background and electromagnetic interactions are being rejected using the timing signal of the V0A and V0C detectors.

Event selection: The offline event selection is repeating the online MB trigger using the same quantities to reduce events triggered by noise. Only tracks within $|\eta| < 0.8$ are considered since this is the acceptance region of the detector with an almost flat efficiency. Additionally, vertex cuts are applied on the Z-vertex (Z_V^{SPD}). At first, the resolution of Z_V^{SPD} is required to be better than 0.25 cm and second the difference between the Z_V from tracks and tracklets in SPD is required to be $|Z_V^{Track} - Z_V^{SPD}| < 0.5$ cm. Also, only events with Z_V within 10 cm to the nominal center of the detector are accepted.

Track selection: Particle tracks are measured in the range of $|\eta| < 0.8$ and $0.15 < p_T < 50$ GeV/c. Most particles are produced in the bulk region of $p_T < 3$ GeV/c. Therefore, especially this region has an abundance of tracks and quality can be favored over quantity in the low p_{T} region. The criteria for the track selection (also called track cuts) are summarized in table 4.1. Since Xe-Xe collision were taken at a

Criteria	Variable	Constraint
DCA along z-axis	$\mathrm{DCA_Z}$	≤ 2 cm
χ^2 per ITS cluster	χ^2_{ITS}	≤ 36
ITS refit required		True
Require hits in the SPD		True
DCA in radial direction	$\mathrm{DCA_r}$ (Pb-Pb)	$< 0.0182 + 0.035\ (\mathrm{p_T/GeV/c})^{-1}$cm
	$\mathrm{DCA_r}$ (Xe-Xe)	$< 0.0119 + 0.049\ (\mathrm{p_T/GeV/c})^{-1}$cm
Track length in active volume	$\mathrm{L_{active}}(p_T)$	> 130 cm
Number of crossed rows	$\mathrm{n_{rows}}$	$> 0.85 \cdot \mathrm{L^{eff}_{active}}(p_T)$
Number of TPC clusters	$\mathrm{n_{cluster}}$	$> 0.7 \cdot \mathrm{L^{eff}_{active}}(p_T)$
Crossed rows over findable clusters	$\mathrm{n_{rows}/n_{findable}}$	≥ 0.8
Fraction of shared TPC clusters	$\mathrm{n_{shared}/n_{cluster}}$	≤ 0.4
χ^2 per TPC cluster	χ^2_{TPC}	≤ 4
Width of exclusion zone	$\mathrm{W_{dead-zone}}$	3 cm
TPC refit required		True
Reject kinks		True
$1/p_{\mathrm{T}}$ dependent slope	α_{slope} (Pb-Pb)	1.5
	α_{slope} (Xe-Xe)	0.7
χ^2 TPC-ITS	$\chi^2_{\mathrm{TPC-ITS}}$	≤ 36

Table 4.1: Track selection criteria for Pb-Pb and Xe-Xe collisions at 5.02 and 5.44 TeV respectively. Two values have been changed between Xe-Xe and Pb-Pb collisions to accommodate the lower magnetic field (0.5 T to 0.2 T). These are marked in red for the Xe-Xe values. The track selection is the same as reported in [42, 41].

different magnetic field compared to previous runs, the track selection was modified in cuts which rely on the p_{T} of the particle. The track selection can be divided into an ITS and TPC selection. The criteria for the different cuts are now discussed briefly.

ITS and DCA selection: The selection criteria for the ITS focus on a good DCA (**D**istance of **C**losest **A**pproach to the primary vertex) resolution and a good p_{T} resolution. For this reason, at least one hit in the SPD and a refit of the ITS tracking is required. Additionally tracks are rejected if they exceed a χ^2_{ITS} cluster of 36.
The DCA selection is required to minimize the number of secondaries compared to primary particle numbers. Secondaries generally result in a larger DCA and are therefore easily filtered using DCA cuts. There are two constraints on DCA in the selection, first the DCA_Z should be less than 2 cm and second that $\mathrm{DCA}_r < 7\sigma_0(p_T)$. With the approximation for the standard deviation of the impact parameter

resolution being $\sigma_0(p_T) = (26 + 50/(p_T\ /\mathrm{GeV/c})^{-1})\mu$m for Pb-Pb collisions and $\sigma_0(p_T) = (17 + 70/(p_T/\mathrm{GeV/c})^{-1})\mu$m for Xe-Xe collisions. This cut becomes more restrictive for higher p_T since the vertex resolution increases.

TPC selection: First, a track cut on the length in the TPC volume is applied due to the efficiency of track reconstruction of the TPC decreasing at the edges of segments of the TPC, which leads to increased systematic uncertainty especially at intermediate p_T. The maximum radial length a particle can pass through the TPC is 160 cm. To also account for the shorter track length at low transverse momentum, a p_T dependent variable is applied which describes the slope. The effective length is then calculated using $L^{\mathrm{eff}}_{\mathrm{active}}(p_T) = L^{\mathrm{cut}}_{\mathrm{active}} - |1/p_T|^{\alpha_{\mathrm{slope}}}$, the tracks are now accepted if $L_{\mathrm{active}} > L^{\mathrm{eff}}_{\mathrm{active}}(p_T)$. The slope dependence α is also dependent on the magnetic field and therefore changed between Pb-Pb and Xe-Xe collisions. This also allows for the width around the boundaries of a sector $\mathrm{W}_{\mathrm{dead-zone}}$, the dead-area. Additionally to the length requirements, a minimum number of crossed rows ($\mathrm{n}_{\mathrm{rows}}$) is set to $0.85 \cdot L^{\mathrm{eff}}_{\mathrm{active}}(p_T)$. A row counts as crossed when a cluster is found in the row or in the two neighboring rows (to account for missing clusters). The minimum number of clusters found is $> 0.7 \cdot L^{\mathrm{eff}}_{\mathrm{active}}(p_T)$. The number of findable clusters $\mathrm{n}_{\mathrm{findable}}$ is gathered from track properties, based on the possible maximum number of clusters. The ratio of $\mathrm{n}_{\mathrm{rows}}/\mathrm{n}_{\mathrm{findable}}$ is set to be at least 0.8. To reduce the number of fake tracks, a maximum for the ratio of $\mathrm{n}_{\mathrm{shared}}/\mathrm{n}_{\mathrm{cluster}} \leq 0.4$. Hereby, $\mathrm{n}_{\mathrm{cluster}}$ describes, that all clusters which are taken into account for fitting whereas $\mathrm{n}_{\mathrm{shared}}$ are all clusters assigned to more than one track. For good quality tracks, the χ^2_{TPC} is set to be lower or equal than 4.
A sophisticated cut on TPC and ITS is established in form of the $\chi^2_{TPC-ITS}$ variable. This takes into account the five track parameters and their uncertainties. The purpose is to remove tracks which are based on wrongly assigned ITS clusters that scatter in the detector material between ITS and TPC.

4.3 Corrections

After applying the event and track selection, the data is available as a raw yield p_T spectrum $\gamma_{\mathrm{raw}}(p_T, \eta)$. This yield is getting corrected by three contributions. The first being the acceptance and efficiency correction that are determined through Monte Carlo simulations. Second, a particle composition correction is applied and last, the effect of a finite transverse momentum resolution is correct for. It's effect is largest at higher momentum. The general form of application can be seen in equation 4.1.

$$\begin{aligned}\gamma_{\mathrm{corrected}}(p_T, \eta) \quad = \quad & C_{\mathrm{acceptance\&efficiency}}(p_T) \cdot \alpha_{\mathrm{ParticleComposition}}(p_T) \cdot \\ & C_{\mathrm{secondaries}}(p_T) \cdot \alpha_{\mathrm{sec.scaling}}(p_T) \cdot \\ & C_{\mathrm{p_T-resolution}}(p_T) \cdot \\ & \gamma_{\mathrm{raw}}(p_T, \eta) \end{aligned} \tag{4.1}$$

Firstly a correction for tracking inefficiencies and detector acceptance is applied ($C_{\text{acceptance\&efficiency}}$) which is multiplied by the factor of the particle composition correction since the MC samples do not represent the particle species correctly. Afterwards the contamination from secondaries ($C_{\text{secondaries}}$) is subtracted which effects mostly the low p_{T} regime. And finally, the p_{T} spectra is unfolded and a data-driven resolution correction is formed and applied ($C_{\text{p}_{\text{T}}-\text{resolution}}$). The other two corrections are all estimated using MC simulations. Since the simulation on secondaries does not represent the data perfectly the MC-driven corrections are matched to data resulting in data-driven reweighting factors ($\alpha_{\text{ParticleComposition}}$ and $\alpha_{\text{sec.scaling}}$).

4.3.1 Acceptance and efficiency correction

To correct the acceptance and efficiency, a Monte Carlo data sample is used for Pb-Pb and Xe-Xe collisions. These Monte Carlo data samples are generated using the event generator HIJING [43], which is used to simulate heavy-ion collisions. In the simulation the generated particles are propagating through a representation of the full ALICE detector. This simulation is generated using the GEANT framework [44]. By traversing this modeled detector, each step is tracked and each detector response is simulated. Afterwards, the complete track reconstruction is done on the simulated detector response. This results in a complete data set with information of each particle at any given point. This Monte Carlo data sample is used to correct for the efficiency and acceptance of the ALICE detector. In figure 4.3 the acceptance and efficiency for Pb-Pb and Xe-Xe collisions are shown.
The particular shape of this curve comes from various effects. The low efficiency in the low p_{T} part comes from the strong curvature of tracks and therefore higher energy loss in the detector material. That is also the reason why the Xe-Xe and Pb-Pb points seem to be shifted. This is due to the change of the magnetic field from 0.5 T to 0.2 T. The next drop at $p_T \approx 1GeV/c$ comes from the requirement of a minimal track length (L_{active}). The minimal track length also scales with the magnetic field, thus the change from Xe-Xe to Pb-Pb collisions. For high p_{T} the efficiency reaches a plateau which resembles the maximum efficiency before it drops for higher p_{T}. To be noted however that the gas composition of the TPC has changed from Ar-CO_2 for Pb-Pb collisions to Ne-CO_2 for Xe-Xe collisions. This also effects the tracking efficiency of the detector.

Centrality	0 - 5 %	5 - 10 %	10 - 20 %	20 - 30 %	30 - 40 %
Ratio to MB (Pb-Pb)	0.984	0.996	1.003	1.008	1.010
Ratio to MB (Xe-Xe)	0.995	1.000	1.003	1.005	1.006
Centrality	40 - 50 %	50 - 60 %	60 - 70 %	70 - 80 %	
Ratio to MB (Pb-Pb)	1.011	1.012	1.013	1.013	
Ratio to MB (Xe-Xe)	1.007	1.008	1.008	1.008	

Table 4.2: Ratios of selected tracking efficiencies to minimum-bias for Pb-Pb and Xe-Xe collisions.

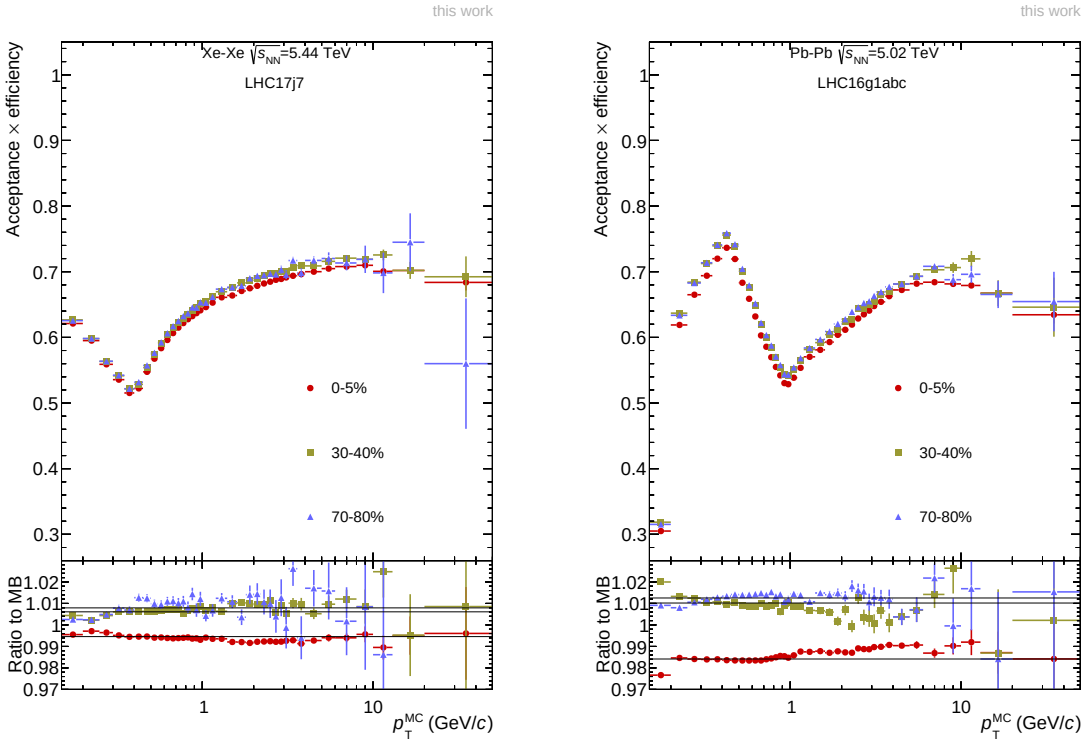

Figure 4.3: Tracking efficiencies and acceptance for a selection of centralities shown on the left for Xe-Xe collisions and on the right for Pb-Pb collisions.

ALICE is designed for high multiplicity with its TPC detector. This results in only a small scaling factor of efficiency with centrality. This is expressed in table 4.2 with the ratio to Minimum Bias (MB) collisions. Only the most central collision classes deviate more than 1 % from the MB efficiency. Because of this there was no separate Monte Carlo data sample in 1 % centrality bins since the efficiency is nearly independent of centrality. Second, a finer binned Monte Carlo sample, when having the same total amount of Minimum Bias events, would have around 17000 events per centrality bin which would increase statistical uncertainties by a larger amount than the possible gain of a fine binned Monte Carlo data sample.

4.3.2 Particle composition correction

It has been observed in Pb-Pb collisions, that the Monte Carlo generators produce different relative abundances of particle species compared to data.
Especially since the HIJING event simulator does not include a hydrodynamical evolution of the system, which is crucial for Σ-baryons, which depend strongly on the centrality of the collision. The Σ-baryons are estimated by a data-driven method using the neutral Λ-baryon yield which has equal strangeness and a similar mass. The Σ-baryons itself were not measured and a data driven p_{T} distribution is needed.

For this the Λ-spectrum is scaled by the ratio of the cross sections of Σ-baryons to Λ-baryons from MC.

To correct this inaccuracy of particle composition the efficiencies of particle species and their abundances based on data is used. The particle composition correction reaches around 8% for central collisions but decreases with increasing centrality. This is a direct result from strange baryons which are underestimated by HIJING in central collisions. This reweighting factor is only available in wider centrality[1] bins since identified particle spectra are limited as well as MC simulations.

For the Xe-Xe collisions, the same particle composition correction factors were used but for comparable values of N_{part} and N_{COLL}. An independent measurement for Xe-Xe collisions is more difficult since there is no measurement of identified particle production yet.

4.3.3 Secondary contamination

The raw transverse momentum spectrum contains even after the selection process contamination from secondary particles. Their origin is within weak decays of particles produced in the initial collision or from reactions of particles with the detector material. Using MC simulations, the contribution of secondaries can be estimated, which is shown in figure 4.4. The contamination for low p_T is more than 10% but decreases with increasing p_T rapidly below 1%. Secondary particles are more abundant in the low p_T regime since they carry only a fraction of the momentum of their mother particle. Additionally most particles in general are produced in the low p_T regime in high energy hadron collisions. The secondary contamination is also significantly centrality dependent as figure 4.4 shows. As depicted with the particle composition correction, Monte Carlo event generators fail to describe relative particle fractions accurately. Secondary particles are also not well described.

Secondaries should be identifiable by examining the DCA_r distribution. Since they do not originate from the primary vertex, no matter if they are decay daughters or remnants of secondary interactions in the detector, the DCA distributions width is affected. To get a correction factor, the MC and data DCA_r distribution are used but the MC distributions is split in primaries and secondaries. The MC distributions are now fitted using templates and the two template fits combined are then compared to the data distribution and the ratio is taken. For Xe-Xe collisions, three template fits were used. For this purpose the MC sample was divided into primaries, secondaries from decay and secondaries from material. Since normal track cuts are such that contamination by secondaries is minimized the DCA_r and $\chi^2_{TPC-ITS}$ selections are not applied. The correction factor is then calculated for three different p_T intervals spanning the complete p_T area, since statistics is limited in MC samples. The resulting ratio is then used to scale the contamination factor.

[1] Centrality intervals used are 0-5%, 5-10%, 10-20%,20-40%, 40-60% and 60-80%.

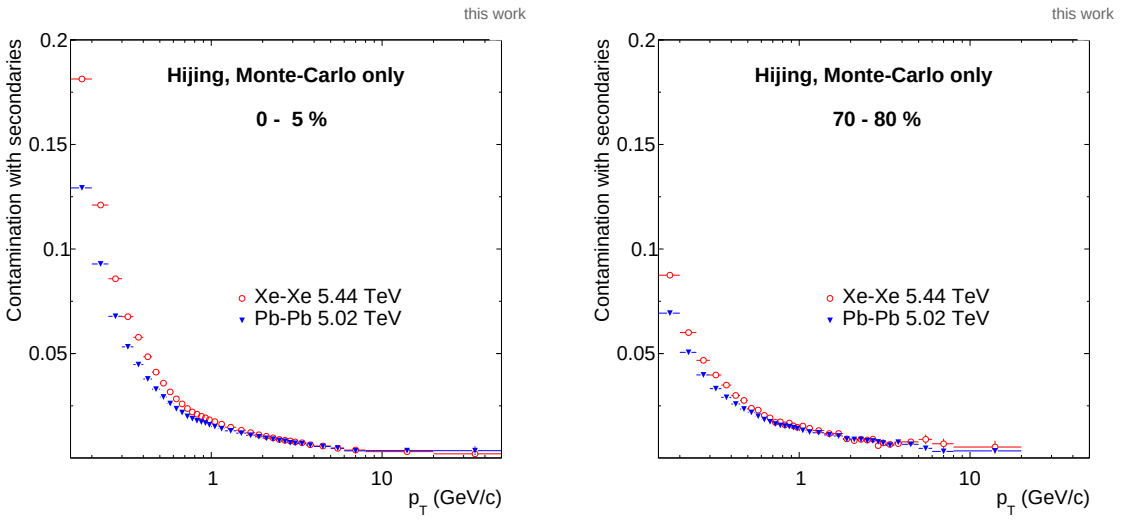

Figure 4.4: Secondary contamination for Xe-Xe and Pb-Pb collisions are shown on the left plot for central collisions and on the right for peripheral collisions.

4.3.4 Transverse momentum resolution correction

The transverse momentum of a particle is reconstructed from a helix fit. This is needed since particles with a $p_T = 1$ GeV/c have a radius of ~ 6.6 m, which is significantly larger than the TPC's outer radius of 2.5 m. The precision of the p_{T} measurement is constrained mainly by two effects. For low p_{T} particles, by the scattering of the particle in the detector layers and for high p_{T} particles by the finite spatial resolution of the TPC. The spatial resolution itself is independent of momenta, but becomes more significant at high p_{T}. Therefore the resolution can not be neglected at high p_{T} since the curvature of the track is lower. For each track, the resolution is estimated individually during tracking and reconstruction. It is clearly visible that at first less high p_{T} tracks are reconstructed and that these tracks have a worse resolution. Also visible is the effect of multiple scattering at low p_{T} which worsens the resolution, since the particles interact with the detector material. The effect of the finite relative momentum resolution is tested by first applying a parametrization to the p_{T} spectra by using a power-law fit. Now an unfolding of the p_{T} distribution is done by taking a randomly picked p_{T} value from the parameterization, which is then smeared with a random-choice based Gaussian distribution with a mean of zero and a width of the relative momentum resolution. This smeared p_{T} distribution is then compared to the unsmeared one and the ratio of the two is applied as a correction factor for tracks with $p_{\mathrm{T}} > 10$ GeV/c. Although the relative momentum resolution has no centrality dependence, the correction factor shows a dependence since the spectra hardens with more peripheral collisions. For Xe-Xe collisions, the correction becomes even more important since the magnetic field was changed to a lower value which means that the curvature of the tracks is

less and the reconstruction deteriorates. In Pb-Pb collisions at $\sqrt{s_{\mathrm{NN}}} = 5.02$ TeV the factor varies between 1% and 2% at high p_{T} for central and peripheral collisions respectively. For Xe-Xe collisions this increases to 3% and 4%. This correction was not redone for the final matched bin widths due to centrality dependence being low. Therefore the corresponding values in the available Pb-Pb collision data was used.

4.3.5 pp reference

For calculation of the $\mathrm{R_{AA}}$, a reference to proton-proton collisions at the same center of mass energy is needed. The $\mathrm{R_{AA}}$ is in fact the ratio of heavy-ion collision spectra and p-p spectra scaled with the nuclear overlap function $\mathrm{T_{AA}}$. For the pp reference at $\sqrt{s} = 5.02$ TeV, a measurement in RUN2 of the LHC was provided. This contains the charged-particle production at p-p collisions and can be directly compared to the heavy-ion collision charged particle production. The pp reference spectra can be seen in figure 4.5.
For Xe-Xe collisions the collision energy changed to $\sqrt{s} = 5.44$ TeV. There was no pp run at the LHC with this beam energy and there will not be one in the foreseeable future. To overcome this challenge the spectra was extrapolated from the $\sqrt{s} =$ 2.76, 5.02 and 7 TeV pp runs at the LHC. For this a power law dependence was assumed for fixed p_{T}. A second possibility was to generate a distribution using MC event generators such as PYTHIA 8.
The extraction of this pp reference is explained in [42] and leads to the same results within 2% to the first method. But in the end the data driven approach was used.

4.3.6 Nuclear overlap function in fine binning

The nuclear overlap function ($\mathrm{T_{AA}}$) is describing the overlap of two colliding nuclei in terms of inverse cross section. It is calculated using Monte Carlo Glauber models [7, 45]. These values were initially provided in 5% centrality bins which leads to large deviations in the comparisons of the $\mathrm{R_{AA}}$ in the end. Therefore, newer values were provided with a finer binning of 1% centrality. These values are then tested for their consistency with the previous values. It has to be noted however, that a simple average of five 1% bins and comparing to one 5% bin does not provide accurate results. This can be seen in figure 4.6. The solution is to not use the average but rather the weighted average in form of the center of gravity (centroid) since the values are not linearly distributed but on a curved line. For the center of gravity, a fit has to be made to the data sample. The centroid is then calculated as follows

$$\bar{x} = \frac{\int_a^b x \cdot f(x) dx}{\int_a^b f(x) dx} \tag{4.2}$$

with f(x) denoting the fit function and a and b denoting the centrality interval. For comparison, the finer binned values were fitted and their centroid taken and

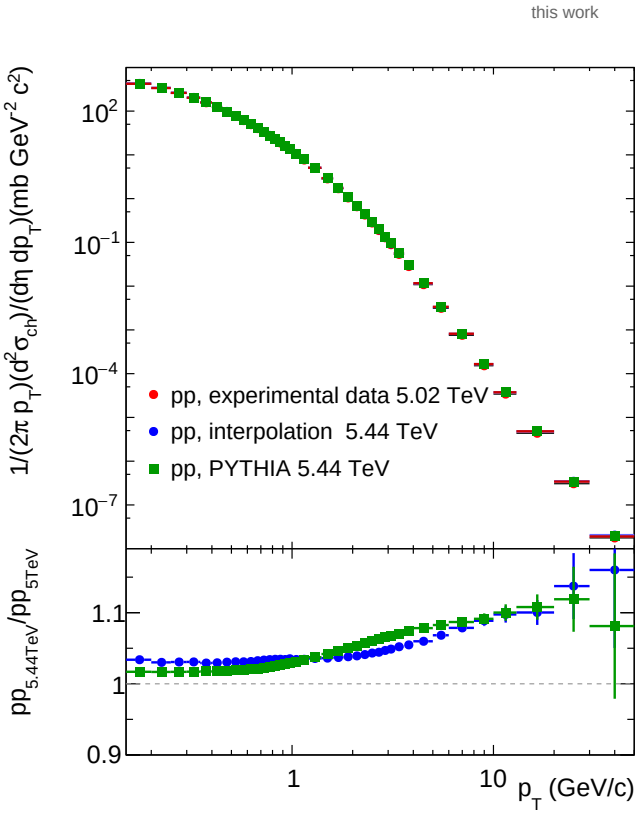

Figure 4.5: The used pp reference for Xe-Xe and Pb-Pb collisions and their ratio to the 5.02 TeV pp reference is shown. Additionally an estimation of the pp reference using PYTHIA for $\sqrt{s_{\mathrm{NN}}} = 5.44$ TeV is presented.

also the larger binned values. The comparison was then made between the larger binned values and the average of the finer bins, the larger binned values against the centroid of the finer bins and the centroid of the larger bins over the centroid for finer bins. The result of this comparison is shown in figure 4.6. The average seems to best describe the larger binned data with the smallest deviation over all and more consistent throughout. The ratio of the two centroids leaves a linear shape and the ratio of the 5 % bins to the centroid leaves a shape of a third degree polynomial.

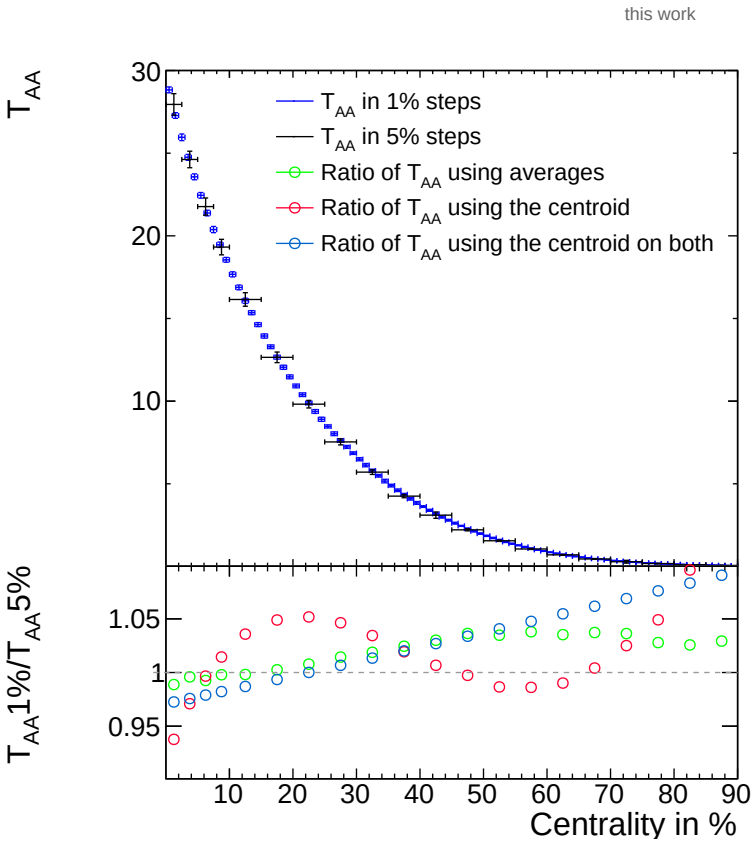

Figure 4.6: Comparison of the T_{AA} values in 5% centrality steps and 1% centrality steps. For the ratio three different methods were used including the average and the centroid.

4.4 Systematic uncertainties

For the systematic uncertainties several contributions are considered which are discussed in detail. The contributions come from the analysis itself and the performed corrections. The systematic uncertainties are in most cases p_T dependent. If not, they are applied to the whole p_T range as a constant. Also, the systematic uncertainties are calculated for every centrality region used since they depend substantially on the centrality. The complete systematic uncertainties are listed in table 4.3 and the p_T dependence is shown in figure 4.7. Also the matched multiplicity bins are shown with their own calculated uncertainties. The single contributions are now discussed and explained individually.

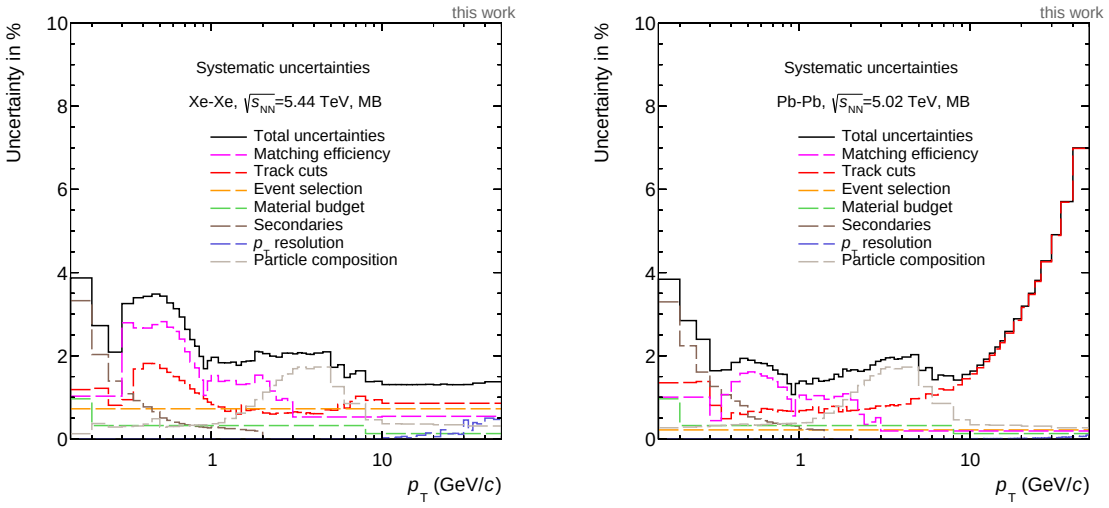

Figure 4.7: Left the complete systematic uncertainties for Xe-Xe collisions are shown whereas on the right the systematic uncertainties for Pb-Pb collisions are shown. The systematic uncertainties for all centrality ranges are available in the appendices A.1, A.2 and A.3.

4.4.1 Efficiency correction

The raw data samples are corrected for tracking efficiency by the MC simulations, as explained in section 4.3. No direct estimation of the uncertainty can be made but a quantity which is available in data and MC can be exploited to be used as uncertainty. For this purpose, the matching efficiency $\epsilon_{\text{matching}}$ is chosen. It is constructed by using the fraction of tracks reconstructed in the TPC to tracks with additional hits in the ITS.

$$\epsilon_{\text{matching}}(p_T) = \frac{dN_{\text{TPC-ITS}}/dp_T}{dN_{\text{TPC-only}}/dp_T} \tag{4.3}$$

By construction the TPC-ITS sample is a subsample of the TPC-only sample since it has additional requirements. The ratio of the matching efficiencies between MC and data is describing the uncertainty of the applied efficiency correction.

$$\text{Uncertainty}(p_T) = \left| 1 - \frac{\epsilon^{MC}_{\text{matching}}(p_T)}{\epsilon^{Data}_{\text{matching}}(p_T)} \right| \tag{4.4}$$

The deviation of this ratio from unity was in the past used as an uncertainty. Secondary contamination however worsens this result. Therefore, the same procedure as for the secondaries is now used to scale the MC sample accordingly and afterwards the correction is gathered. This greatly improves the matching efficiency from around 4% to 1-1.5% uncertainty. For high p_{T}, the uncertainty is linearly extrapolated to decrease statistical fluctuations.

Source	**Uncertainty in %**					
	Pb-Pb, standard		Xe-Xe		Pb-Pb, matched	
	0-5%	70-80%	0-5%	70-80%	12-18%	74-83%
Efficiency corr.	0.82/0.33	0.99/0.20	2.03/0.4	2.15/0.54	1.25/2.47	1.08/0.19
Track selection	1.34/4.43	0.53/4.00	1.59/1.15	0.95/0.96	2.34/6.8	0.60/4.6
Event selection	0.07	0.11	0.36	1.06	0.57	0.09
p_{T} resolution	0/0.06	0/0.10	0/0.50	0/1.32	0/0.07	0/0.10
Particle comp.	0.31/0.26	0.31/0.46	0.32/0.32	0.33/0.44	0.30/0.29	0.31/0.46
Secondaries	1.7/0	0.88/0	1.41/0	0.63/0	1.36/0	0.88/0
Material budget	0.32/0.13					
Total	2.42/4.45	1.55/4.04	3.24 /1.41	2.76/2.19	3.13/7.30	1.63/4.63
Anchor point	0.06	3.50	0.06	3.23	0.32	3.85

Table 4.3: Systematic uncertainties in units of percent for the different data samples used in the analysis and their sources. The numbers are averaged in different p_{T} intervals from 0.2-0.5 GeV/c (left side) and 40-50 GeV/c (right side). For the combined total result all contributions are added in quadrature with the exception of the anchor point contribution which is used as an overall normalization uncertainty.

4.4.2 Anchor point shift

The centrality estimation is using an anchor point as described in section 3.3. The anchor point is then shifted by its uncertainty of $90\% \pm 0.5\%$. The systematic uncertainty was then calculated by recalculating the centrality boundaries accordingly. This results in a change of centrality for all centrality classes and results in a larger shift of values for more peripheral collisions. This uncertainty is p_{T} independent and is therefore applied as a normalization uncertainty. The result of an incorrect assigned anchor point can be seen in the wrong OADB files in section 4.1.3 and figure 4.2.

4.4.3 Track selection

To get the systematic uncertainties due to track selection, all track selections were varied within reasonable limits. For this purpose the whole analysis, was redone for each new track cut. To get the uncertainties, the spectra are compared to the nominal value and the corresponding ratio is made. For changes to larger and smaller cut values only the variations which lead to higher deviations were considered and taken as uncertainties for this specific track cut. This was done for every centrality and in MC and experimentally data. To eliminate statistical fluctuations the different contributions were fitted towards higher p_{T}. The variation of the parameters can be seen in table 4.4 and the individual track cuts uncertainties can be seen in figure 4.8.

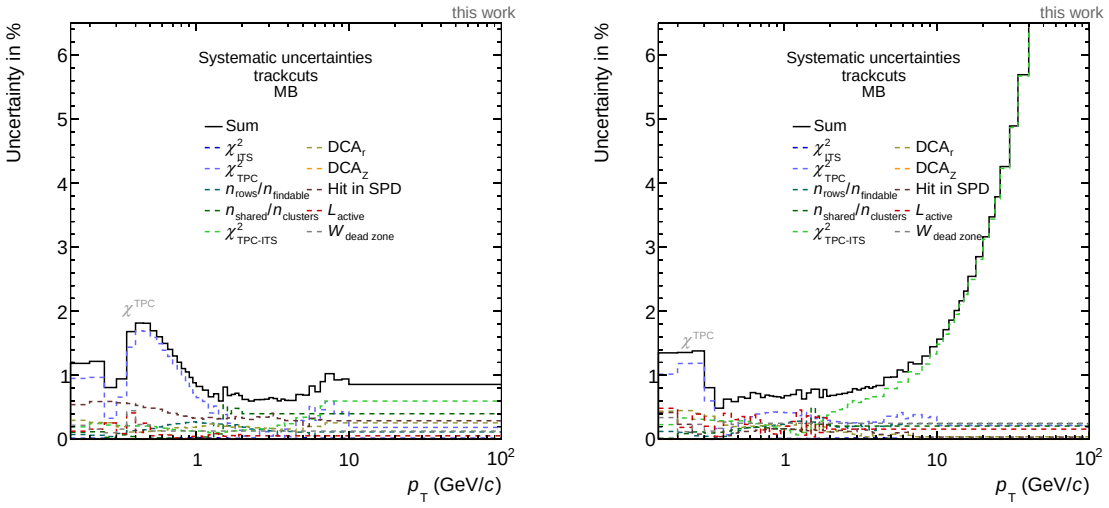

Figure 4.8: On the left the complete track related systematic uncertainties for Xe-Xe collisions are shown, whereas on the right the systematic uncertainties for Pb-Pb collisions are shown. The uncertainty is also split into their individual contributions which are then added in quadrature for the final result. The systematic uncertainties for all centrality ranges are available in the appendices A.4 and A.5.

4.4.4 Event selection

For heavy-ion collisions, the trigger and vertex determination are supposed to be fully efficient. Therefore, the only remaining uncertainty comes from the selection of the vertex position along the beam pipe Z_v. The selection on the Z_v coordinate was varied from normal ± 10 cm to ± 5 cm and ± 20 cm in data and simulation. The resulting spectra were then compared to the nominal value and the ratio is taken as shown in figure 4.9. To remove present statistical fluctuations and since the ratio is p_{T} independent, a constant was fitted to the ratio. The constant of the largest deviation is then used as uncertainty for all p_{T} bins. The uncertainty is small for Pb-Pb in standard binning. However, it is increased for Xe-Xe and matched Pb-Pb bins and possibly correlated to the number of events.

4.4.5 p_{T} resolution

For the p_{T}-resolution correction an, unfolding based on a power-law parametrization was used. The first source of uncertainty is this parametrization which is varied from its lower boundary from 10 GeV/c to 8 GeV/c and 12 GeV/c. This is then compared to the nominal correction factor and the ratio directly contributes to the uncertainty. The second source is the smearing which is additionally applied to the Gaussian as explained in section 4.3.4. To estimate this effect, the p_{T} resolution correction is

Selection criteria	Lower	Nominal	Upper
DCA_r	$4\sigma_0$	$7\sigma_0$	$10\sigma_0$
χ^2_{ITS}	25	36	49
Hit in SPD	not required	required	-
DCA_Z	1 cm	2 cm	5 cm
$L_{active}(p_T)$	120 cm	130 cm	140 cm
$n_{rows}/n_{findable}$	0.7	0.8	0.9
$n_{shared}/n_{cluster}$	0.2	0.4	1
χ^2_{TPC}	3	4	5
$W_{dead-zone}$	2 cm	3 cm	4 cm

Table 4.4: Variation of the nominal track selection to get the systematic uncertainties. Lower and upper hereby refer to variations which are lower or higher than the nominal value. For a hit in the SPD, only a variation from required to not required was made.

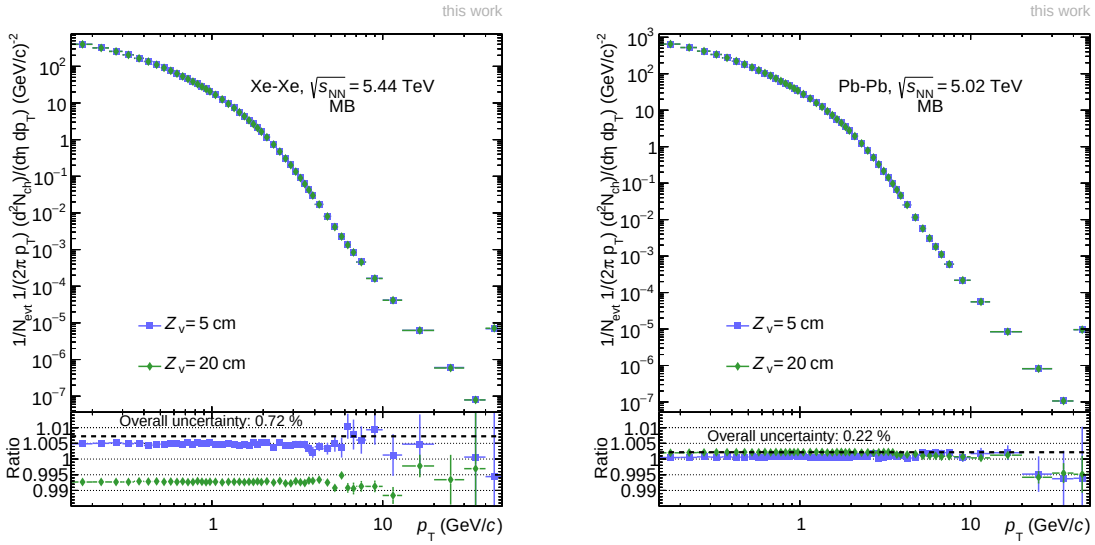

Figure 4.9: The determination of the event selection related systematic uncertainty is estimated on the left for Xe-Xe collisions and on the right for Pb-Pb collisions. The ratio at the bottom panels are taken with respect to the nominal spectra with a $Z_v = 10$ cm. The result with the larger divergence is then used and fitted with a constant. This constant is then taken as, systematic uncertainty.

calculated without extra smearing and then compared to the nominal case. Both contributions are then added in quadrature.

4.4.6 Particle composition

As explained in section 4.3.2, the particle composition correction relies on measured data and some assumptions. Both contribute to the systematic uncertainty. At first, the influence of the data of the analyzed particle species has to be evaluated. For this, the individual transverse momentum distributions were varied within their uncertainties. The change in the correction factor is then used as uncertainty. Second, the contribution of Σ-baryons is estimated using Λ-baryons which adds an extra uncertainty to the contribution. The remaining MC-only particles also contribute to the uncertainty.

4.4.7 Material budget

As the corrections depend on a simulation of the detector within the GEANT framework [44], the simulated description of the detector material is a source of uncertainty. The uncertainty is estimated by varying the material budget in the simulated detector by $\pm 7\%$ [46]. However, recent studies on the photon conversion method provided better constraints for the material budget of $\pm 4.5\%$ [47]. The simulation with these constraints has not been repeated and therefore the uncertainty provided by the first attempt is scaled by a factor of 4.5/7. Since the used MC samples are based on GEANT this uncertainty is also applied for all systems.

4.4.8 Secondary contamination

The uncertainty of the scaling factor has two contributions. At first, there is the variation of the number of templates used in the fits and second is the quality of the template fits. For the first contribution, the number of template fits is varied and their difference is added as uncertainty. For the quality of the templates, the RMS of the differences between fit and data is taken as contribution to the uncertainty. To propagate these uncertainties to p_{T} distributions the secondary scaling factor is varied by the uncertainties and applied to the raw spectra. The ratio of the spectra to the nominal one is then taken as secondary uncertainty. The contribution is significant and dominating at low p_{T} but negligible for high p_{T}. This can also be seen in figure 4.10 where the lower and upper spectra are plotted and their ratio to the nominal value.

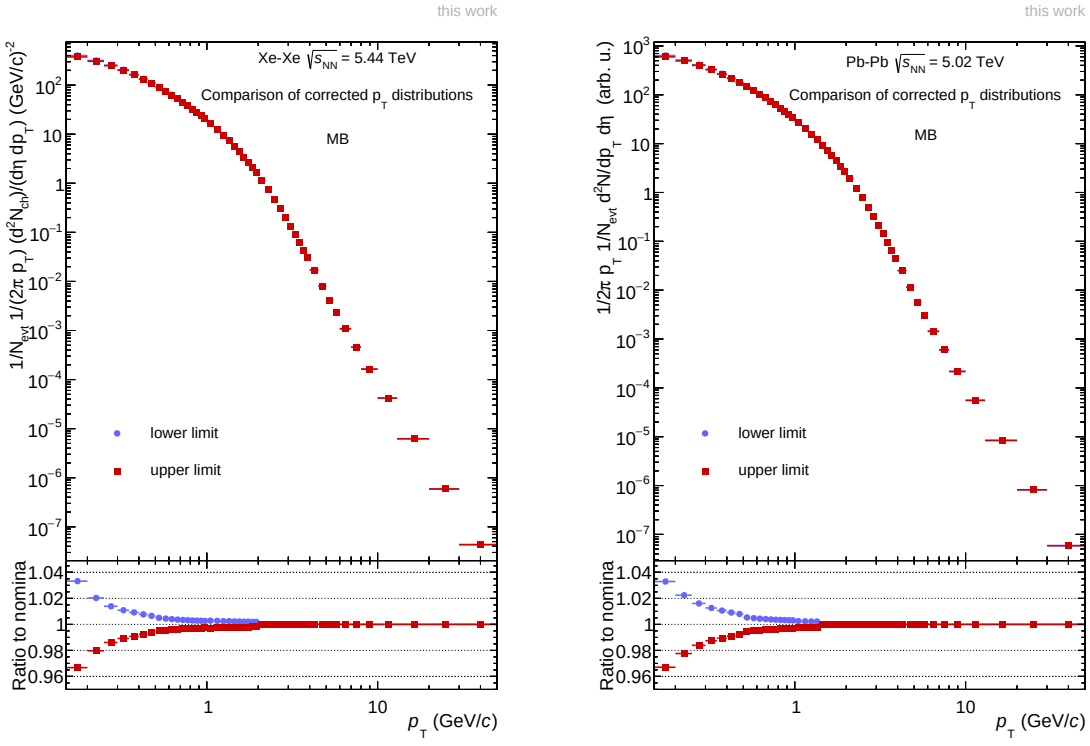

Figure 4.10: Systematic Uncertainty due to secondary contamination for Xe-Xe collisions and Pb-Pb collisions is shown. The ratio in the bottom panel is taken with respect to the nominal value. The result with the larger deviation is used as systematic uncertainty. For $p_{\mathrm{T}} > 1$ GeV/c, the systematic uncertainty from secondary contamination is negligible.

4.5 Determination of the multiplicity

To calculate the multiplicity $\frac{d\mathrm{N_{ch}}}{d\eta}$, the corrected spectra are used. To extract the multiplicity, the complete p_{T} range needs to be covered. Since the measurement only starts at a finite p_{T} of 0.15 GeV/c the spectra is fitted with a Hagedorn function:

$$\mathrm{Data}(p_T) = \alpha \frac{p_T^2}{\sqrt{m_\pi^2 + p_T^2}} \left(\frac{1 + p_T}{\gamma}\right)^{-\beta}, \tag{4.5}$$

with α, β and γ denoting fit parameters and m_π being the mass of the pion. The data is extrapolated inside the p_{T} region of 0-0.15 GeV/c. The fit itself is evaluated from 0.15-1 GeV/c and then extrapolated to 0. For extracting $\frac{d\mathrm{N_{ch}}}{d\eta}$, the extrapolated fit from 0-0.15 GeV/c and the data from 0.15-50 GeV/c is used. It is then integrated over the complete p_{T} range to get the $\frac{d\mathrm{N_{ch}}}{d\eta}$.
For the statistical uncertainties the fit is varied inside the errors of the parameters and the integral error is then added. For the systematic uncertainties, the fit range is varied from 0.15-1 GeV/c to 0.15-3 GeV/c. This can be seen in figure 4.11.

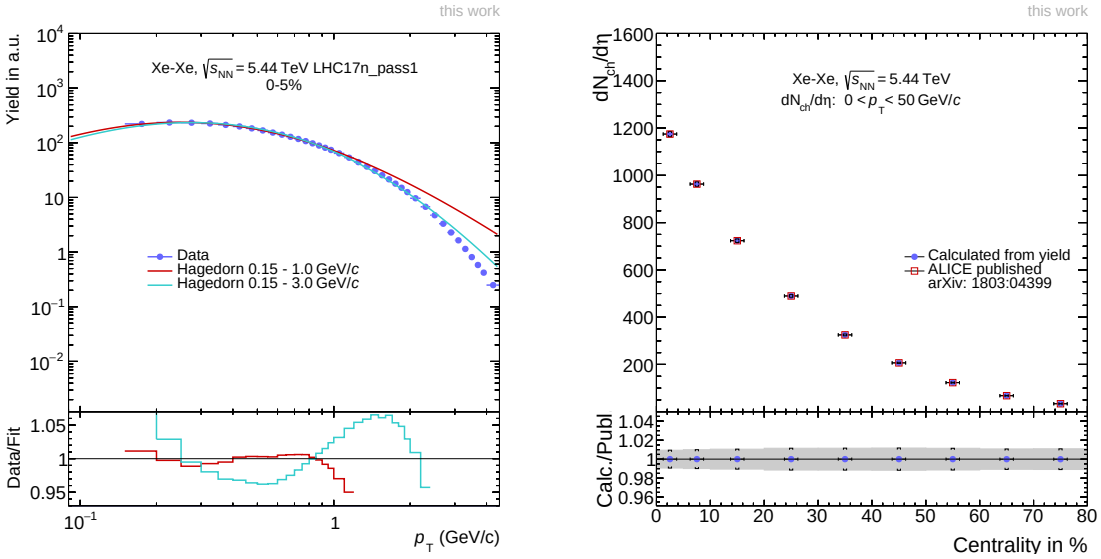

Figure 4.11: Left the systematic uncertainty of the multiplicity in Xe-Xe collisions through variation of the fit is shown. The spectra from data in a centrality of 0-5% is shown by in blue dots whereas the Hagedorn fits are represented in red and blue lines for normal and varied Hagedorn. On the right the multiplicity derived by the analysis (blue circles) compared to the published values (red rectangles) in Xe-Xe collisions is shown.

For Xe-Xe collisions a perfect agreement with the data from the published results [42] was achieved. Reproducing the results of the published paper was one goal of this thesis. The results are shown in table 4.5 and figure 4.11.

Centrality	Xenon $\frac{dN_{ch}}{d\eta}$ $\pm$ stat. $\pm$ syst.	extrapolation	Lead $\frac{dN_{ch}}{d\eta}$ $\pm$ stat. $\pm$ syst.	extrapolation
0-5%	$1174.50 \pm 0.21 \pm 11.04$	7.94 %	$1909.23 \pm 0.11 \pm 23.88$	7.69%
5-10%	$963.10 \pm 0.21 \pm 9.58$	8.06 %	$1545.47 \pm 0.18 \pm 20.88$	7.67%
10-20%	$723.49 \pm 0.13 \pm 7.61$	8.22 %	$1156.17 \pm 0.14 \pm 15.45$	7.68%
20-30%	$489.79 \pm 0.11 \pm 5.63$	8.53 %	$779.48 \pm 0.11 \pm 10.87$	7.93%
30-40%	$325.07 \pm 0.09 \pm 3.75$	8.84 %	$508.39 \pm 0.08 \pm 7.32$	8.30%
40-50%	$206.69 \pm 0.07 \pm 2.42$	9.29 %	$315.38 \pm 0.03 \pm 4.38$	8.85%
50-60%	$123.15 \pm 0.06 \pm 1.41$	9.78 %	$181.23 \pm 0.02 \pm 2.41$	9.44%
60-70%	$67.85 \pm 0.05 \pm 0.73$	10.34 %	$94.74 \pm 0.02 \pm 1.25$	10.17%
70-80%	$33.85 \pm 0.03 \pm 0.37$	11.12 %	$44.03 \pm 0.01 \pm 0.57$	10.95%

Table 4.5: Multiplicity calculated from the integrated yield for Xe-Xe and Pb-Pb collisions at standard centrality binning with the extrapolation to 0 GeV/c through a Hagedorn fit function. Extrapolation denotes hereby the percentage of the extrapolation compared to $\frac{dN_{ch}}{d\eta}$.

4.6 Matching multiplicity

After getting the multiplicity values for every bin in Xe-Xe, and for every 1% centrality bin in Pb-Pb collisions a matching of these two can be made. For this purpose the following algorithm was used. The general concept is to take a Xe-Xe centrality bin and its corresponding multiplicity and search for a centrality interval in Pb-Pb collisions with the closest average multiplicity. Within the interval, the multiplicity is calculated by taking the average over the intervals bin range. To achieve the closest multiplicity, the difference between the two has to be minimized. The only constraint is that the maximum number of Pb-Pb bins is set to be 10 which corresponds to a centrality interval of 10%. Also overlapping between two intervals is allowed for matching different multiplicity bins in Xe-Xe. The complete algorithm can be schematically seen in figure 4.13. This procedure is done for every centrality bin of Xe-Xe collisions.

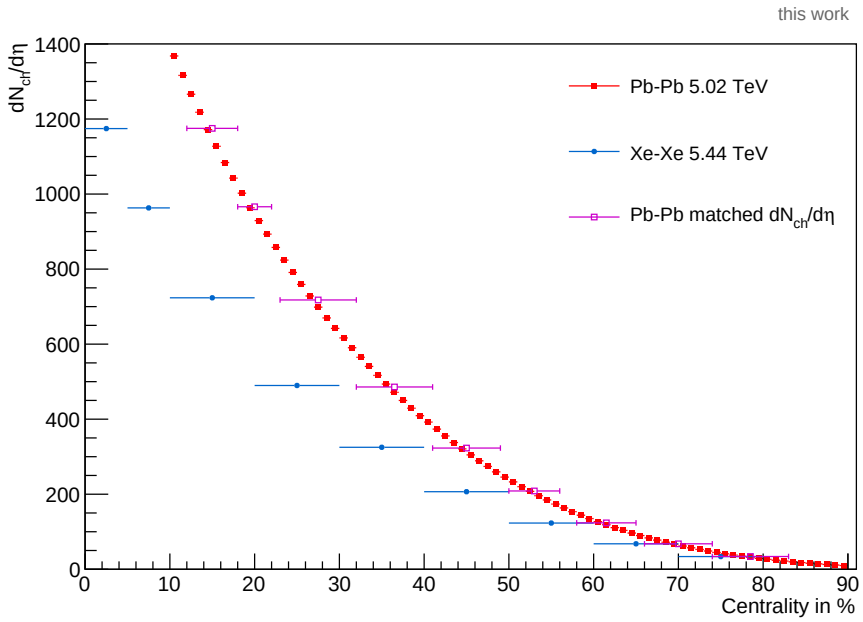

Figure 4.12: Multiplicity over centrality for the matching algorithm is shown. Visible are Xe-Xe (blue), Pb-Pb (red) and matched multiplicity Pb-Pb (purple) bins.

Not only the multiplicity was matched, but also the T_{AA}, N_{COLL} and the spectra. The first two are matched exactly the same way as for the multiplicity whereas the third is an abbreviation for matching different quantities of the corrected p_T spectra. For the spectra matching, the mean, mode and RMS from the underlying corrected p_T spectra are used and the ratio of each of these values, compared to the corresponding Xe-Xe bin value, is calculated. All three ratios are then added in quadrature with each other and the result is then optimized with the same procedure as for the multiplicity, to be as close to one as possible.

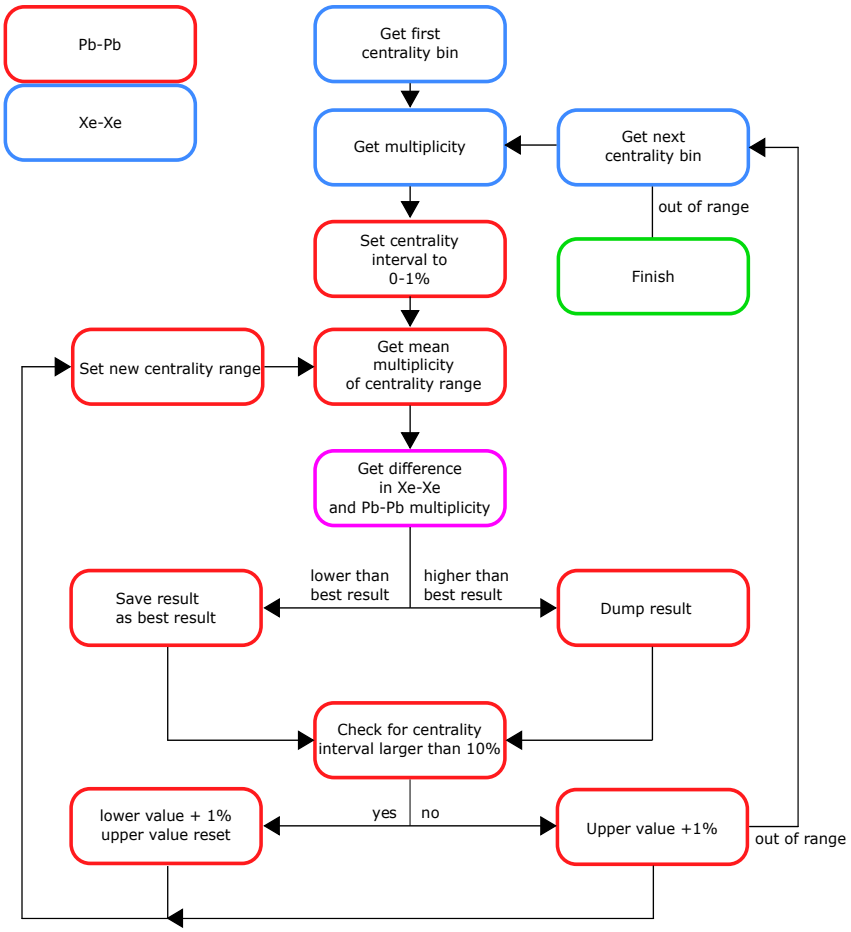

Figure 4.13: Schematic view of the algorithm used for matching the multiplicity between Pb-Pb and Xe-Xe collisions. The blue boxes represent the Xe-Xe data whereas the red boxes represent the Pb-Pb data. The purple box uses both collision systems for a comparison between them. The green box describes the end of the algorithm.

These other values are furthermore not chosen randomly but each directly corresponds to the multiplicity. The T_{AA} describes the overlap of the nuclei and therefore correlates directly with the centrality which is a multiplicity dependent variable. The N_{COLL} describes the number of binary collision which also correlates directly with the charged-particle production. The spectra matching is done on the same spectra from which the multiplicity is calculated.
The results of the matching procedure are centrality interval sizes. These can be seen in figure 4.14. It is visible that they all lie mostly in the same range of each other.

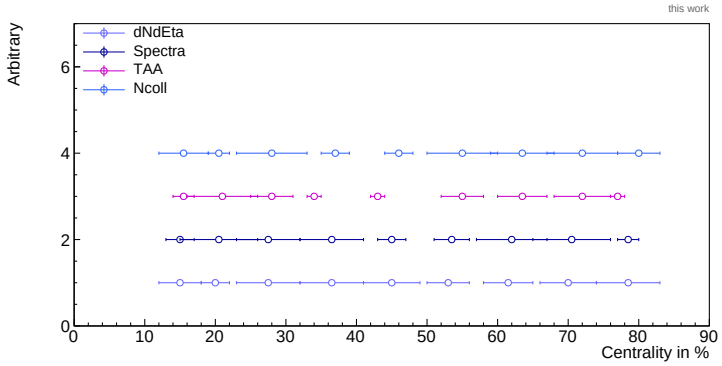

Figure 4.14: The individual bin width for each matching is shown as function of centrality. The y axis scaling in this case is arbitrary and has no value. The error bar in x direction shows the bin width of the specific matching method.

After matching the different variables, a set of intervals for each is gained. With these intervals, it is possible to calculate the multiplicity accordingly like in the previous section 4.5 which gains a multiplicity for each bin range and comparable values for the individual matching variables. The four different matching methods can be compared to each other and to the Xe-Xe values as shown in figure 4.15. This leads to the result that directly matching the multiplicity leads to the best matched multiplicity, by having the closest ratio to the Xe-Xe values compared to the other matching values. For T_{AA} and N_{COLL}, matching the ratio diverges more for peripheral collisions than the ratio of the matched multiplicity or spectra. For central collisions all matching values have a ratio close to one compared to Xe-Xe values. These defined intervals are then used as discrete data samples where the centrality bins are given by their intervals. These intervals can also be used to extract the R_{AA} for comparisons with the Xe-Xe R_{AA} within matched bins.

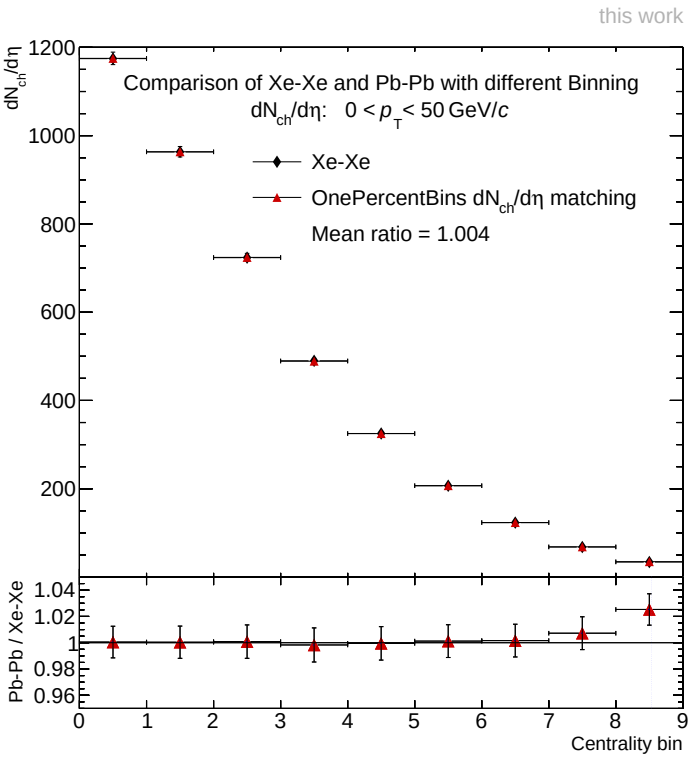

Figure 4.15: Multiplicity as function of centrality bin. The centrality bin is hereby increasing from central to peripheral collisions while the bins are the individually matched bins for the corresponding matching procedure.

5 Results

5.1 Comparison of R_{AA} in in Xe-Xe and Pb-Pb collisions at equal multiplicity

After matching the multiplicity and gaining a Pb-Pb collision data sample with nine centrality bins with the same multiplicity as in Xe-Xe collisions the R_{AA} values are compared to each other. The R_{AA} is calculated using

$$R_{AA}(p_T) = \frac{1}{T_{AA}} \cdot \frac{dN_{AA}(p_T)/dp_T}{d\sigma_{pp}(p_T)/dp_T}. \tag{5.1}$$

It is taking into account the corrected p_T spectra $dN_{AA}(p_T)/dp_T$ which are then normalized by the pp reference of the same energy and divided by the nuclear overlap function T_{AA}. When comparing the R_{AA} of Xe-Xe collisions to those of Pb-Pb collisions at the same centrality, as shown in [42] and also in figure 5.1, it can be seen, that they do not match and diverge further for more peripheral collisions. Therefore the suppression of particles is in Pb-Pb collisions harder than for Xe-Xe collisions at the same centrality.
The comparison of the two R_{AA} could lead to tests on the path length dependence for medium-induced energy loss. When assuming a simplified radiative energy loss scenario [48] the path length L of the parton goes in squared into the energy loss model $\Delta E \sim L^2$. For further investigation on the R_{AA} the goal of this thesis was to match the multiplicity in the two collision systems. The R_{AA} is then compared for same multiplicity bins in Xe-Xe and Pb-Pb collisions. The result can bee seen in figure 5.2. It is visible that the R_{AA} matches for central to mid-central collisions or the high multiplicity part for $\frac{dN_{ch}}{d\eta} > 489$, but a divergence for peripheral collisions is still visible.
When the R_{AA} is plotted as a function of the multiplicity, this behavior is supported, as presented in figure 5.3. The matched values hereby are together with the Pb-Pb collision in standard binning on the same curve. The curve formed by the Xe-Xe collisions and the Pb-Pb collision curve converge for higher multiplicity and are indistinguishable for $\frac{dN_{ch}}{d\eta} > 500$. This underlines the statement made above about them being in agreement for $\frac{dN_{ch}}{d\eta} > 489$.
The ratio of the two R_{AA} are shown in figure 5.4. It is visible that the R_{AA} is in agreement with each other for low $p_T < 1\ GeV/c$, therefore the energy loss in both systems is equal within uncertainties. However at central at high p_T the energy loss for Xe-Xe collisions seem to be lower than for Pb-Pb collisions at same multiplicity. In the p_T region of 2-4 GeV/c a small bump with an deviation from unity of up to

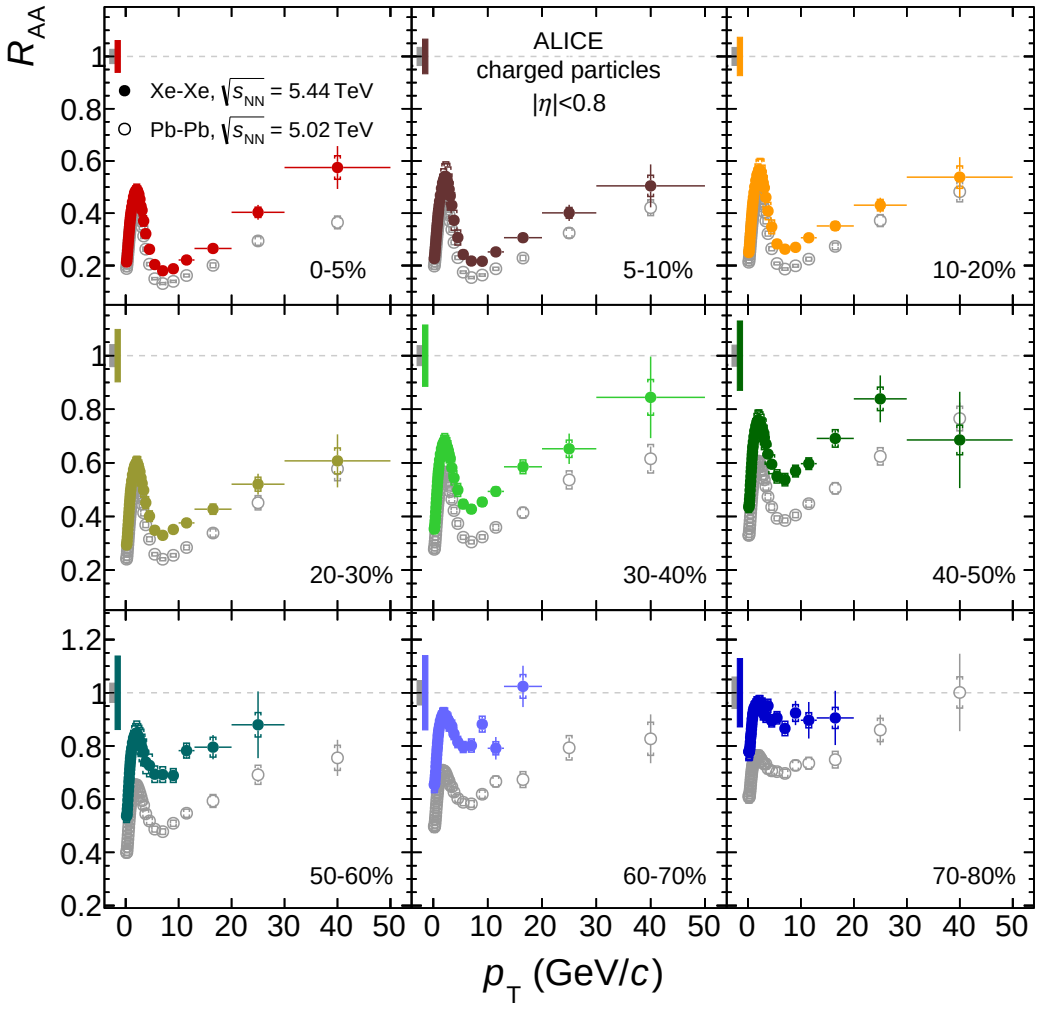

Figure 5.1: Published results of R_{AA} comparisons of Xe-Xe and Pb-Pb collision in matched centrality bins [42].

10% can be seen especially for a matched multiplicity of about 963 and 724. This bump may be due to different transverse radial flow or due to the different initial geometry of the Pb ion being spherical and the Xe ion being deformed. It is also visible that the ratio diverges for higher centrality or lower multiplicity.

5.1.1 Impact of the T_{AA} values

For further investigation the T_{AA} value presented in formula 5.1 is removed from the equation, which should lead to a better matching at peripheral collisions. This

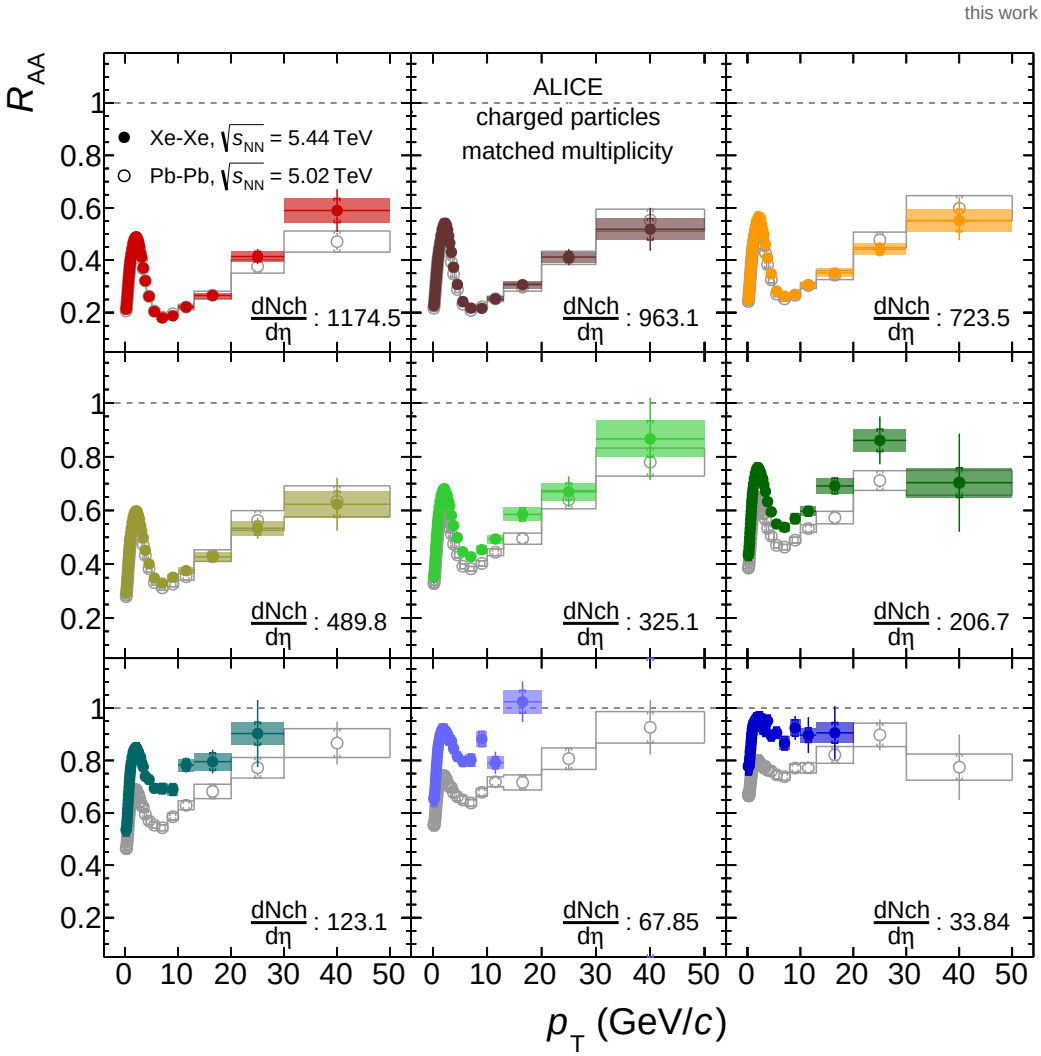

Figure 5.2: R_{AA} comparisons of Xe-Xe and Pb-Pb collision in matched multiplicity bins.

leaves as ratio

$$R^{*}_{AA} = \frac{dN_{AA}(p_T)/dp_T}{d\sigma_{pp}(p_T)/dp_T}. \tag{5.2}$$

The corresponding ratio between Xe-Xe and Pb-Pb collisions is shown in figure 5.5. Now the matching is in agreement over the complete multiplicity range and especially in the low p_T region. This means that for the bulk production in heavy-ion collisions the difference only comes from the T_{AA} values. However, the bump around 2 - 4 GeV/c did not vanish, but this is expected since the T_{AA} is only centrality dependent and not p_T-dependent.
For this representation, the R_{AA} of Xe-Xe and Pb-Pb collisions are nearly identical

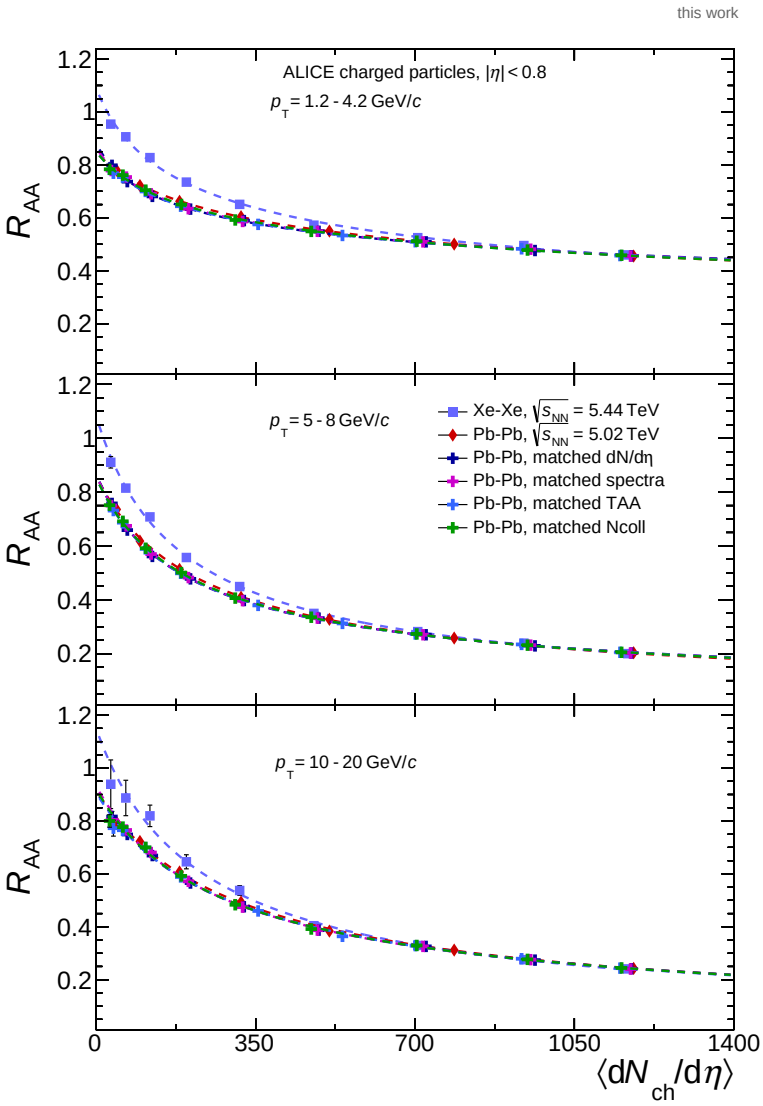

Figure 5.3: Nuclear modification factor as function of the multiplicity for Pb-Pb and Xe-Xe collisions. All matched centrality ranges are shown. The Xe-Xe curve is distinctive for low multiplicities but converges to the Pb-Pb curve for higher multiplicities $\frac{dN_{ch}}{d\eta} > 400$. The p_T regions are chosen such that the maximum and minimum of the R_{AA} is considered as well as the high p_T region.

as a function of multiplicity as shown in figure 5.6. It can also be seen that now the Xe-Xe and Pb-Pb data are on the same curve. For the low p_T regime it can be described by a linear function while for mid and high p_T a second order polynomial is required. For the mid and high p_T regime the explanation is jet quenching which scales with system size and therefore with multiplicity. The quenching suppresses

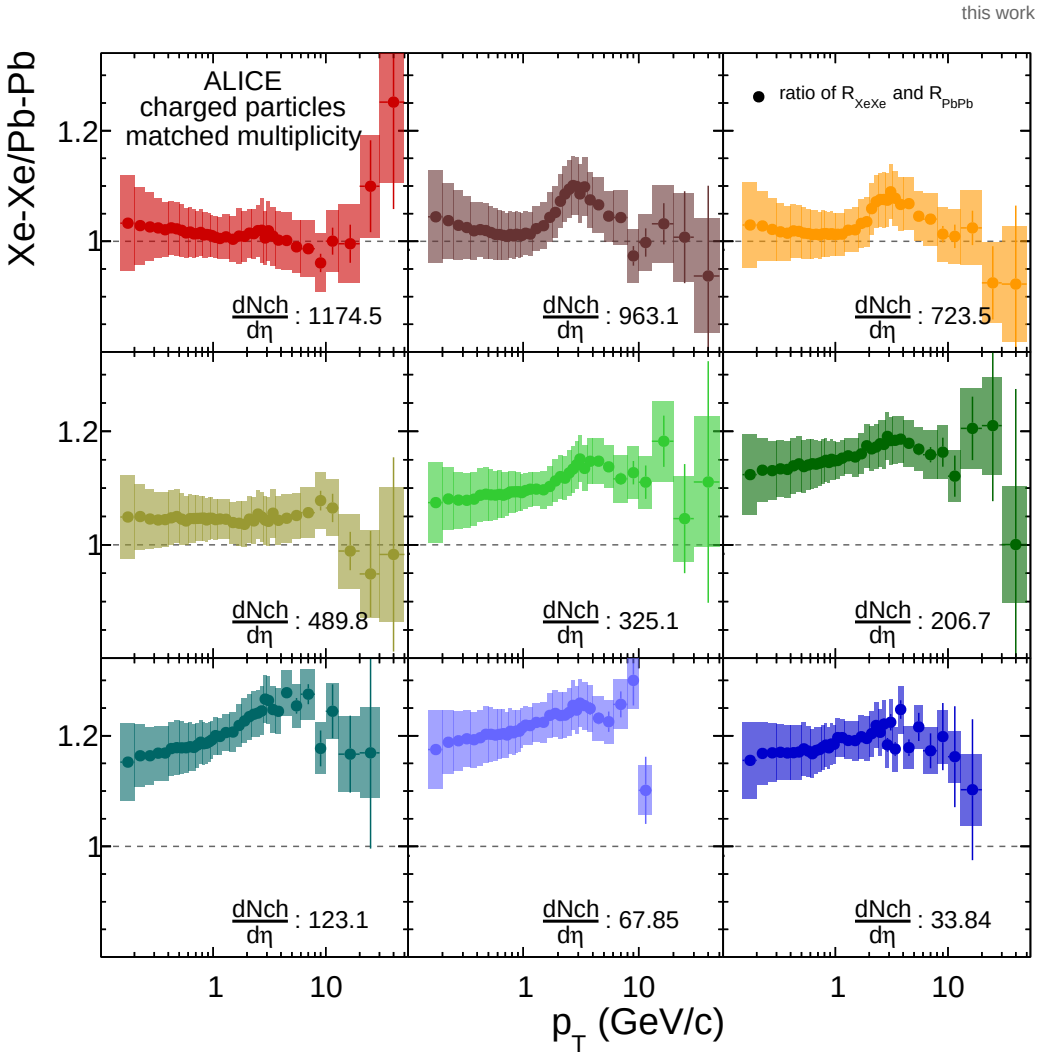

Figure 5.4: Ratio of the R_{AA} for matched multiplicity in each centrality bin.

the high momentum part at high multiplicities.

5.1.2 Impact of the pp reference

For further analysis on the ratio, also the pp reference is removed from the calculation leaving just the comparison of the spectra

$$dN_{AA}(p_T)/dp_T.$$

In principle this should enhance the difference since the two collision systems have different energies which the pp reference takes into account. However in reality it gives an even better match in the low p_T regime, with higher divergence in the high

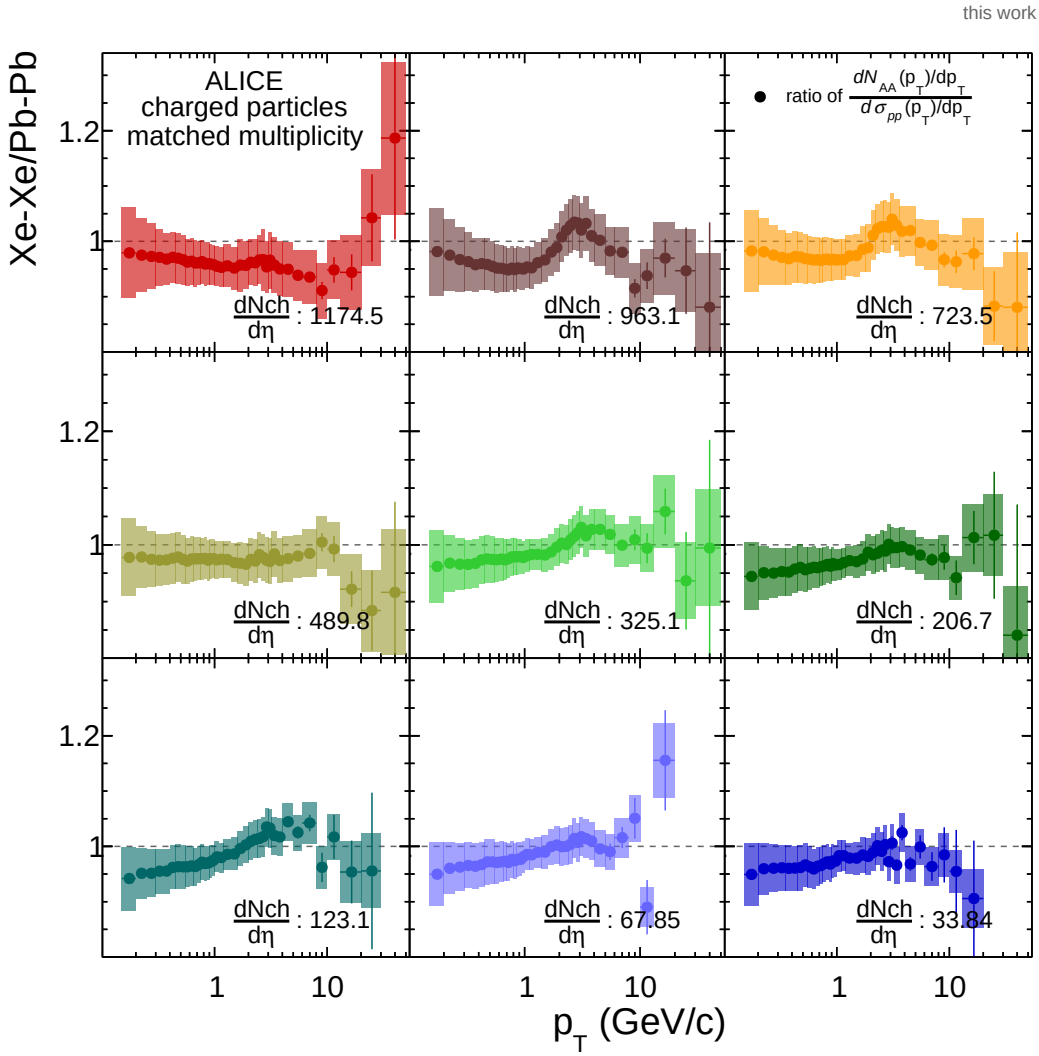

Figure 5.5: Ratio of R^*_{AA} for Pb-Pb and Xe-Xe collisions at matched multiplicity.

p_T regime. The bump at 2 - 4 GeV/c gets also enhanced. In figure 5.7 the ratio between the matched spectra in Pb-Pb and the Xe-Xe collisions are shown.

5.1.3 Impact of the particle composition correction

Since the particle composition correction plays a role in the p_T range where the bump is observed, the correction was further studied. The particle composition correction is explained in detail in section 4.3.2. To show the impact of the particle composition correction the ratio of the spectra in Pb-Pb to Xe-Xe collisions is shown for matched multiplicity in figure 5.8. Leaving out the particle composition correction does not decrease the bump but rather increases it for all multiplicity ranges. As explained in section 4.3.2 the particle composition correction for Xe-Xe collisions is

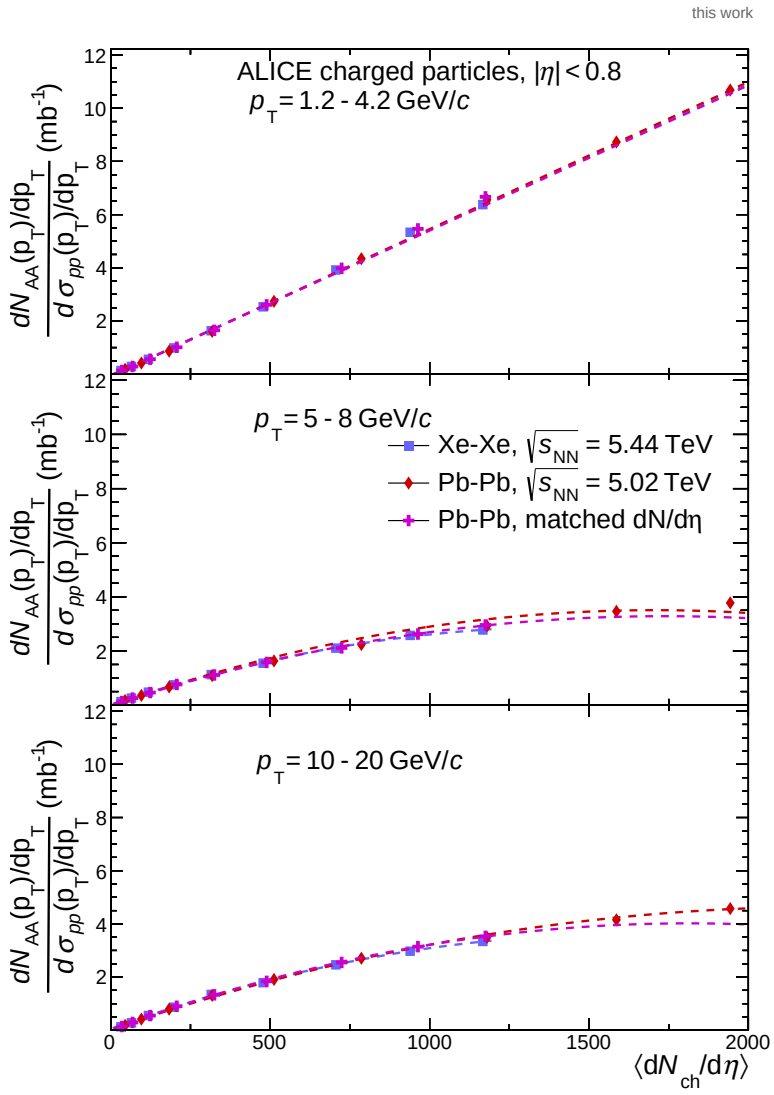

Figure 5.6: R^{*}_{AA} as function of the multiplicity for Pb-Pb and Xe-Xe collisions including matched multiplicity Pb-Pb collisions. The p_T regions are chosen such that the maximum and minimum of the R_{AA} is considered as well as the high p_T region.

based on the data for Pb-Pb collisions for the same multiplicity. In principle, when matching the multiplicity the correction should drop out. However this is not the case. In figure 5.8 it is visible that without particle composition correction the bump gets enhanced rather than suppressed or vanished. This leaves to speculate that a separate correction for the Xe-Xe values, which is not dependent on Pb-Pb results, could further clarify the origin of the bump.

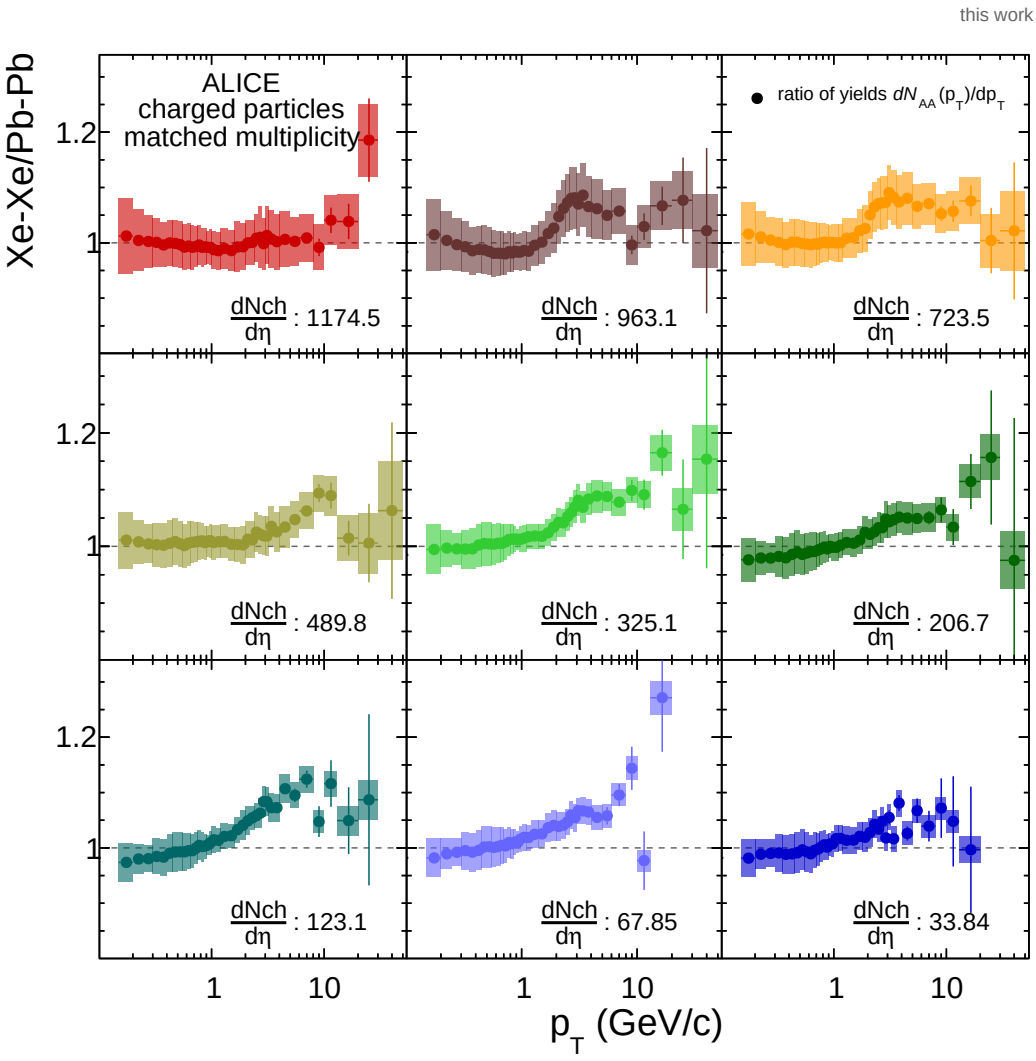

Figure 5.7: Ratio of the p_{T} spectra of Xe-Xe and Pb-Pb collisions at different matched multiplicities.

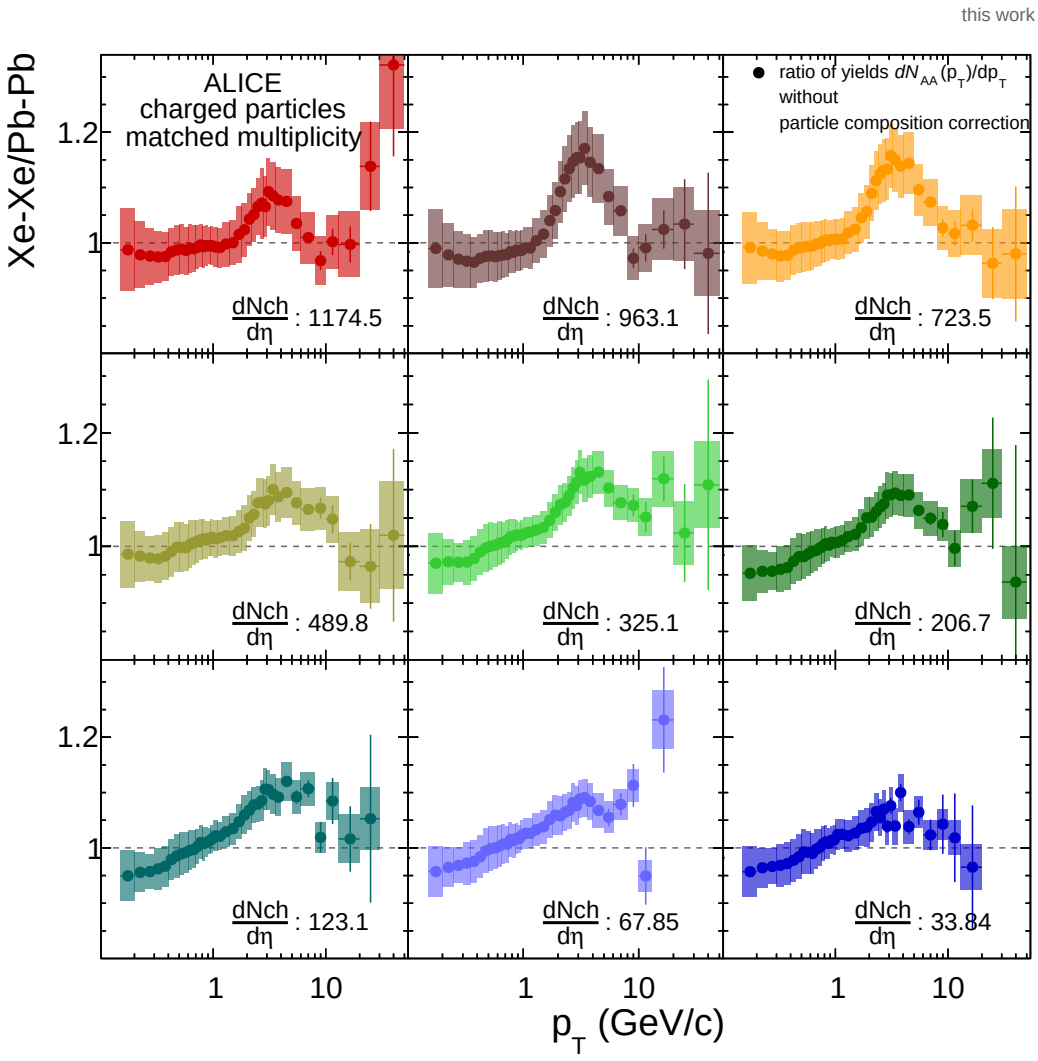

Figure 5.8: Comparison of the p_{T} spectra of Xe-Xe and Pb-Pb collisions at different matched multiplicities without particle composition correction.

5.2 Comparison to CMS

CMS has also measured Xe-Xe collisions at $\sqrt{s_{\mathrm{NN}}} = 5.44$ TeV in 2017 [49] with 19 million MB events. The data obtained in this thesis is therefore now compared to the CMS values. At first the systematic uncertainties are compared. Compared to the values obtained in this thesis the systematic uncertainties are large. The full systematic uncertainties of this thesis can be viewed in the appendix figure A.1. There it is visible, that the uncertainties never reaches over 5%, which is significantly better than the CMS uncertainties, which are larger then 5% throughout and reach heights of over 17%. Also their normalization uncertainty is significantly larger than the one obtained in this thesis with a normalization of up to 26% for most peripheral collisions.
CMS also measured the $\mathrm{R_{AA}}$ of Xe-Xe collisions in 6 centrality regions. For this CMS used an extrapolated pp reference spectrum which was extrapolated using a MC driven approach. Here the ratio of a MC sample generated by PYTHIA at 5.02 Tev and 5.44 TeV was used to scale the measured pp reference spectrum to the desired center of mass energy of 5.44 TeV. The $\mathrm{R_{AA}}$ acquired in this thesis at the ALICE experiment is compared to the ones published by CMS in figure 5.9.
Here matching between the $\mathrm{R_{AA}}$ from ALICE and CMS can be seen for high centrality but a divergence fore peripheral collisions can still be seen. The data points however are within margin of error to each other due to the large uncertainties from the CMS data points for central to mid-central collisions. For peripheral collisions the CMS data seems to get flatter then the corresponding ALICE data. It also shows a greater energy loss then the ALICE data for these centrality bins. Their data however corresponds better to their Pb-Pb data. It has to be noted however that the data taking in CMS goes up to 100 GeV/c in p_{T} which is larger then the 50 GeV/c limit of ALICE. Also are the high p_{T} bins of ALICE in dominated with systematical uncertainties.

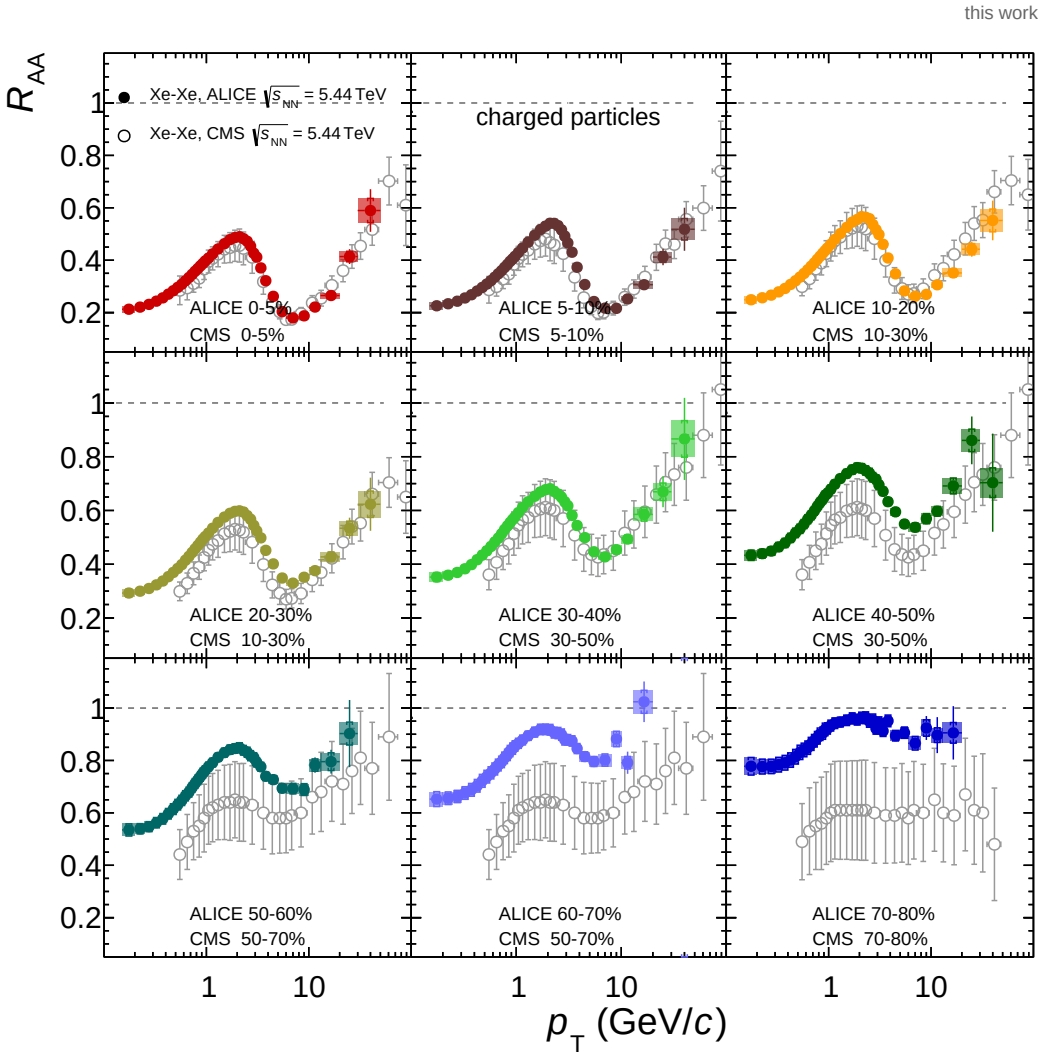

Figure 5.9: R_{AA} comparison from ALICE to CMS data in 9 centrality bins. The centrality bins from CMS are wider than the ones from ALICE. The uncertainty of the CMS data points is the combined uncertainty of statistical, systematical and normalization uncertainties. CMS data taken from [49].

5.3 Comparison to model calculations

Various models which describe the energy loss in the QGP exist. However neither models can describe all aspects of particle production over the entire p_T range and rather try to describe certain aspects (e.g. hydrodynamics, jet quenching etc.) with greater precision. This explains the variety of models. In this thesis, comparison to the model from Djordjevic [50, 51, 52, 53], the CUJET [54, 55] model and a linear Boltzmann transport (LBT) [56, 57] model are made. These models are base

on the factorization theorem in **p**erturbative **Q**uantum **C**hromo **D**ynamics (pQCD) calculations. The energy loss of fast partons is encoded in the fragmentation function that is modified due to the presence of a medium.
The Djordjevic model describes energy loss through pQCD for high p_{T} particles ($p_{\mathrm{T}} > 10$ GeV/c). For this purpose, it takes into account a finite size medium a finite temperature field theory and a generalized HTL (Hard Thermal Loop) approach. It uses a state-of-the-art dynamical energy loss formalism, with a medium that undergoes Bjorken expansion [58] or expands with a constant temperature. Radiative and collisional energy losses of light and heavy flavor hadrons are taken into account. The path length dependence is predicted between linear and quadratic.
The CUJET model is split into two components, a jet quenching model that includes the suppression of quark and gluon degrees of freedom and the emergence of magnetic monopoles and a framework calculating the dependence of correlations between soft and hard azimuthal flow on an event-by-event basis. It uses a semi-Quark-Gluon-Monopole-Plasma model for studies on the confinement in the vicinity of the critical temperature T_c. The CUJET model also takes a perturbative HTL approach.
The LBT model is combining the kinetic description of a parton propagating the QGP with the hydrodynamic description of the evolution of the medium. The LBT uses pQCD calculations for elastic and inelastic collisions inside the medium where it incorporates the energy of the jet, the medium temperature and flow dependencies of jet-medium interactions. It can also be used for jet transport in the medium and and jet-induced medium excitations. It predicts a quadratic path length dependence in case of a static medium.
The results of the models are compared to the experimental results in figure 5.10. The models describe the data only in the high p_{T} region and only in central collisions adequately. In semi-central and more peripheral collisions the models are below the data points, this translates to a disagreement in the centrality dependence between the models and the data. This behavior can also be seen in figure 5.11 where the $\mathrm{R_{AA}}$ is plotted as function of the multiplicity. There one can see that the Djordjevic model does not match peripheral collisions well and is only suitable for central collisions. This is probably due to a wrong scaling with multiplicity for this model. It assigns a higher energy loss than is measured in data. Therefore the models can describe central high p_{T} collisions rather well but do not describe the data at all for peripheral collisions. In the mid p_{T} range of 5 - 8 GeV/c data and models diverge except in central Pb-Pb collisions. In the high p_{T} range of 10 - 20 GeV/c data and model are more in agreement to each other for multiplicities larger than 500. The models however scale differently with the multiplicity in this region being lower than data in the low multiplicity range and being higher than data in the high multiplicity range.
To test for path length dependence in the QGP, Djordjevic et al. suggested a new variable to be taken into account, that is supposedly more sensitive to the path length dependence than the simple ratio of nuclear modification factors. It was derived from simple scaling arguments and assuming a similar temperature in both collision systems.. This variable should take two different heavy-ion colliding systems

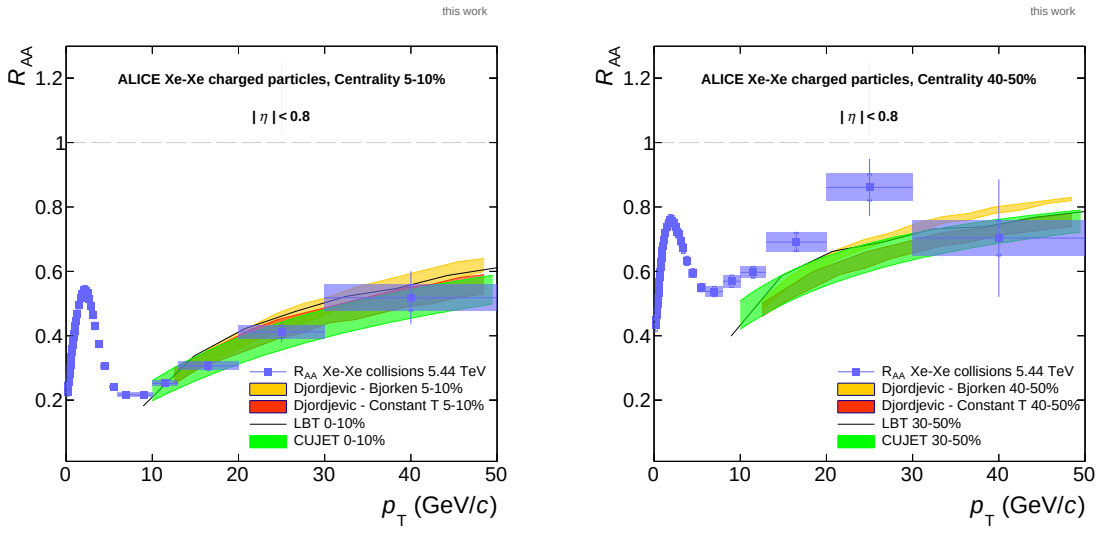

(a) (b)

Figure 5.10: Comparison of the R_{AA} of Xe-Xe to the theoretical model calculations of Djordjevic, LBT and CUJET are shown. All comparisons are found in the appendix A.6.

into account.

$$R_L^{XePb} = \frac{1 - R_{XeXe}}{1 - R_{PbPb}} \approx \left(\frac{A_{Xe}}{A_{Pb}}\right)^{b/3} . \tag{5.3}$$

This formula is a simple expression and depends only on the medium size (mass number of the nuclei A_{Xe}/A_{Pb}) and the path length dependence (with b being the exponent of the path length L). This simplification of the complex problem of path length dependence should hold true for central collisions and high p_T regions. Inserting the numbers for a linear (b = 1) or quadratic (b = 2) path length gives values for R_L^{XePb} of ≈ 0.85 and ≈ 0.73 respectively. Since the model from Djordjevic is available for Xe-Xe and Pb-Pb collisions, its R_L^{XePb} is compared to the data in same centrality and matched multiplicity.
As shown in figure 5.12, the model does describe the data points accurately for central collisions. It can also be seen that for central collisions the match between data and model is within uncertainties and predicting an almost linear path length dependence in central collisions. As shown in the appendix A.8, the linear path length dependence is matched up to a centrality of 20-30%. Afterwards, model and data diverge drastically and do not match anymore. It has to be noted however, that the model does not take into account the different center of mass energies in Pb-Pb and Xe-Xe collision of $\sqrt{s_{NN}} = 5.02$ TeV and $\sqrt{s_{NN}} = 5.44$ TeV respectively. Even though the difference is only $\approx 10\%$, it has to be noted that the energy loss has a cubic dependence on the temperature ($\sim T^3$).

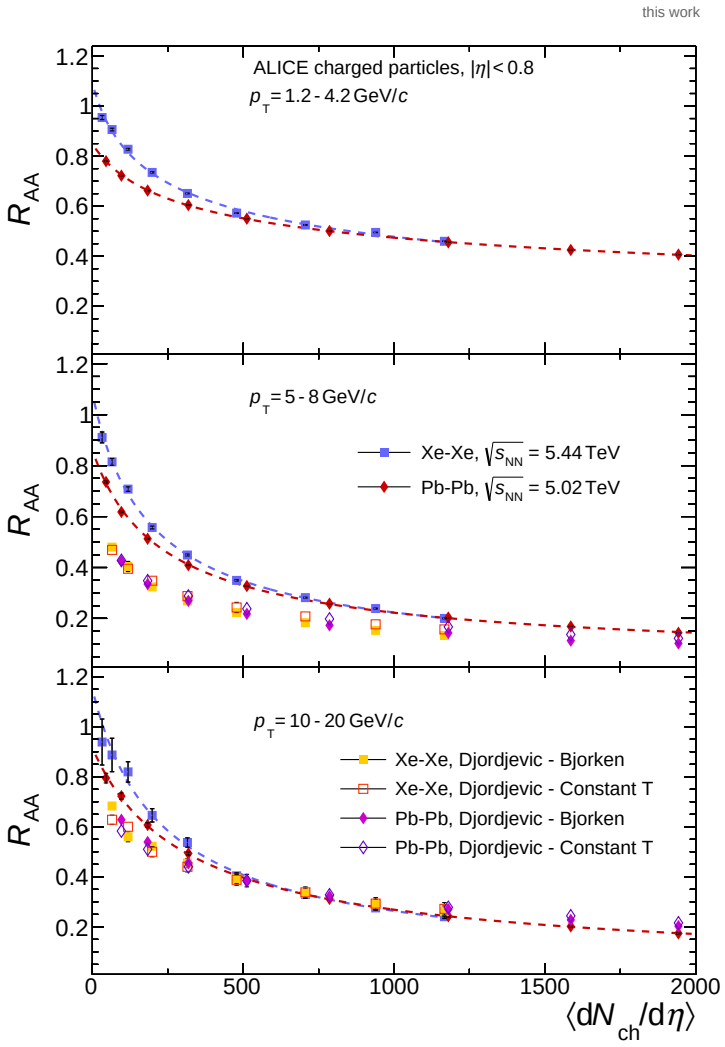

Figure 5.11: R_{AA} as a function of multiplicity for Pb-Pb and Xe-Xe collisions and corresponding models calculations from Djordjevic et al. are shown. It is visible that the model best describes data with higher transverse momentum and higher multiplicity.

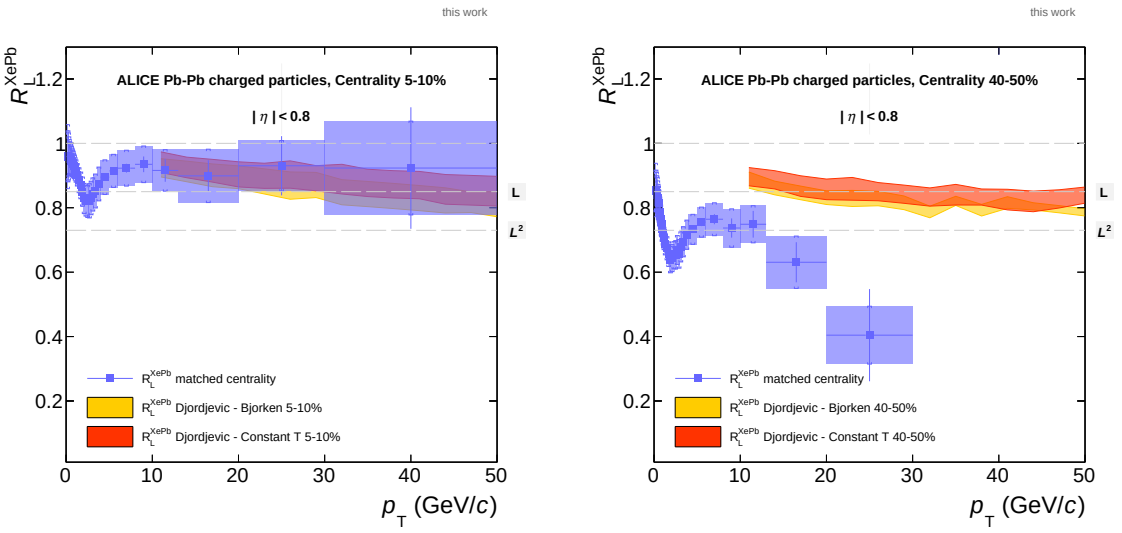

Figure 5.12: Comparison of the R_L^{XePb} in same centrality intervals for Pb-Pb and Xe-Xe collisions to the model calculations of Djordjevic et al.. It can be seen that the model describes the data best for central collisions. Comparisons for all centralities can be found in the Appendix A.8.

6 Conclusion and outlook

In this thesis, heavy-ion collisions measured by the ALICE detector at the LHC were analyzed for Xe-Xe and Pb-Pb collisions at $\sqrt{s_{\mathrm{NN}}} = 5.44$ TeV and $\sqrt{s_{\mathrm{NN}}} = 5.02$ TeV respectively. The transverse momentum distribution for charged particles was measured at a pseudorapidity of $|\eta| < 0.8$ and transverse momentum range of $0.15 < p_T < 50$ GeV/c for nine centrality classes. The centrality classes in Pb-Pb collisions were furthermore matched in multiplicity to those in Xe-Xe collisions. The transverse momentum distributions were efficiency and acceptance corrected using Monte Carlo data samples. They were also corrected for their particle composition and their transverse momentum resolution. The systematic uncertainties were determined using variations of the selection criteria as well as contributions coming from the corrections and the material budget. The systematic uncertainties dominate over the statistical uncertainties for $p_{\mathrm{T}} < 20$ GeV/c, than the statistical uncertainties dominate. The uncertainties are below 10% for Pb-Pb collisions and below 5% for Xe-Xe collisions. This data is the most precise data at the LHC so far for charged hadron $\mathrm{R_{AA}}$ in these collision systems.

An analysis of the nuclear modification factor $\mathrm{R_{AA}}$ with a comparison between the two different colliding systems at matched multiplicity was provided. The two $\mathrm{R_{AA}}$ were in excellent agreement for a multiplicity $\frac{d\mathrm{N_{ch}}}{d\eta}$ of over 400. In the ratio of the two $\mathrm{R_{AA}}$ in central collisions, a deviation at $2 < p_T < 4$ GeV/c not larger than 10% was observed. It might be attributed to the slightly different energies of the two colliding systems which are also approximately 10% apart or the different overlap of the nuclei due to the deformation of the xenon ion.

Comparing the $\mathrm{R_{AA}}$ obtained for Xe-Xe collisions to the $\mathrm{R_{AA}}$ obtained by the CMS experiment at the same energies showed good agreement for central collisions. The data however diverges for semi-central collisions with the ALICE results. This divergence increases towards more peripheral collisions. Interestingly, while the ALICE $\mathrm{R_{AA}}$ values approach unity, the CMS data seems to stay constant.

The obtained results were then compared to model calculations which describe the energy loss in the QGP through theoretical calculations for high p_{T} particles. In the comparison of the $\mathrm{R_{AA}}$ the models describe central collisions well in the high transverse momentum region ($p_{\mathrm{T}} > 10$ GeV/c) whereas peripheral and low transverse momentum regions ($p_{\mathrm{T}} < 10$ GeV/c) were not matched between data and model. A second variable the $\mathrm{R_{L}^{XePb}}$ was introduced which can compare two different colliding systems and could hint to a path length dependence regarding this value. This variable shows when applied to data a linear path length dependence in central to mid-central collisions. This contradicts the L^2 dependence from simple arguments made in [42]. However the same as for the $\mathrm{R_{AA}}$ can be said, with the model describing

the high transverse momentum region ($p_{\mathrm{T}} > 10$ GeV/c) well and the peripheral and low transverse momentum regions ($p_{\mathrm{T}} < 10$ GeV/c) badly. This variable also does not take into account the slightly different collision energies of the two colliding systems and comparing them for matched multiplicity data of Xe-Xe and Pb-Pb collisions shows no match at all.
For further analysis on the nuclear modification factor in different heavy-ion collisions a run with ^{16}O is considered after LS2 (long shutdown 2 of the LHC). This could lead to further insight on the path length dependence and the scaling of the QGP properties with system size. Further analysis on this specific data should use a new particle composition correction based on Xe-Xe data and their particle abundances as well as an experimentally obtained pp reference. These would minimize cross correlations between the two colliding systems. In 2018, a large data set of $\sim$ 100 million central Pb-Pb collisions was recorded at ALICE. This enables ALICE to measure $\mathrm{R_{AA}}$ up to 100 GeV with good statistical and systematic precision.

A Appendix

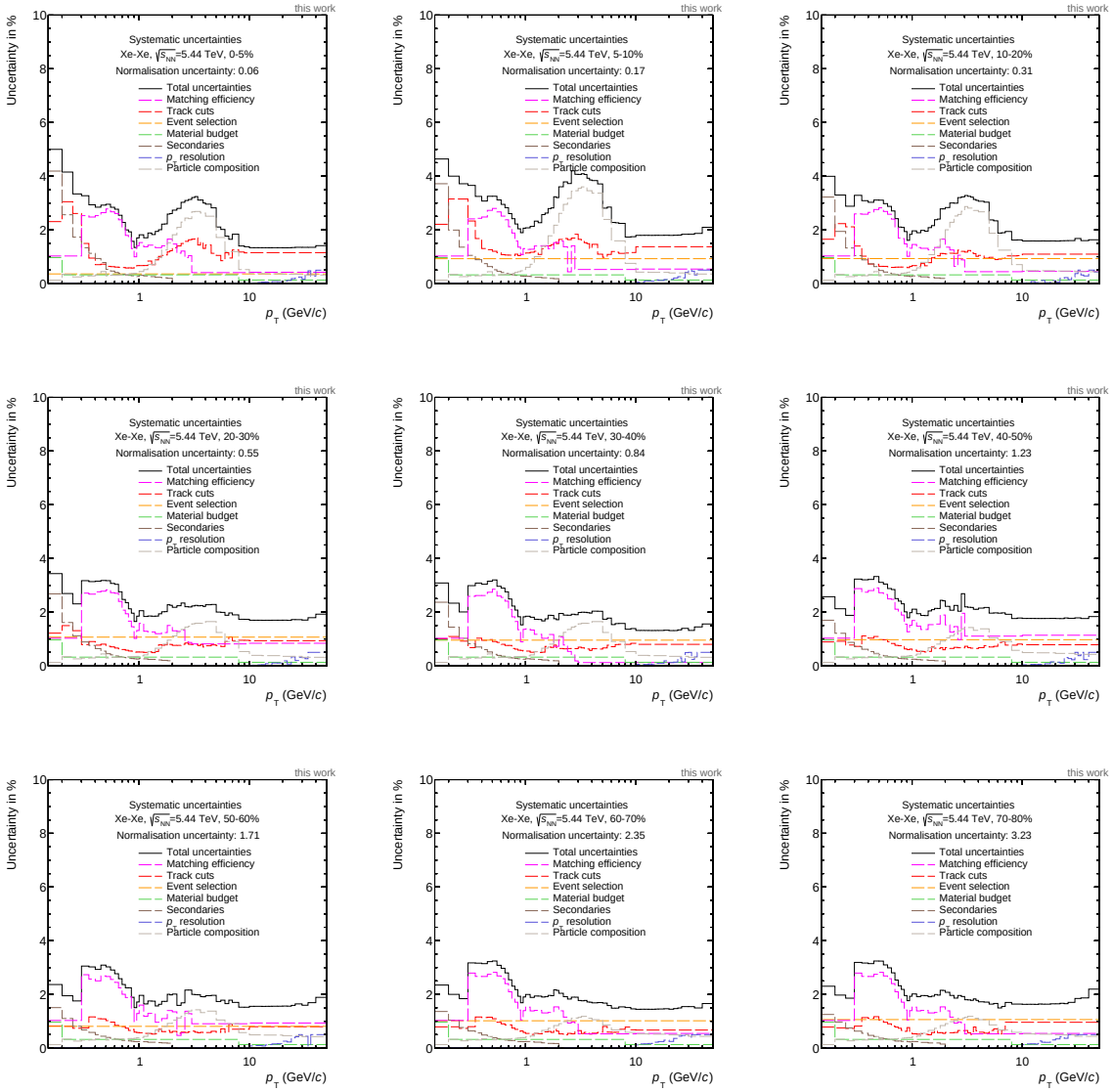

Figure A.1: Systematic uncertainties for Xe-Xe collisions for all centrality classes.

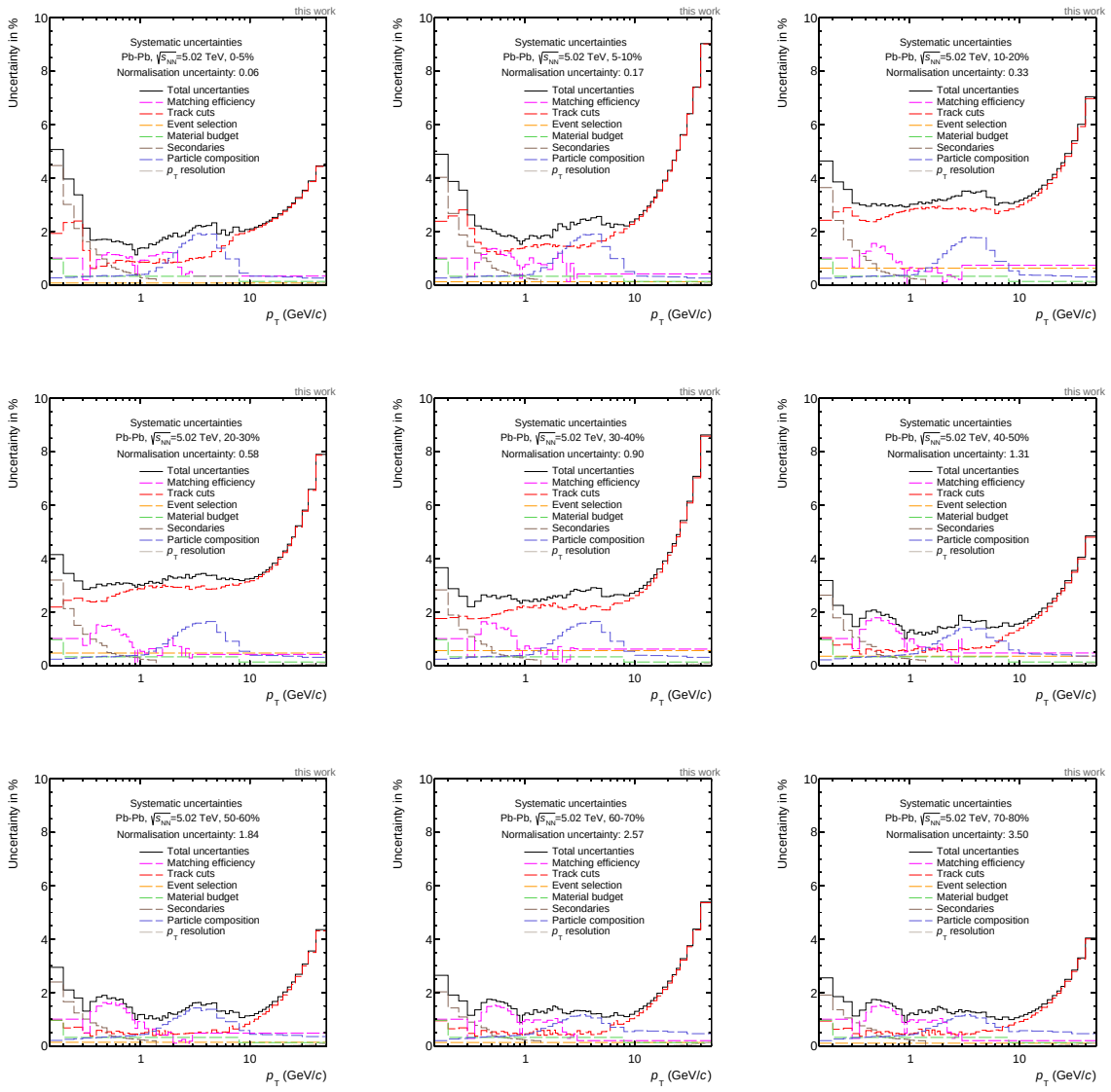

Figure A.2: Systematic uncertainties for Pb-Pb collisions for all centrality classes.

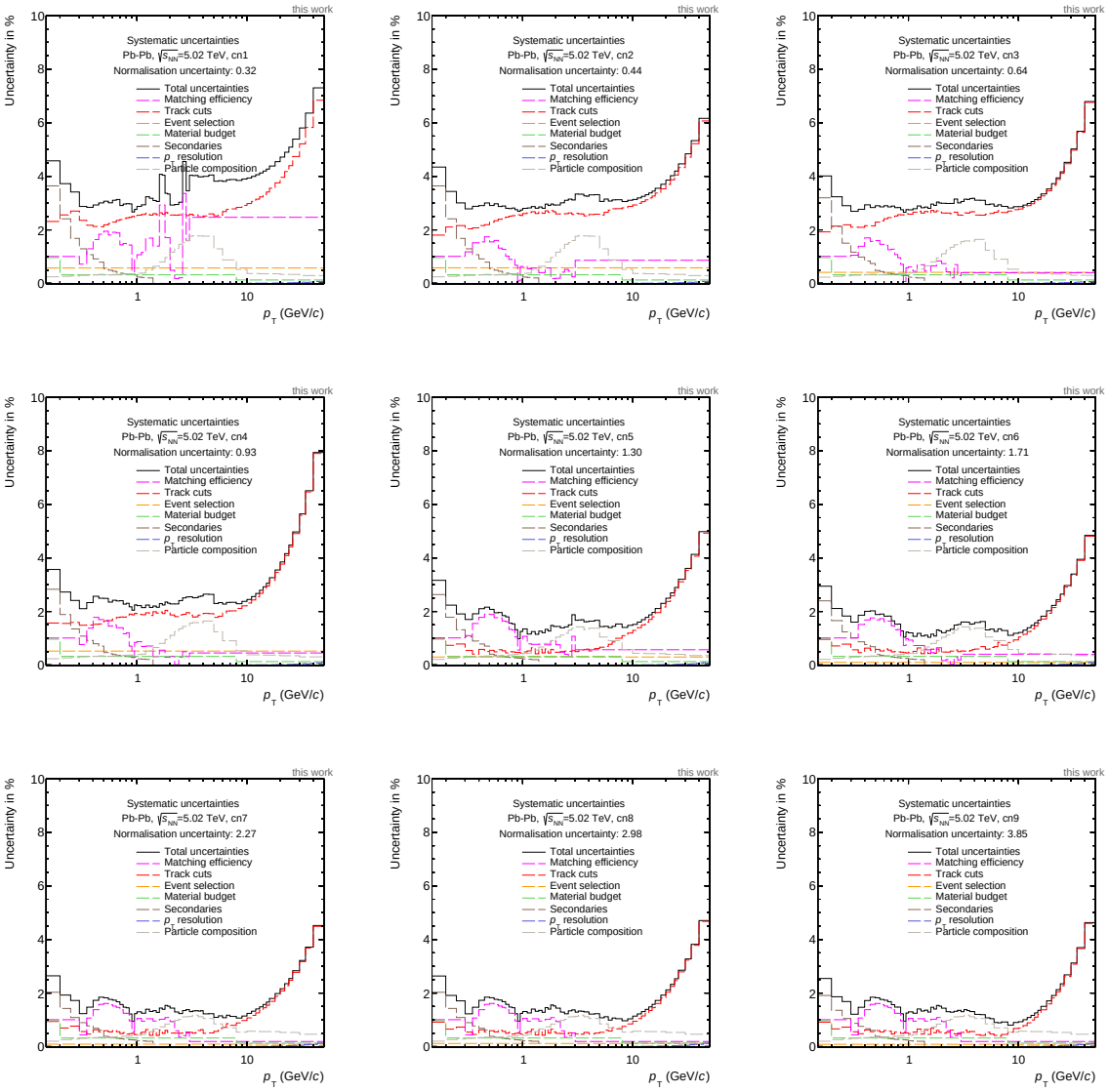

Figure A.3: Systematic uncertainties for Pb-Pb collisions for matched centrality classes.

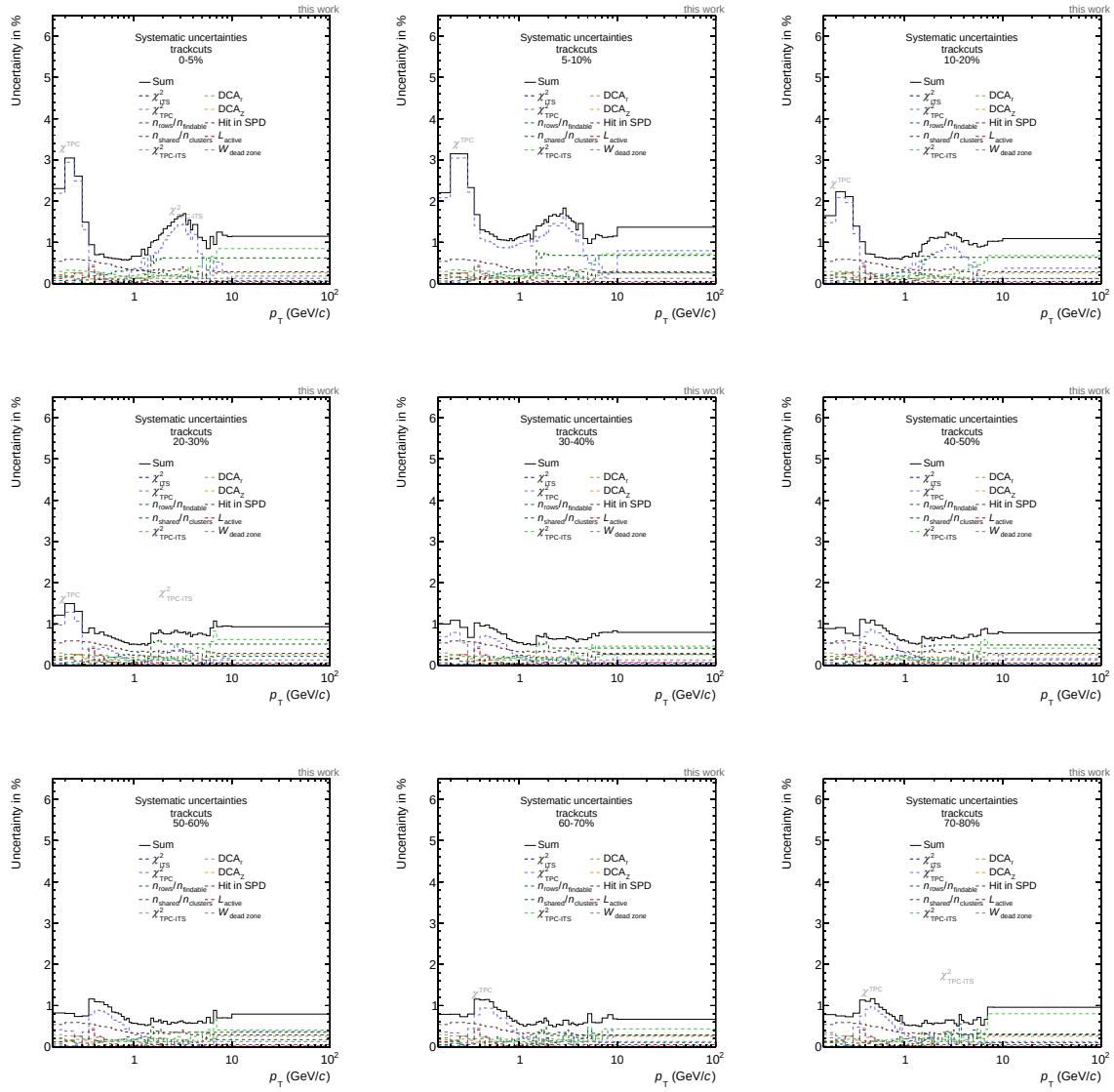

Figure A.4: Systematic uncertainties for track selection in Xe-Xe collisions for all centrality classes.

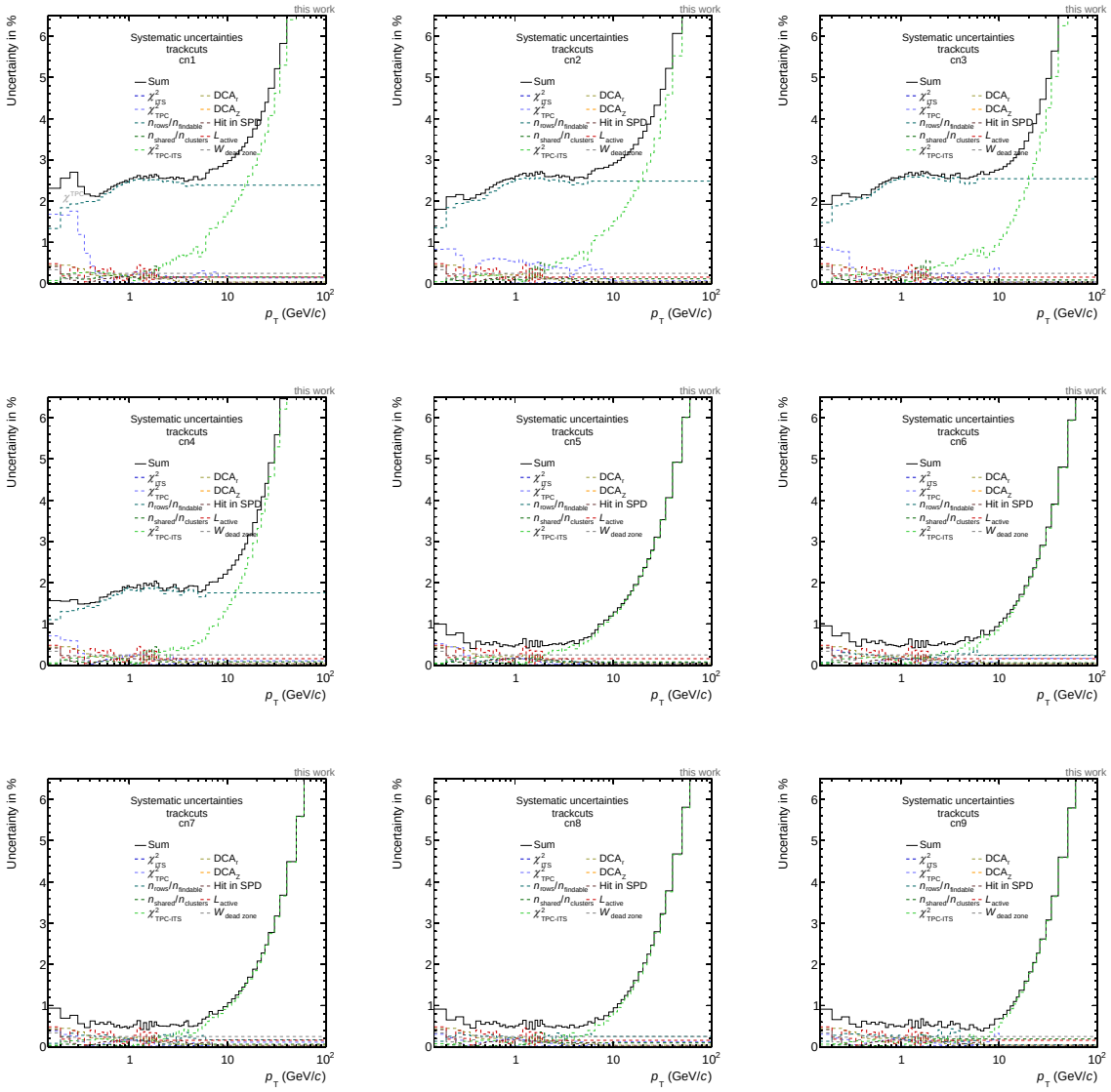

Figure A.5: Systematic uncertainties for the track selection in Pb-Pb collisions for matched centrality classes.

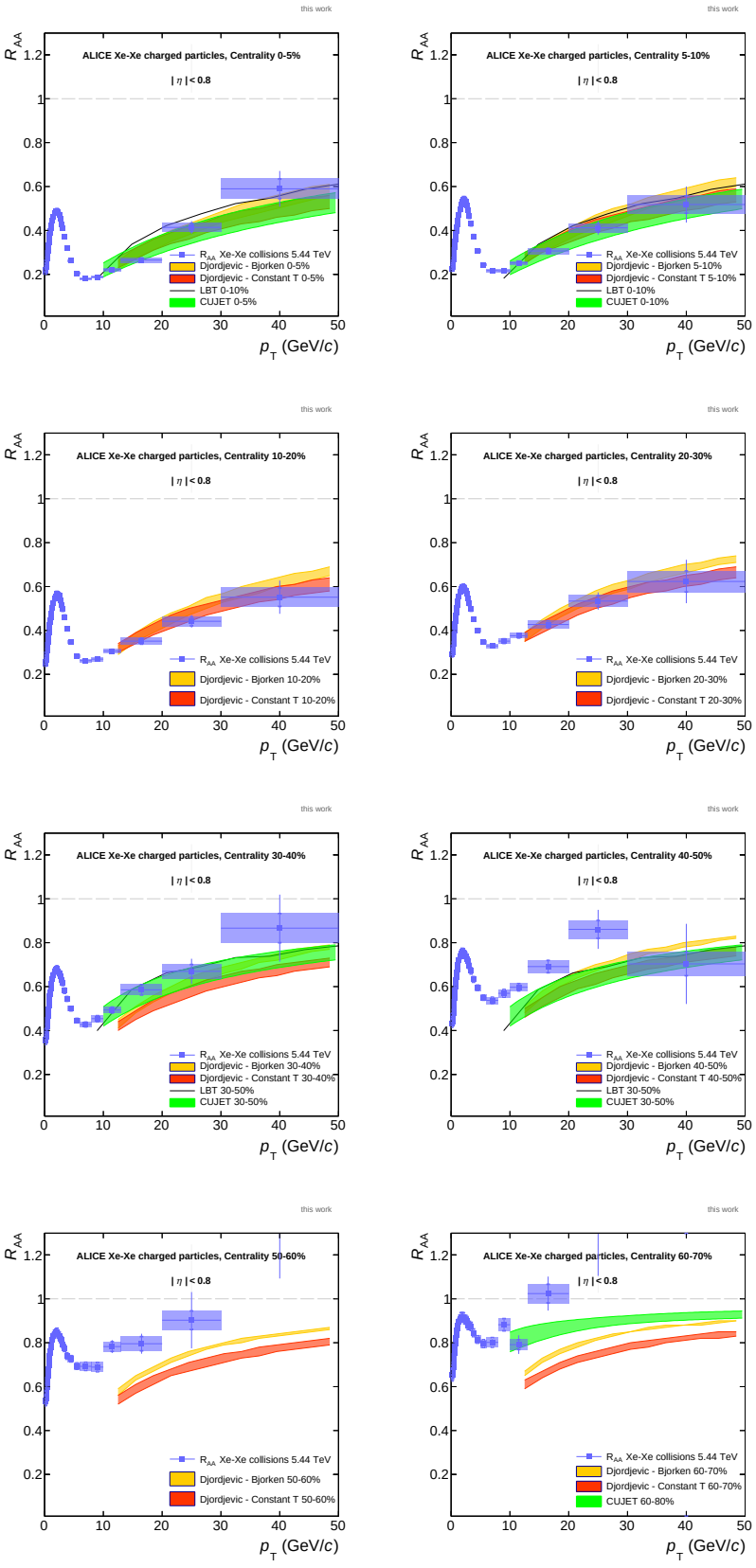

Figure A.6: Comparison of R_{AA} between the Djordjevic model and experimental data in Xe-Xe collisions.

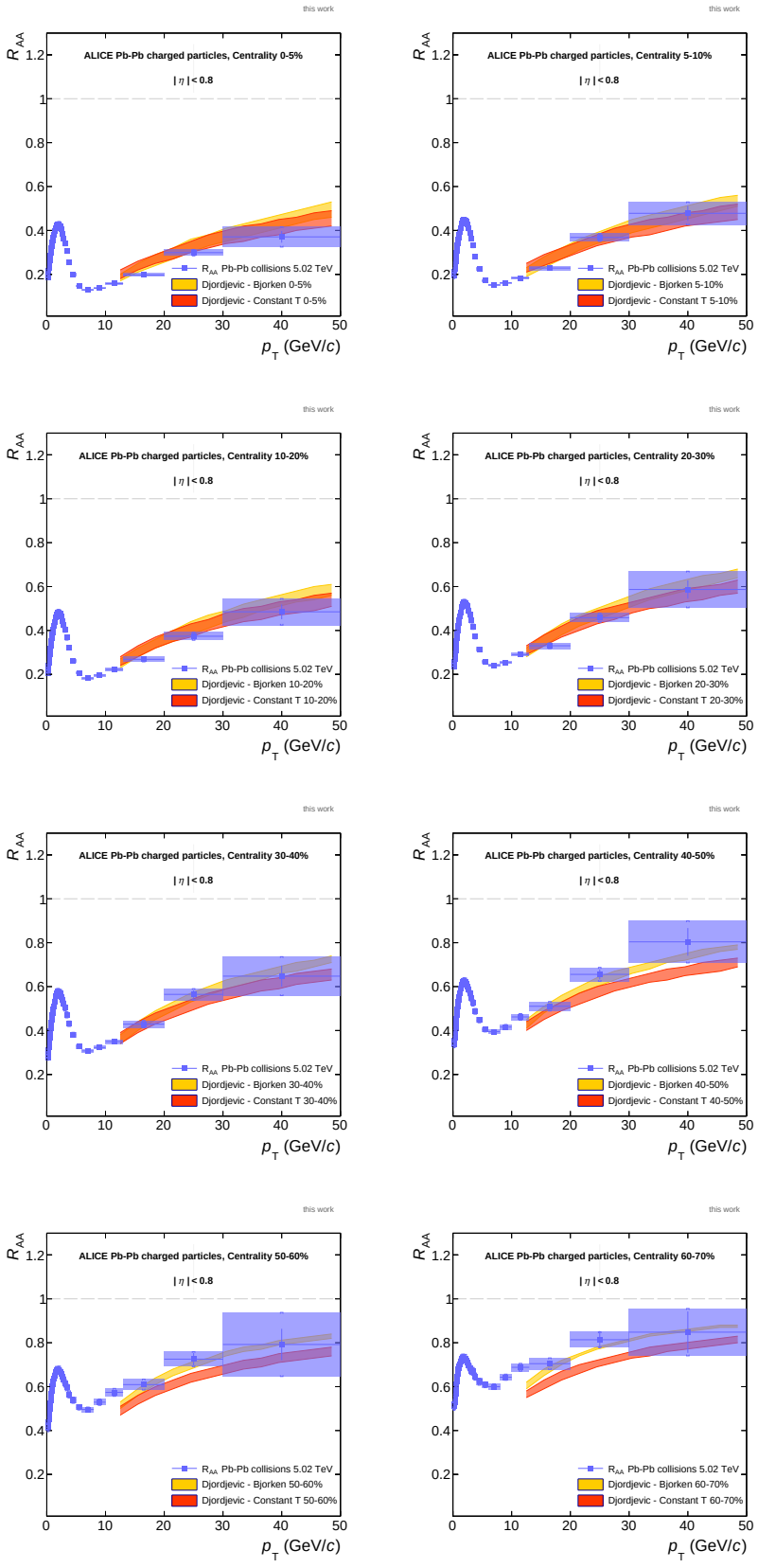

Figure A.7: Comparison of R_{AA} between the Djordjevic model and experimental data in Pb-Pb collisions.

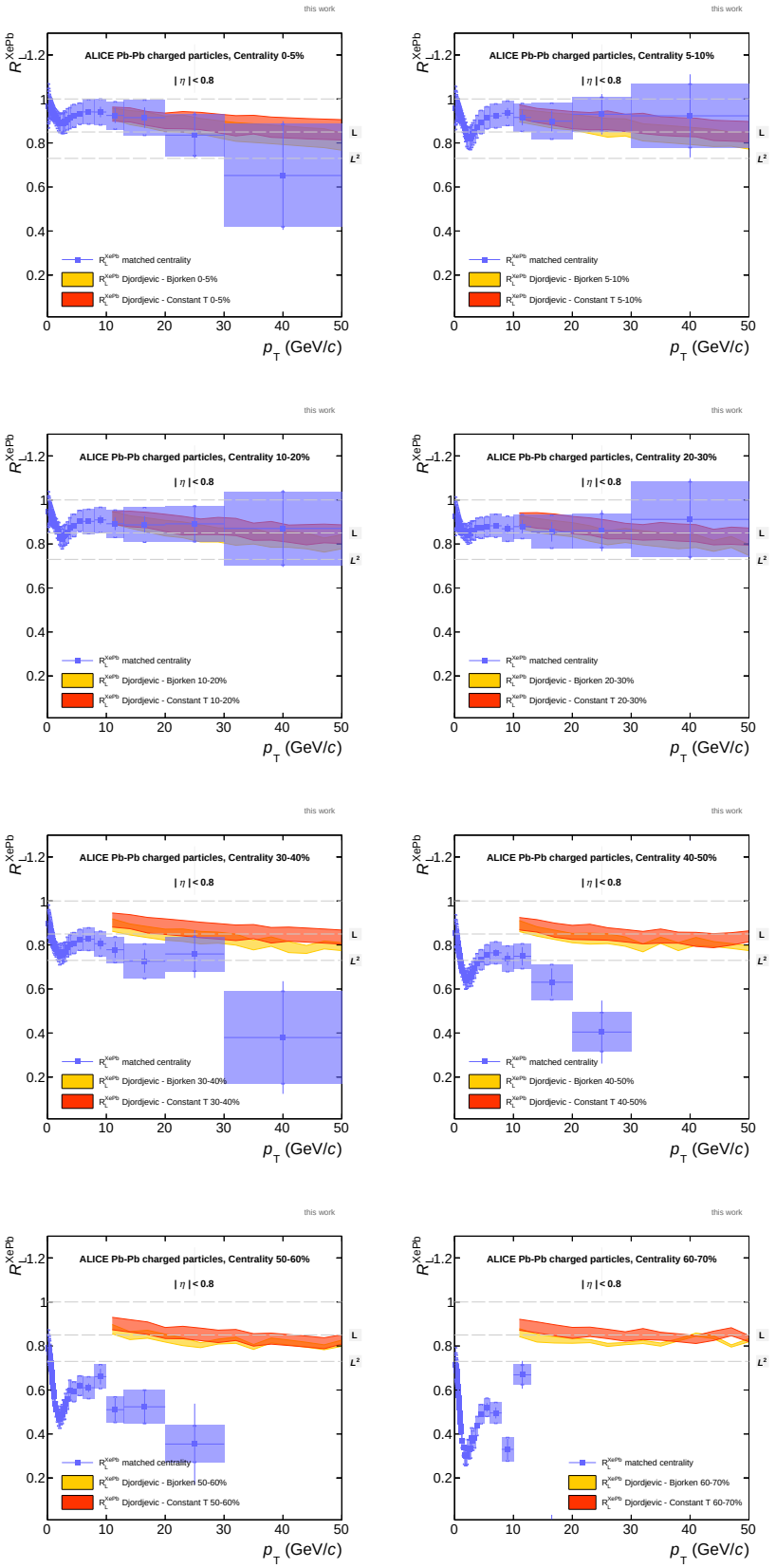

Figure A.8: Comparison of R_L^{XePb} between the Djordjevic model and experimental data in Xe-Xe and Pb-Pb collisions at the same centrality.

B Bibliography

[1] Murray Gell-Mann. *Progress in elementary particle theory, 1950–1964*. WORLD SCIENTIFIC, Feb. 2010, pp. 360–377. DOI: 10.1142/9789812836854_0024. URL: https://doi.org/10.1142/9789812836854_0024.

[2] Martin L. Perl, Eric R. Lee, and Dinesh Loomba. "Searches for fractionally charged particles". In: *Ann. Rev. Nucl. Part. Sci.* 59 (2009), pp. 47–65. DOI: 10.1146/annurev-nucl-121908-122035.

[3] S M Sanches, D A Fogaça, and F S Navarra. "The time evolution of the quark gluon plasma in the early Universe". In: *Journal of Physics: Conference Series* 630 (July 2015), p. 012028. DOI: 10.1088/1742-6596/630/1/012028. URL: https://doi.org/10.1088/1742-6596/630/1/012028.

[4] K. Aamodt et al. "Two-pion Bose-Einstein correlations in central Pb-Pb collisions at $\sqrt{s_{NN}} = 2.76$ TeV". In: *Physics Letters B* 696.4 (Feb. 2011), pp. 328–337. DOI: 10.1016/j.physletb.2010.12.053. URL: https://doi.org/10.1016/j.physletb.2010.12.053.

[5] Y. Aoki et al. "The order of the quantum chromodynamics transition predicted by the standard model of particle physics". In: *Nature* 443.7112 (2006), pp. 675–678. ISSN: 1476-4687. DOI: 10.1038/nature05120. URL: https://doi.org/10.1038/nature05120.

[6] D. d'Enterria and D. Peressounko. "Probing the QCD equation of state with thermal photons in nucleus–nucleus collisions at RHIC". In: *The European Physical Journal C* 46.2 (Mar. 2006), pp. 451–464. DOI: 10.1140/epjc/s2006-02504-0. URL: https://doi.org/10.1140/epjc/s2006-02504-0.

[7] Michael L. Miller et al. "Glauber Modeling in High-Energy Nuclear Collisions". In: *Annual Review of Nuclear and Particle Science* 57.1 (Nov. 2007), pp. 205–243. DOI: 10.1146/annurev.nucl.57.090506.123020. URL: https://doi.org/10.1146/annurev.nucl.57.090506.123020.

[8] Universität Zürich. *Standard Model of Particle Physics*. http://www.physik.uzh.ch/groups/serra/StandardModel.html. Visited on 02.05.2019. 2015.

[9] Guido Fantini et al. *The formalism of neutrino oscillations: an introduction*. 2018. arXiv: 1802.05781.

[10] Mark Thomson. *Modern Particle Physics*. Cambridge University Press, 2013.

[11] ALICE collaboration. "The ALICE definition of primary particles". In: (June 2017). URL: https://cds.cern.ch/record/2270008.

[12] M. Strickland. "Anisotropic Hydrodynamics: Three Lectures". In: *Acta Physica Polonica B* 45.12 (2014), p. 2355. DOI: 10.5506/aphyspolb.45.2355. URL: https://doi.org/10.5506/aphyspolb.45.2355.

[13] Edmond Iancu. "Multiparticle Dynamics in the LHC Era". In: *arXiv preprint arXiv:1105.0751* (2011).

[14] David d'Enterria. "6.4 Jet quenching". In: *Relativistic Heavy Ion Physics*. Springer Berlin Heidelberg, 2010, pp. 471–520. DOI: 10.1007/978-3-642-01539-7_16. URL: https://doi.org/10.1007/978-3-642-01539-7_16.

[15] N. Schwierz, I. Wiedenhover, and A. Volya. "Parameterization of the Woods-Saxon Potential for Shell-Model Calculations". In: (2007). arXiv: 0709.3525.

[16] K. Tsukada et al. "First Elastic Electron Scattering from Xe132 at the SCRIT Facility". In: *Physical Review Letters* 118.26 (June 2017). DOI: 10.1103/physrevlett.118.262501. URL: https://doi.org/10.1103/physrevlett.118.262501.

[17] Michelangelo Mangano et al. *Future Circular Collider*. Tech. rep. CERN-ACC-2018-0056. Submitted for publication to Eur. Phys. J. C. Geneva: CERN, Dec. 2018. URL: https://cds.cern.ch/record/2651294.

[18] Michael Benedikt et al. *Future Circular Collider*. Tech. rep. CERN-ACC-2018-0057. Submitted for publication to Eur. Phys. J. ST. Geneva: CERN, Dec. 2018. URL: https://cds.cern.ch/record/2651299.

[19] Michael Benedikt et al. *Future Circular Collider*. Tech. rep. CERN-ACC-2018-0058. Submitted for publication to Eur. Phys. J. ST. Geneva: CERN, Dec. 2018. URL: https://cds.cern.ch/record/2651300.

[20] CERN. *Cern-Accelerator-Complex*. http://te-epc-lpc.web.cern.ch/te-epc-lpc/machines/lhc/general.stm. Visited on 02.05.2019. 2016.

[21] G. Aad et al. "Observation of a new particle in the search for the Standard Model Higgs boson with the ATLAS detector at the LHC". In: *Physics Letters B* 716.1 (Sept. 2012), pp. 1–29. DOI: 10.1016/j.physletb.2012.08.020. URL: https://doi.org/10.1016/j.physletb.2012.08.020.

[22] S. Chatrchyan et al. "Combined results of searches for the standard model Higgs boson in pp collisions at sqrt(s) = 7 TeV". In: *Physics Letters B* 710.1 (Mar. 2012), pp. 26–48. DOI: 10.1016/j.physletb.2012.02.064. URL: https://doi.org/10.1016/j.physletb.2012.02.064.

[23] R. Aaij et al. "Observation of $J/\psi\ \rho$ resonances consistent with pentaquark states in $\Lambda_b^0 \to J/\psi K^- \rho$ decays". In: *Physical Review Letters* 115.7 (Aug. 2015). DOI: 10.1103/physrevlett.115.072001. URL: https://doi.org/10.1103/physrevlett.115.072001.

[24] R. Aaij et al. "Amplitude analysis of $B^+ \to J/\psi \phi K^+$ decays". In: *Physical Review D* 95.1 (Jan. 2017). DOI: 10.1103/physrevd.95.012002. URL: https://doi.org/10.1103/physrevd.95.012002.

[25] Wikipedia. *ALICE side view*. https://commons.wikimedia.org/wiki/File:2012-Aug-02-ALICE_3D_v0_with_Text_(1)_2.jpg. Visited on 02.05.2019. 2016.

[26] ALICE collaboration. *ALICE Inner Tracking System (ITS): Technical Design Report*. Technical Design Report ALICE. Geneva: CERN, 1999. URL: https://cds.cern.ch/record/391175.

[27] J. Alme et al. "The ALICE TPC, a large 3-dimensional tracking device with fast readout for ultra-high multiplicity events". In: *Nuclear Instruments and Methods in Physics Research Section A: Accelerators, Spectrometers, Detectors and Associated Equipment* 622.1 (Oct. 2010), pp. 316–367. DOI: 10.1016/j.nima.2010.04.042. URL: https://doi.org/10.1016/j.nima.2010.04.042.

[28] ALICE collaboration. *ALICE time projection chamber: Technical Design Report*. Technical Design Report ALICE. Geneva: CERN, 2000. URL: https://cds.cern.ch/record/451098.

[29] P Cortese. *ALICE transition-radiation detector: Technical Design Report*. Technical Design Report ALICE. Geneva: CERN, 2001. URL: https://cds.cern.ch/record/519145.

[30] ALICE collaboration. *ALICE Time-Of-Flight system (TOF): Technical Design Report*. Technical Design Report ALICE. Geneva: CERN, 2000. URL: https://cds.cern.ch/record/430132.

[31] ALICE collaboration. *ALICE Electromagnetic Calorimeter Technical Design Report*. Tech. rep. CERN-LHCC-2008-014. ALICE-TDR-14. Aug. 2008. URL: https://cds.cern.ch/record/1121574.

[32] V I Man'ko et al. *ALICE Photon Spectrometer (PHOS): Technical Design Report*. Technical Design Report ALICE. Geneva: CERN, 1999. URL: https://cds.cern.ch/record/381432.

[33] ALICE collaboration. *ALICE Photon Multiplicity Detector (PMD): Technical Design Report*. Technical Design Report ALICE. Geneva: CERN, 1999. URL: https://cds.cern.ch/record/451099.

[34] ALICE collaboration. *ALICE forward detectors: FMD, TO and VO: Technical Design Report*. Technical Design Report ALICE. Submitted on 10 Sep 2004. Geneva: CERN, 2004. URL: https://cds.cern.ch/record/781854.

[35] ALICE collaboration. *ALICE dimuon forward spectrometer: Technical Design Report*. Technical Design Report ALICE. Geneva: CERN, 1999. URL: https://cds.cern.ch/record/401974.

[36] ALICE collaboration. *Technical Design Report for the Muon Forward Tracker*. Tech. rep. CERN-LHCC-2015-001. ALICE-TDR-018. Jan. 2015. URL: https://cds.cern.ch/record/1981898.

[37] François Piuz et al. *ALICE high-momentum particle identification: Technical Design Report*. Technical Design Report ALICE. Geneva: CERN, 1998. URL: https://cds.cern.ch/record/381431.

[38] M Gallio et al. *ALICE Zero-Degree Calorimeter (ZDC): Technical Design Report*. Technical Design Report ALICE. Geneva: CERN, 1999. URL: https://cds.cern.ch/record/381433.

[39] B. Abelev et al. "Centrality determination of Pb-Pb collisions atsNN=2.76 TeV with ALICE". In: *Physical Review C* 88.4 (Oct. 2013). DOI: 10.1103/physrevc.88.044909. URL: https://doi.org/10.1103/physrevc.88.044909.

[40] ALICE collaboration. "Centrality determination using the Glauber model in Xe-Xe collisions at $\sqrt{s_{NN}} = 5.44$ TeV". In: (Apr. 2018). URL: http://cds.cern.ch/record/2315401.

[41] S. Acharya et al. "Transverse momentum spectra and nuclear modification factors of charged particles in pp, p-Pb and Pb-Pb collisions at the LHC". In: *Journal of High Energy Physics* 2018.11 (Nov. 2018). DOI: 10.1007/jhep11(2018)013. URL: https://doi.org/10.1007/jhep11(2018)013.

[42] S. Acharya et al. "Transverse momentum spectra and nuclear modification factors of charged particles in Xe–Xe collisions at $\sqrt{s_{\mathrm{NN}}}$=5.44 TeV". In: *Physics Letters B* 788 (Jan. 2019), pp. 166–179. DOI: 10.1016/j.physletb.2018.10.052. URL: https://doi.org/10.1016/j.physletb.2018.10.052.

[43] Xin-Nian Wang and Miklos Gyulassy. "HIJING: A Monte Carlo model for multiple jet production in pp, pA, and AA collisions". In: *Phys. Rev. D* 44 (11 Dec. 1991), pp. 3501–3516. DOI: 10.1103/PhysRevD.44.3501. URL: https://link.aps.org/doi/10.1103/PhysRevD.44.3501.

[44] S. Agostinelli et al. "Geant4—a simulation toolkit". In: *Nuclear Instruments and Methods in Physics Research Section A: Accelerators, Spectrometers, Detectors and Associated Equipment* 506.3 (July 2003), pp. 250–303. DOI: 10.1016/s0168-9002(03)01368-8. URL: https://doi.org/10.1016/s0168-9002(03)01368-8.

[45] Constantin Loizides, Jason Kamin, and David d'Enterria. "Improved Monte Carlo Glauber predictions at present and future nuclear colliders". In: *Physical Review C* 97.5 (May 2018). DOI: 10.1103/physrevc.97.054910. URL: https://doi.org/10.1103/physrevc.97.054910.

[46] B. Abelev et al. "Energy dependence of the transverse momentum distributions of charged particles in pp collisions measured by ALICE". In: *The European Physical Journal C* 73.12 (Dec. 2013). DOI: 10.1140/epjc/s10052-013-2662-9. URL: https://doi.org/10.1140/epjc/s10052-013-2662-9.

[47] "Performance of the ALICE experiment at the CERN LHC". In: *International Journal of Modern Physics A* 29.24 (Sept. 2014), p. 1430044. DOI: 10.1142/s0217751x14300440. URL: https://doi.org/10.1142/s0217751x14300440.

[48] Giuliano Giacalone et al. "Hydrodynamic predictions for 5.44 TeV Xe + Xe collisions". In: *Physical Review C* 97.3 (Mar. 2018). DOI: 10.1103/physrevc.97.034904. URL: https://doi.org/10.1103/physrevc.97.034904.

[49] A. M. Sirunyan et al. "Charged-particle nuclear modification factors in XeXe collisions at $\sqrt{s_{\mathrm{NN}}} = 5.44$ TeV". In: *Journal of High Energy Physics* 2018.10 (Oct. 2018). URL: https://doi.org/10.1007/jhep10(2018)138.

[50] Dusan Zigic et al. *Joint R_{AA} and v_2 predictions for $Pb + Pb$ collisions at the LHC within DREENA-C framework*. 2018. arXiv: 1805.03494.

[51] Magdalena Djordjevic et al. *How to test path-length dependence in energy loss mechanisms: analysis leading to a new observable*. 2018. arXiv: 1805.04030.

[52] Magdalena Djordjevic and Ulrich Heinz. "Radiative Energy Loss in a Finite Dynamical QCD Medium". In: *Physical Review Letters* 101.2 (July 2008). DOI: 10.1103/physrevlett.101.022302. URL: https://doi.org/10.1103/physrevlett.101.022302.

[53] Magdalena Djordjevic. "Theoretical formalism of radiative jet energy loss in a finite size dynamical QCD medium". In: *Physical Review C* 80.6 (Dec. 2009). DOI: 10.1103/physrevc.80.064909. URL: https://doi.org/10.1103/physrevc.80.064909.

[54] Jiechen Xu, Jinfeng Liao, and Miklos Gyulassy. "Bridging soft-hard transport properties of quark-gluon plasmas with CUJET3.0". In: *Journal of High Energy Physics* 2016.2 (Feb. 2016). DOI: 10.1007/jhep02(2016)169. URL: https://doi.org/10.1007/jhep02(2016)169.

[55] Shuzhe Shi, Jinfeng Liao, and Miklos Gyulassy. "Probing the color structure of the perfect QCD fluids via soft-hard-event-by-event azimuthal correlations". In: *Chinese Physics C* 42.10 (Sept. 2018), p. 104104. DOI: 10.1088/1674-1137/42/10/104104. URL: https://doi.org/10.1088/1674-1137/42/10/104104.

[56] Yayun He et al. "Linear Boltzmann transport for jet propagation in the quark-gluon plasma: Elastic processes and medium recoil". In: *Physical Review C* 91.5 (May 2015). DOI: 10.1103/physrevc.91.054908. URL: https://doi.org/10.1103/physrevc.91.054908.

[57] Shanshan Cao et al. "Heavy and light flavor jet quenching at RHIC and LHC energies". In: *Physics Letters B* 777 (Feb. 2018), pp. 255–259. DOI: 10.1016/j.physletb.2017.12.023. URL: https://doi.org/10.1016/j.physletb.2017.12.023.

[58] J. D. Bjorken. "Highly Relativistic Nucleus-Nucleus Collisions: The Central Rapidity Region". In: *Phys. Rev.* D27 (1983), pp. 140–151. DOI: 10.1103/PhysRevD.27.140.

[59] Michael Linus Knichel. "Transverse momentum distributions of primary charged particles in pp, p-Pb and Pb-Pb collisions measured with ALICE at the LHC". PhD thesis. Darmstadt: Technische Universität, 2015. URL: http://tuprints.ulb.tu-darmstadt.de/4930/.

[60] Julius Maximilian Gronefeld. "Transverse Momentum Distributions and Nuclear Modification Factors in Heavy-Ion Collisions with ALICE at the Large Hadron Collider". PhD thesis. Darmstadt: Technische Universität, 2018. URL: http://tuprints.ulb.tu-darmstadt.de/7653/.

Erklärung:

Ich versichere, dass ich diese Arbeit selbstständig verfasst habe und keine anderen als die angegebenen Quellen und Hilfsmittel benutzt habe.

Heidelberg, den (Datum) .....